Magnetic Field Dynamics and Shock Physics at the High Intensity Frontier of Laser Plasma Interactions

by

Brandon K. Russell

A dissertation submitted in partial fulfillment
of the requirements for the degree of
Doctor of Philosophy
(Electrical Engineering)
at the University of Michigan
2022

Doctoral Committee:

      Associate Professor Louise Willingale, Chair
      Professor Almantas Galvanauskas
      Professor Karl Krushelnick
      Dr. Anatoly Maksimchuk
      Professor Alexander G. R. Thomas

Brandon K. Russell

bkruss@umich.edu

ORCID iD: 0000-0003-0011-2419

Dedicated to my parents Robert and Joanne, my brother Cody,
my uncles Patrick and Gerald, and my dog Hunter.

ACKNOWLEDGMENTS

In any thesis I have read, it is not the science that I find the most interesting, but the acknowledgments. When one reads a paper or a thesis it is easy to simply look at the science without appreciating the human aspect of the science. By that, I mean the many hours of analysis, conversations with collaborators, the people who supported the person that wrote the paper, and the many years of experience that person accumulated to even work in a particular field of research. Among the many forms of scientific communication, the thesis acknowledgments are one of the rare places where these human aspects can be found.

This thesis discusses work I performed over the last 5 years, however it is also the accumulation of many more years of school where I was provided several opportunities to be able to work in this field. As a second year undergraduate student at the University of Alberta, Prof. Xihua Wang and Dr. Seyed Milad Mahpeykar allowed me to research with them and gain experience helping out with their projects studying quantum dot solar cells. Later, I approached Prof. Ying Tsui who gave me the opportunity to work at the Stanford Linear Accelerator National Laboratory (SLAC) during the summer before my final year as an undergraduate. At SLAC, I was advised by Prof. Siegfried Glenzer and worked with a group of exceptional scientists including Dr. Zhijiang Chen, Dr. Mianzhen Mo, and Dr. Benjamin Ofori-Okai who gave me my first introduction to High Energy Density Physics (HEDP) research. I am truly grateful to all of these people who provided me the opportunities and support as an undergraduate that allowed me to purse graduate school and to research in the field of HEDP.

Following my undergraduate degree I was lucky enough to be accepted to the University of Michigan into a research group full of supportive and kind people. My PhD work would

not be possible without the support of my advisor, Prof. Louise Willingale. She has given me countless opportunities throughout my degree, including allowing me to lead research on the T-cubed laser, lead experiments on the OMEGA EP laser facility, attend conferences, and run large simulations on super computers. Additionally, she has tried to set me up to succeed in the future by connecting me with other scientists, giving me career/life advice, and the opportunity to pursue my own research topics. After working with Prof. Willingale for 5 years, I can confidently say she is a truly great advisor who cares about her students.

I would also like to acknowledge Dr. Anatoly Maksimchuk who had a significant impact on the first few years of my time at Michigan. Although I have not presented work in this thesis that we worked on together, he and I spent years working together on the T-cubed laser. From that time I learned a huge amount, from how to run and setup experiments to being confident in my ideas. I appreciate all the advice he has given me, the stories about other students breaking things to make me feel better after accidentally blowing things up, and the excitement after successfully setting up a diagnostic or obtaining some nice data. I am lucky to have had such a good mentor.

I would like to recognize the support of Prof. Alec Thomas, Prof. Karl Krushelnick and Dr. Paul T. Campbell who have all contributed significantly to the work in this thesis and my experience at Michigan. Prof. Thomas has greatly motivated me to pursue the theoretical side of plasma physics in addition to experiments, and our discussions have led to the derivation of most equations presented in this thesis. Prof. Krushelnick has been integral to my experience at Michigan, providing me the opportunity to run experiments at the OMEGA EP laser facility and many ideas for these experiments. Paul has been my go-to person for discussing ideas and has had influence on or directly contributed to all the work presented in this thesis. I would like to thank Paul for all his help and for being a great friend during my time at Michigan.

I am also thankful for the many students in the High Field Science group who I have worked with over the years. I am particularly grateful to Hongmei Tang for helping out

PREFACE

This thesis covers novel work from four papers that have either been published, submitted or are in preparation. Specifically:

Chapter 4 summarizes the following publication:

B. K. Russell, P. T. Campbell, A. G. R. Thomas, and L. Willingale, Multiple species laser-driven ion-shock acceleration, Plasma Phys. Control. Fusion 63, 095012 (2021)

I performed all the simulations and analysis reported in this publication. The theory was derived with help from A. G. R. Thomas.

Chapter 5 summarizes the following publication:

P. T. Campbell, B. K. Russell, C. Dong, G. Fiksel, P. M. Nilson, A. G. R. Thomas, C. A. Walsh, K. M. Krushelnick, and L. Willingale, Observation of semi-relativistic quasi-perpendicular shocks, 2022 (submitted)

The experiment and analysis of experimental data was led by P. T. Campbell. I helped with experimental analysis and ran the 3D simulation with help from C. Dong and P. T. Campbell. I performed all analysis on the 3D simulation and co-wrote the paper with P. T. Campbell.

Chapter 6 summarizes the following publications:

B. K. Russell, M. Vranic, P. T. Campbell, A. G. R. Thomas, K. M. Schoeffler, D. A. Uzdensky, and L. Willingale, Magnetic field generation in laser-solid interactions at strong-field QED relevant intensities, 2022 (in preparation)

I performed all the simulations and analysis reported in this publication and derived the theory with help from A. G. R. Thomas. The simulations were advised by M. Vranic and K. M. Schoeffler. I wrote the paper with input from all co-authors.

B. K. Russell, P. T. Campbell, Q. Qian, J. Cardarelli, L. Willingale, and A. G. R. Thomas, Ultrafast relativistic electron probing of extreme fields, 2022 (in preparation)

This paper is being co-written by myself and P. T. Campbell. Theory was derived by myself with help from Q. Qian.

TABLE OF CONTENTS

LIST OF FIGURES

ABSTRACT

This thesis presents experimental, computational, and theoretical work studying shock formation and magnetic field generation. The work was performed primarily in the highly energetic relativistic regime of laser plasma physics and uses simulations to obtain insight into an even higher energy regime where quantum electrodynamic effects become important.

Two forms of collisionless shocks are studied: electrostatic shocks, and magnetized shocks. Electrostatic shocks are explored through a set of particle-in-cell simulations using a simplified two-dimensional slab model and simulations including a relativistic intensity laser pulse. These simulations were performed to understand the effects of multiple ion species on laser-driven shock formation and proton acceleration. It is found that with the inclusion of a second ion species multiple shocks can form and ions can experience more than one stage of acceleration. We attempted to modify standard shock theory, which treats ions as a fluid, to include a second ion species. However, it is shown that this fluid theory breaks down due to reflections which require a kinetic model. Laser driven simulations showed that the inclusion of a second ion species reduced proton acceleration. Double shocks are not always formed and require sufficient density steepening to form.

Magnetized shocks are studied through experiments and simulations. Using the OMEGA EP laser system, a plasma plume was generated on a thin plastic foil using a moderate intensity long pulse laser and strongly magnetized relativistic electrons accelerated from the focal spot of a relativistic short pulse laser were interacted with this plume. The interacting fields were measured using proton deflectometry. Forward scattering was used to model the

observed features. The features could be formed due to a build up of short pulse generated fields, or annihilation of magnetic fields at the interface where the plasmas interact. A massive three-dimensional particle-in-cell simulation showed that a discontinuity was generated from which a shock is driven into the long pulse generated plasma plume. This discontinuity became unstable and two-dimensional simulations are used to understand the instability formation. Electron particle tracking shows trajectories consistent with shock drift acceleration. This is the first experimental evidence of semi-relativistic magnetized shock formation and may be the basis for many energetic experiments studying the microphysics of extreme astrophysical environments.

The final part of this thesis explores the generation of magnetic fields on the next generation laser facilities where expected intensities exceed 10^{23} W/cm^2. At these intensities it has been shown that quantum electrodynamic effects appear, however it is unclear how these processes affect magnetic field generation in laser-solid interactions. By performing several two-dimensional particle-in-cell simulations at various laser intensities including QED effects, magnetic field generation was studied. It was found that the laser pulse channels and hole bores into the target, driving relativistic electrons along the surface of the target with an associated return current. The target electron density depletes due to this return current setting up fields that pull the radially expanding electrons towards the target, generating a thin layer of strong > 0.1 MT magnetic fields. The scaling of these fields with intensity is found and is seen to be limited by radiation reaction as a significant fraction of energy is converted to photons. This field generation mechanism is modeled using a set of simple equations that allow for the estimation of maximum field strength using laser parameters.

CHAPTER 1

Introduction

There are few processes more ubiquitous in our universe than shock formation. Shock waves appear as an abrupt change in the pressure, density and temperature of a medium. A common example of a shock on Earth is that formed by an airplane moving faster than the local speed of sound in the air. In astrophysical systems shocks commonly form where there is an energetic flow of particles. For example, a shock forms far from the surface of the Earth between the solar wind and the dipolar magnetic fields (magnetosphere) of the Earth [3]. They are also seen in far more energetic systems including the interface between a supernova and the interstellar medium [4, 5] or between the winds of the pulsar and the supernova remnant that it is nested in [6]. The Earth's bow shock has been directly probed by spacecraft [7], however most other astrophysical shocks can only be observed through the measurement of particles accelerated by the shocks as they arrive at Earth or images at specific wavelengths where the plasma around the shock emits light. This is especially true for the extremely energetic shocks of pulsar wind nebulae that exist several light-years away [8]. Understanding these systems is currently a topic of significant interest and a growing body of theoretical work is being generated on this topic [9].

Magnetic field generation is perhaps an even more fundamental process in our universe and can even be the precursor to shock formation [10]. Magnetic fields are observed everywhere from planetary magnetospheres to active galactic nuclei jets. The magnetic fields of Earth's magnetosphere act to shield us from incoming plasma. However, magnetic fields are

also a large source of energy in the universe that can be rapidly converted to particle kinetic energy through magnetic reconnection to generate the plasma that bombards the Earth's magnetosphere, e.g. flares and coronal mass ejections. The way these fields are generated and how they are amplified to observed strengths is still an open question [11]. Many theories exist including dynamo amplification [12], instabilities [13], and the Biermann battery mechanism [14].

The advent of high energy density physics (HEDP) has allowed for the exploration of both shocks and magnetic field generation in the laboratory [15]. Plasmas formed in the high energy density regime have pressures exceeding 0.1 Mbar or 10^{10} J/m^3. High-power laser pulses with powers of several TW to PW can create the conditions necessary to drive shocks in plasmas or to generate magnetic fields. These experiments have covered a large parameter space, with collisionless [16] and collisional [17] shocks being generated, and large magnetic fields from 1-100 MG being produced [18–20]. Some of the most energetic shocks have been generated for inertial confinement fusion (ICF) using the extremely powerful National Ignition Facility (NIF) [21].

Currently there is significant excitement in the field of HEDP as new laser facilities are being commissioned. These laser facilities aim to explore an extremely energetic regime of plasma physics where strong field quantum electrodynamic (SFQED) effects become important to the dynamics of the system [2]. With the extreme laser intensities promised from these facilities, a completely new field of plasma physics, "extreme laboratory astrophysics" may emerge. This new field may study the microphysics of extreme astrophysical environments e.g. pulsar magnetospheres, blackhole accretion disks, supernova remnants [22].

This first part of thesis presents theory, simulations, and experimental data of shock formation and magnetic field dynamics at the current energetic limit of laser facilities known as the relativistic regime. The second part of this thesis will show simulations and theory that will lay the ground work for magnetized experiments on next-generation laser facilities to potentially access the extreme plasma regime.

2

1.1 Laser-Plasma Interaction History

The work presented in this thesis covers laser-plasma interactions over a wide range of laser intensities from the moderate intensity conditions generated by $\sim 10^{14}$ W/cm^2 long pulse lasers to those generated by $> 10^{23}$ W/cm^2 ultra-intense pulses. Prior to the Nobel Prize winning idea of chirped pulse amplification (CPA) in the mid-1980's [23], laser intensities had reached values $\sim 10^{15}$ W/cm^2. In the interaction with a solid target this moderate intensity can generate plasma plumes with keV temperatures and magnetic fields $\mathcal{O}(\text{MG})$. This is the intensity range that is commonly accessed by relatively long-pulse lasers with durations of 100's of ps to ns. Interactions in this intensity range still make up a large fraction of plasma physics research because they can deliver a lot of energy to a system. Many large laser facilities including the National Ignition Facility (NIF) at Lawrence Livermore National Laboratory (LLNL) and OMEGA at the University of Rochester Laboratory for Laser Energetics (LLE), use long-pulse lasers to study inertial confinement nuclear fusion, or highly collisional plasmas where the plasma can be modeled as a fluid.

Much of the work in this thesis is centered in the relativistic regime where fields are so strong in the focus of a laser pulse that they can accelerate electrons to a large fraction of the speed of light within a laser cycle. This regime can be accessed by CPA lasers with intensities $> 10^{18}$ W/cm^2. Over the past couple of decades, several interesting phenomena have been discovered, including laser wakefield acceleration of electrons [24, 25] and relativistically induced transparency [26, 27]. There is a significant amount of work being performed to understand the unique physics that appear in the relativistic regime.

Recently there has been a push to access an even higher energy regime where quantum electrodynamic (QED) effects, e.g. radiation generation and pair creation, become important. This regime is so energetic that the photons radiated from electrons accelerated by the laser fields have enough energy to create electron positron pairs within the strong laser fields. These pairs can then be accelerated in the fields and generate more photons, creating a runaway process known as a pair cascade [28]. Reaching this regime with just the fields of

a laser pulse is well outside of what can be achieved using current laser technology. Instead, special relativity can be leveraged to lower the threshold to access this regime. By colliding a high-energy electron beam head-on with a laser pulse, the pulse appears to be significantly more intense from the perspective of the electrons in the beam [29]. There is a significant amount of excitement around this concept and many simulations have been performed to understand how it may work in experiment. Several laser facilities around the world are being built that may be able to achieve this experimental configuration. In particular, the ZEUS facility at the University of Michigan is being commissioned with the purpose of running this as its flagship experiment [30].

1.2   Laboratory Astrophysics

Laboratory astrophysics is an application of plasma physics that attempts to study astrophysical systems in the laboratory. Generally, these experiments do not try to recreate the complete global picture of a system e.g., a star, but instead they study the microphysics, e.g. magnetic reconnection that drives solar flares. One may be skeptical of how such systems can compared when experiments occur on micron or mm scales while astrophysical features can occur on the scale of 1000's of km. However, experiments are commonly performed in the hydrodynamic regime that allows for the Ryutov scalings to be invoked [31]. This hydrodynamic scaling uses a set of dimensionless parameters to define the properties of the astrophysical and laboratory systems. Given that the dimensionless parameters are similar then the systems will evolve in similar ways even though their spatial scales, velocities, and field strengths may be different by many orders of magnitude.

Scientists working in this area have attempted to study many topics using large plasma devices, pulsed powered systems, and lasers. Plasma devices such as MRX and LAPD have been used to study magnetic reconnection [32, 33]. Several reconnection experiments have also been performed using laser pulses although these experiments generally struggle to scale
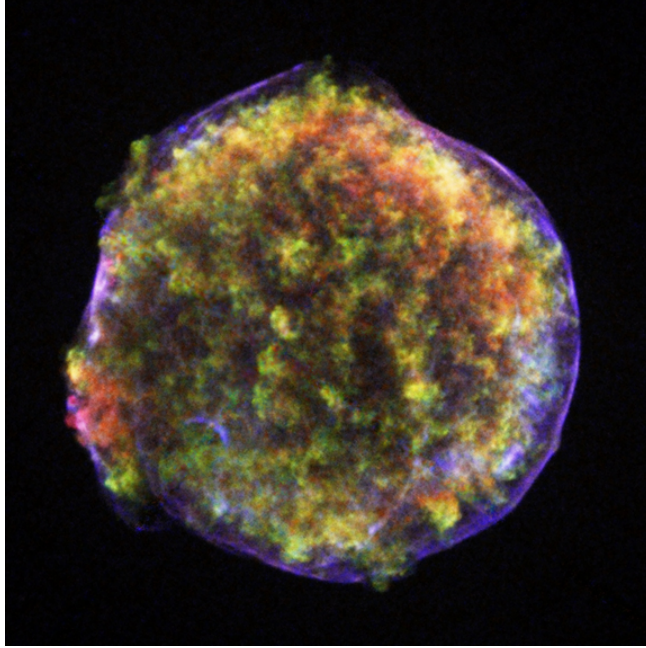
Figure 1.1: Tycho supernova SN1572 with shocks seen around the perimeter of the rapidly expanding plasma. Credit:NASA/CXC/Rutgers/J.Warren and J.Hughes *et al.* [1]

to the expected parameters of commonly studied astrophysical systems [34]. Shocks have been rigorously studied in the collisional regime using long-pulse lasers, and recently Weibel mediated shocks have been studied [35]. Lasers have also been used to compress materials such that materials can be studied at the expected pressures of planetary interiors [36]. Pulsed power systems have been used to study bow-shocks [37] and famously the Z-machine at Sandia National Laboratory found discrepancies in models for the solar opacity of iron [38].

Recently some experiments have been performed in the much higher energy semi-relativistic regime [39, 40]. In Chapter 5 we demonstrate for the first time, semi-relativistic magnetized shock formation in the laboratory. As laser intensities increase we may be able to reach a much more energetic regime relevant to extreme astrophysical environments. Chapter 6 lays the groundwork for the study of magnetized astrophysics experiments in this regime.

1.3 Shocks

Shocks form on many scales throughout our universe and are routinely produced in the lab under various conditions. Just as lasers have a range of energies or intensities to characterize their regime, shocks can also be characterized by their properties including the energy of inflowing particles, the importance of magnetic fields to the shock physics, and the collisionality. If we consider, for example, the shock formed between the magnetic fields of the Earth and the solar wind, i.e. the plasma emitted from the Sun, this shock is quite low energy with inflow velocities $\sim$100 km/s [41]. These inflow velocities may seem fast relative to what we see in our daily lives, however this is quite slow compared to the extreme speeds of the relativistic shocks observed around pulsar wind nebulae (PWN) or supernova remnants (SNR) like that shown in Fig. 1.1. Unlike Earth's bow shock, which has been directly probed by sending spacecraft through the plasma that forms the shock, the shocks outside our solar system can only be studied through the light that they emit and the extremely energetic particles that they accelerate toward us. The Tycho supernova remnant image shown in Fig. 1.1 is constructed by superimposing a set of images taken at different wavelengths of light. By measuring the spectra emitted from different regions of the SNR the properties of the plasma can be extracted [42, 43]. Spectroscopic techniques are also commonly used to measure the properties of the Sun. While the Sun is relatively close to us, it is however much too energetic to be probed directly [44, 45].

To understand how these astrophysical shocks form, theoretical models have been created and many simulations have been performed with parameters relevant to those measured in astrophysical systems [46, 47]. The theory of these shocks will be reviewed in Chapter 2. Laboratory shock experiments have also been performed, to provide insight into shock formation and particle acceleration [35, 48, 49]. These experiments are generally performed using lasers due to the high energies and pressures they can achieve. The most common shocks generated in the laboratory are collisional shocks, where the plasma can be modeled as a fluid and standard hydrodynamic shock theory can be used. A more recent experimental

development has been the generation of collisionless shocks [50]. The shocks discussed in this thesis are collisionless, meaning that particle collisions are not important to the interaction and the shock is instead mediated by electric and in some cases magnetic fields [51]. The study of these shocks is important as many shocks in space occur in the collisionless regime. For example the shock that forms ahead of coronal mass ejections from the Sun [52], and shocks that form in PWN [53]. These shocks are particularly interesting because of the extremely energetic particles or cosmic rays that been measured from systems where shocks have been observed. Understanding the processes that accelerate these cosmic rays is a large area of research in both heliophysics and astrophysics. One prominent theory is that particles can be accelerated multiple times by shocks through a process known as diffusive shock acceleration (DSA) [54]. A threshold energy is necessary for this mechanism, therefore particles must be pre-accelerated, potentially through another mechanism such as shock drift acceleration (SDA) [55]. SDA is shown through simulations in Chapter 5 as a potential acceleration process occurring in an experiment that we performed.

1.4   Ion Acceleration

Ion acceleration in the laboratory has many other applications beyond understanding the processes that occur in astrophysical shocks. One of the potential applications of high-energy ion beams is for cancer therapy [56]. Unlike other forms of radiation, like high energy photons and electrons which give up energy to a material throughout their whole path of propagation, ions give up the majority of their remaining energy in a very small volume once they have almost stopped in the material. Therefore treatment schemes using protons to damage specific cancer cells while minimizing damage to the rest of the cells along the particle's trajectory are appealing. To do this, a high energy (10's to 100's MeV) beam with a small energy spread is required. Finding an acceleration mechanism to produce this type of beam has been an important area of laser-driven ion acceleration research as a way to potentially

reduce the scale of an accelerator required for hadron therapy. Shocks have been proposed as a mechanism for producing these beams and simulations have shown that beams with energies > 100 MeV may be produced at currently available laser intensities [57]. Experimentally, collisionless shock acceleration (CSA) has produced $\sim$ 18 MeV/amu beams with 10-20% energy spread from pre-ablated multi-species targets [58] and $\sim$ 20 MeV beams with 1% energy spread from H_2 gas jets [16]. An alternative acceleration mechanism, where the whole target is simultaneously driven by a laser pulse, called radiation pressure acceleration (RPA) has been proposed as a method for producing narrow energy-spread beams [59]. RPA requires extremely thin (few nanometer) targets and specific laser properties. Although simulation and theory show that high energy ion beams could be driven, in experiment instabilities appear that reduce the performance of the mechanism [60].

The simplest mechanism for accelerating ions is target normal sheath acceleration (TNSA) [61]. This mechanism occurs in the interaction of a laser with a thin (few μm) solid density target. Both shock acceleration and RPA require specific and difficult to practically achieve target density profiles to accelerate quasi-monoenergetic ion beams. TNSA does not have such stringent target or laser requirements to accelerate ions, however the beams produced are very different from those of CSA. The beams can have quite large energies up to 100 MeV and large beam charge [62], however the continuous, Maxwellian-like energy spread makes them an unsuitable source for proton therapy. TNSA beams are suitable for imaging applications due to their small transverse emittance. In this thesis TNSA proton beams are used to image and quantify the fields occurring in laser-solid interactions. This method, known as proton deflectometry, allows for the quantitative measurement of electric and magnetic fields by comparing the deflection of protons through the fields to the path of protons without deflection [63]. It has shown great utility in measuring the fields of many laser-plasma interactions including laser-driven magnetic reconnection [34].

1.5 Magnetic Field Generation

Magnetic fields form on many scales throughout the universe with a huge range of magnitudes. We live inside the large-scale magnetic field of the Earth which protects us from coronal mass ejections, solar flares, and the solar wind [64, 65]. These three phenomena are also magnetized, meaning that particles orbit around magnetic field lines more frequently than they experience collisions, therefore particle trajectories are strongly coupled with magnetic field lines. The magnetic fields originate from the Sun. The Sun's field extends to even larger distances forming the heliosphere between its fields and the background interstellar medium that our solar system travels through [66]. Outside the heliophere exist many astrophysical bodies and environments that have their own magnetic fields e.g., the many stars we observe, supernova remnants, pulsars, and even the plasma surrounding black holes [22]. In terms of magnitude the fields of the solar wind are on the order of nT [41] while the most energetic environments of magnetars are theorized to have $> 10^{11}$ T fields [67], a difference of 20 orders of magnitude.

One might expect that based on the relatively small spatial scales of laboratory experiments that the fields generated must have magnitudes much smaller than the large-scale fields observed elsewhere in the universe, however this is not true. Coils are commonly used in magnetized experiments with large capacitor banks to drive pulsed externally applied fields > 10 T [68, 69]. Capacitor coil targets can be driven by high-power lasers to drive $\sim$kT fields external to a plasma experiment [70]. In the interaction of lasers with solid targets the resulting plasma plumes will self generate magnetic fields that have strengths > 100 T for long-pulse lasers [19], ~ 10 kT for relativistic intensity lasers [20, 71], and a mechanisms for even stronger field generation through the ponderomotive force has been theorized [72].

From these many magnetized systems it is clear that magnetic field generation is fundamental component of plasma physics and is important to understanding our universe. This is certainly true if we also consider not just the existence of magnetic fields in systems but also their effects. Magnetic fields have been shown through theory and simulation to be a major

source of particle acceleration in astrophysics either by the direct conversion of magnetic potential energy or indirectly by driving particles through accelerating electric fields. The turbulent magnetic background formed near magnetized shocks is able to reflect particles back through shocks through the process of diffusive shock acceleration (DSA) [54]. Anti-parallel magnetic fields driven together can annihilate and accelerate particles, converting magnetic potential energy to particle kinetic energy [73]. This process known as magnetic reconnection is theorized to be the driver of solar flares and has been measured in Earth's magnetosphere [74]. Magnetic reconnection and DSA have both been proposed as processes that may accelerate the highly energetic cosmic rays that we observe at Earth coming from distant astrophysical environments [75, 76].

The way astrophysical fields form is known in the literature as "magnetogenesis" and is still an open question [11], although there have been many mechanisms suggested. For the formation of planetary and stellar magnetic fields, the magnetic dynamo has been suggested whereby loops of magnetic fields in plasmas become twisted by the flowing plasma and are amplified [12]. This process requires a seed magnetic field. Another mechanism is the Weibel instability whereby a positive feedback loop forms between wave-like magnetic field perturbations and currents [13]. The Biermann battery effect can generate magnetic fields from non-equilibrium conditions in plasmas [14]. Some of these field generation mechanisms also appear in laboratory experiments either in configurations purposely designed to study a mechanism e.g. Weibel instability [77], turbulent dynamo [78], or from mechanisms that are inherent to certain interactions e.g. Biermann battery in long-pulse laser-solid interactions [19].

If we look ahead to the next generation of laser facilities where laser intensities may reach the QED regime, the field generation mechanism is currently not well understood. In Chapter 6 the field generation mechanism in this regime is studied using simulations and theory. This is important because field generation may be very different with QED effects and knowing the topology and magnitude of these fields and how the fields co-exist with

energetic electrons and potentially positrons will be important to any future magnetized experiment.

1.6   Thesis Outline

The thesis is structured as follows:

Chapter 2:   The relevant theory to understand the work outlined in this thesis is introduced. This includes discussion of laser pulse characteristics, laser-plasma interaction physics, shocks, ion acceleration, and magnetic field generation.

Chapter 3: The primary methods used to perform the work in this thesis are summarized. This includes a discussion of the OMEGA EP laser system, experimental diagnostics, and particle-in-cell simulations.

Chapter 4: Novel simulation and theoretical work studying ion acceleration in plamsas with multiple ion species is summarized. Several parameter scans are performed using simplified models in 2D particle-in-cell simulation and are used to inform theoretical models for high Mach-number shocks. These models are relevant to multi-species laser driven shocks which are explored using 2D simulations.

Chapter 5:   An experiment performed on OMEGA EP and the subsequent analysis including 2D and 3D simulations is presented. This experiment showed evidence for semi-relativistic magnetized shock formation. The simulations elucidated the dynamics of the shock, demonstrating that it is unstable to shear and streaming instabilities and shows evidence of shock drift acceleration.

Chapter 6: Theoretical and simulation work relevant to next-generation laser facilities is discussed. The interaction of short ultra-intense laser pulses with solid targets is investigated using particle-in-cell simulations including QED processes. These simulations provide a scaling of target-surface magnetic field strength with laser intensity and demonstrates

how these fields are generated. The results are used to derive a set of equations that can accurately estimate field strengths outside the laser focal volume starting from laser parameters. Additionally, high energy laser wakefield accelerated electrons are considered as a potential probe for strong fields generated in laser interactions. With GeV electron beams QED effects become important to the probe. Several probing considerations are discussed and the equations demonstrating the potential for QED effects to be leveraged as a diagnostic are derived.

CHAPTER 2

Theoretical Background

In this chapter, the physics necessary to understand the content of this thesis will be reviewed. Although this thesis only covers two fundamental topics: shocks and magnetic fields, these topics are studied over a large range of energetic regimes. Additionally, the physics is studied in the context of laser-driven experiments, giving added complexity, therefore many topics will be covered in this chapter.

This thesis only considers near critical and over-dense laser-plasma interactions where the plasma is too dense to allow for laser propagation. The physics that define this interaction will be outlined in the following sections. Although there are several similarities between overdense plasma experiments and underdense interactions, there are additional considerations that must be made in the choice of laser pulse properties. These considerations will also be outlined. A summary of the processes that occur in intense laser-solid interactions is shown in Fig. 2.1.

The primary sources for several of the following sections is the textbook by Gibbon [79]. Other references have been specified in their respective chapters.

2.1   Laser Properties

For the purpose of experiments and simulations we care about a few main properties of a laser pulse: pulse duration, energy, central wavelength, contrast, and spatial profile. These properties can be fundamental to the chosen laser gain medium and cavity or defined by the
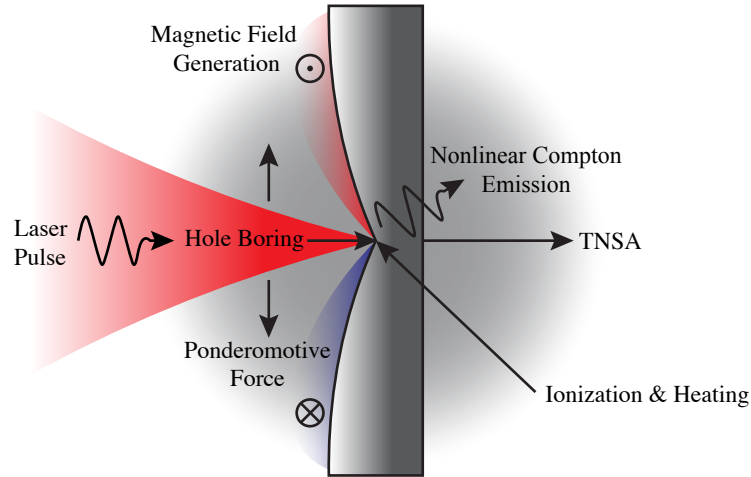
Figure 2.1: A summary of some of the processes that occur in high-intensity ($> 10^{18}$ W/cm^2) laser-solid interactions.

set of optics that exist between the laser cavity and the final target where the plasma experiment takes place. Here we will cover basic laser concepts, for a more detailed explanation see the textbook by Anthony Siegman [80].

The simplest picture of a laser consists of a laser gain medium, a pumping source and a cavity. In high-power laser systems the gain medium is generally a type of glass or crystal doped with some concentration of ion, e.g. Nd:YAG or Ti:Sapphire. In the case of titanium sapphire (Ti:Sapphire), the sapphire crystal is doped with titanium ions. The electrons of the dopant ion have several discrete energy levels that they can be excited to. Electrons can be excited from a lower energy state to an upper state by pumping the gain medium. This is generally done optically using flash lamps or pump lasers. Excited atoms will later decay and produce a photon with a frequency ν and corresponding energy $E_\gamma = h\nu$ which is equal to the difference in the energy of the upper and lower energy state. This process of spontaneous emission will not produce a coherent pulse of light, it will instead produce a background

of photons that propagate in all directions with various frequencies. To produce a laser pulse one must leverage the process of stimulated emission. Additionally, a cavity must be used to restrict the possible laser wavelengths that are allowed to propagate. Photons with wavelengths allowed by the cavity will propagate through the laser gain medium repeatedly. As these photons propagate through the excited medium, each photon will interact with an excited atom, causing it to rapidly decay and produce a photon with identical momentum to the seed photon. If this process occurs several times then the number of photons will grow exponentially. In high-power laser systems, the pulse that exits the cavity will act as a seed pulse that will be sent into additional gain media to be amplified.

The resultant amplified pulse consists of the short pulse generated by stimulated emission superimposed on a background pedestal of spontaneously emitted photons. The ratio of the laser intensity at the peak of the pulse to the peak of the pedestal is the laser intensity contrast. Most laser systems will use a complex laser cavity that includes mirrors to send the pulse through the gain medium multiple times combined with passive or active switching, causing the laser cavity to only accept specific laser wavelengths and to produce high-contrast pulses. Laser contrast is very important for solid-target laser interactions because the spontaneous emission can create a pre-plasma on the target, or perhaps completely destroy the target before the main part of the laser arrives in the case of ultra-thin nm targets. In some laser systems plasma mirrors will be used to increase the laser contrast [81].

A laser pulse is constructed by the temporal and spatial superposition of several wavelengths of light. If we consider a pulse with a Gaussian temporal profile it will be defined by the equation:

$$E_L(t) = E_0 e^{-t^2/\tau^2} e^{i\omega_L t}, \tag{2.1}$$

where τ defines the envelope or temporal shape of the pulse and ω_L defines the central frequency or carrier frequency of the pulse. If the Fourier transform of this pulse is taken, one finds that the minimum pulse duration and frequency bandwidth are fundamentally related by $\tau \Delta \nu = const$. Therefore, in order to produce very short pulses large bandwidths

are needed.

The spatial profile is an important property for focusing the pulse to the smallest spot possible and therefore for reaching the highest intensity. The spatial profile is highly dependent on the laser system and can become non-uniform due to transverse spatial non-uniformities in the laser gain medium. In high power laser systems this is commonly corrected using spatial filters and more recently using deformable mirrors [82].

The property of the laser pulse that best defines how strong the interaction will be is the laser intensity. In standard optics the intensity I is simply defined in units of $\mathrm{W/cm^2}$, however at very high intensities a more relevant parameter is the peak normalized vector potential given by:

$$a_0 = \frac{eE_0}{m_e c \omega_L} \propto \sqrt{I\lambda_L^2}, \tag{2.2}$$

where e is the electron charge, λ_L is the laser wavelength, and m_e is the electron mass. This equation comes from the ratio of the electron quiver velocity to the speed of light. It can also be interpreted as the amount of work done by the peak laser electric field over a distance of $\lambda_L/2\pi$ normalized to the electron rest mass energy $m_e c^2$. Therefore, if $a_0 > 1$, electrons accelerated by the peak laser field will gain kinetic energy in excess of their rest mass energy. This is the threshold for what is defined as relativistic.

To relate a_0 to laser intensity we first note that the vector potential of a plane wave is given by:

$$\mathbf{A}(z, t) = A_0 \sin(k_L z - \omega_L t)\hat{x}, \tag{2.3}$$

where $k_L = 2\pi/\lambda_L$ is the wavenumber and $\omega_L = 2\pi c/\lambda_L$ is the laser frequency. Specifically, this is for a plane wave propagating along the z-direction and polarized in the x-direction. The vector potential can be converted to the electric and magnetic fields through the following relations:

$$\mathbf{E}(z, t) = -\frac{\partial \mathbf{A}}{\partial t} - \nabla\phi = \omega_L A_0 \cos(k_L z - \omega_L t)\hat{x}, \tag{2.4}$$

$$\mathbf{B}(z, t) = \nabla \times \mathbf{A} = k_L A_0 \cos(k_L z - \omega_L t)\hat{y}, \tag{2.5}$$

16

where the gradient of the electric potential $\nabla\phi = 0$ for a plane wave propagating in a vacuum. The Poynting vector of the laser averaged over a laser period is then given by:

$$I = \langle |S| \rangle = \frac{1}{\mu_0} \langle |\mathbf{E} \times \mathbf{B}| \rangle = \frac{\epsilon_0 c}{2} E_0^2, \qquad (2.6)$$

where $E_0 = \omega_L A_0$. This can then be substituted into Eqn. 2.2 for E_0 to give:

$$a_0 \approx \sqrt{\frac{I\lambda_\mu^2}{1.37 \times 10^{18}\ \mathrm{Wcm}^{-2}\mu\mathrm{m}^2}}, \qquad (2.7)$$

where $I\lambda_\mu^2$ is in units of $\mathrm{Wcm}^{-2}\mu\mathrm{m}^2$. From this equation we can see that for a laser pulse with a 1 μm central wavelength, the onset for relativistic plasma interactions is $\sim 10^{18}$ W/cm^2.

The record for highest laser intensity was held for many years by the HERCULES laser at $> 10^{22}$ W/cm^2 [83], however other lasers throughout the world have since reported slightly higher intensities [84]. Currently multi-petawatt lasers are being built that are expected to exceed 10^{23} W/cm^2 [30,85]. The scale of these lasers is much larger than previous relativistic intensity lasers in both size of laser components and the number of technical staff required to build and maintain these lasers. If we consider the properties that allow for high intensities they are pulse duration, pulse energy, and ability to focus the pulse. Pulse duration is inherent to the gain medium used and typically becomes larger after amplification, however there are some optical systems that use complex components to alter the pulse spectra and therefore pulse duration. Minimum pulse durations are $\sim$ 5 fs. With the ideal spatial profile and phase front quality there is a minimum spot size that can be achieved by a focusing optic defined by the diffraction limit. Therefore, the main property that can be used to increase laser intensity is the laser energy. Any optical component in a laser system has an inherent damage threshold that defines how much energy can be incident on a unit area of material without irreversible changes occurring in the material. For a specific laser energy this then defines the minimum beam size. In petawatt class systems beam energies have become so large that optics must have diameters of almost a foot. This means that

optics are extremely expensive and facilities and their vacuum systems must be very large to contain all the optics. If we look at the future of laser intensity this means that significant technological improvements must occur before laser intensities can become much larger.

2.2 Laser Ionization

Ionization is the process by which electrons bound to an atom are freed. When done with a large number of atoms the multiple ionizations form a plasma. There are several types of ionization that can occur depending on photon energy and material/atom, however they all must work in one of two ways. An electron must gain enough energy to escape the atomic potential energy that bounds it to the atom, or the Coulomb barrier of the atom/molecule must be suppressed such that an electron can escape. For the former there are two possibilities, the electron gains enough energy from absorbing a single photon or scattering from another particle to exceed the ionization potential, or it rapidly obtains energy from the absorption of several photons. For most atoms, the ionization potential greatly exceeds the energy of a single optical photon. Even for high Z metals, the outer shell electrons have ionization potentials of a few eV and UV lasers would be required. The process of multiphoton ionization is typically slow, however it is the dominant mechanism for ionization when the Keldysh parameter given by [86]

$$\gamma_k = \frac{\text{tunneling time}}{\text{laser period}} = \sqrt{\frac{I_p}{2U_p}}, \tag{2.8}$$

is > 1, where $U_p = e^2 E_L^2 / 4 m_e \omega_L^2$ is the non-relativistic ponderomotive potential.

As γ_k decreases the dominant ionization mechanism transitions from multiphoton ionization to ionization based on the suppression of the Coulomb barrier. When the ponderomotive potential U_p exceeds the ionization potential I_p then the Coulomb barrier will be suppressed

enough that electrons can tunnel through the remaining barrier. This threshold is

$$I(\text{W/cm}^2) > 5.4 \times 10^{12} \frac{\text{I}_\text{p}(\text{eV})}{\lambda_\mu^2}. \tag{2.9}$$

If the laser intensity is further increased the Coulomb potential can be completely suppressed, allowing for barrier suppression ionization. The threshold for this type of ionization is given by

$$I(\text{W/cm}^2) \approx 4 \times 10^9 \left(\frac{\text{I}_\text{p}}{\text{eV}} \right)^4 \text{Z}^{-2}, \tag{2.10}$$

where Z is the charge state after ionization.

2.3   Single Particle Dynamics

Aside from Maxwell's equations, perhaps the most important equation to understanding the dynamics of a plasma is the Lorentz force equation:

$$\frac{\partial \mathbf{p}}{\partial t} = q(\mathbf{E} + \mathbf{v} \times \mathbf{B}), \tag{2.11}$$

where $\mathbf{p} = \gamma m \mathbf{v}$ is the relativistic particle momentum and $\gamma = 1/\sqrt{1 - \mathbf{v}^2/c^2}$ is the Lorentz factor. This equation defines the two ways that a charged particle can be accelerated by electric and magnetic fields: in the direction of electric fields and perpendicular to magnetic fields.

In non-relativistic laser interactions we can generally set $\gamma = 1$ and take the acceleration due to magnetic fields to be negligible because it is a factor $\mathbf{v}/c$ smaller than the electric field contribution. In relativistic interactions, the magnetic field contribution can become comparable to the electric field contribution, causing the particles to be accelerated along the direction of the laser propagation. In solid target interactions, this magnetic field component in conjunction with the electric field accelerates electrons into the target as will be discussed in Section 2.6.4.

In this thesis we will see interactions where strong magnetic and electric fields form in the plasma that are not oscillatory. Consider the effect of a static magnetic field in the z-direction perpendicular to velocity of a particle. The particle's energy cannot change in a static magnetic field, therefore γ is constant. This gives an equation for the acceleration in the x and y-direction:

$$\frac{\partial v_x}{\partial t} = \frac{q}{\gamma m} v_y B_z, \tag{2.12}$$

$$\frac{\partial v_y}{\partial t} = -\frac{q}{\gamma m} v_x B_z. \tag{2.13}$$

Taking the second derivative of Eqn. 2.13 and substituting into Eqn. 2.12 gives the equation:

$$\frac{\partial^2 v_x}{\partial t^2} = -\frac{q^2}{\gamma^2 m^2} B_z^2 v_x. \tag{2.14}$$

Substituting a guess of $v_x = v_\perp \cos(\omega_c t)$ and solving for ω_c will give:

$$\omega_c = \frac{|qB|}{\gamma m}, \tag{2.15}$$

the cyclotron frequency. Integrating the velocity gives the radius with which the particle will orbit in the magnetic fields known as the Larmor radius:

$$r_L = \frac{\gamma m v_\perp}{|qB|}. \tag{2.16}$$

The ratio of the cyclotron frequency to the rate at which the orbiting particles experience collisions (introduced in the next section) is known as the Hall parameter and defines how magnetized the plasma is. If the particles experiences multiple collisions during the time of a single orbit than they are not magnetized. The plasma is said to be magnetized if particles can on average perform multiple orbits without experiencing a collision.

2.3.1 Collisions

Collisionality is a term that will show up in this thesis as a way of defining what regime phenomena are being studied in. Collisions in plasmas appear in the form of Coulomb collisions where a charged particle propagates towards another charged particle and is deflected by the electric field of the particle. The rate at which these collisions occur is defined by $\nu_{col} = n\sigma_{col}u$, where σ_{col} is the collision cross section in units of length squared, n is the number density of background charged particles, and u is the speed the test particle moves toward the background plasma with. The collisional cross-section is defined as the area surrounding a background particle within which a test particle would be deflected by 90 degrees. To find this cross section we follow the derivation by Chen [87]. First we note that the force on the test particle is:

$$F = -\frac{e^2}{4\pi\epsilon_0 r^2},\tag{2.17}$$

if the test particle is an electron and the background particle is a proton. The interaction time is approximately $T \approx r_0/u$ where r_0 is the initial distance from the test to background particle perpendicular to the direction of propagation (Fig. 2.2). Multiplying F by T gives the change in momentum which is $\sim mu$ for a 90 degree deflection. Solving for r_0,

$$r_0 = \frac{e^2}{4\pi\epsilon_0 mu^2},\tag{2.18}$$

and noting $\sigma_{col} = \pi r_0^2$ gives,

$$\nu_{ei} = \frac{ne^4}{16\pi\epsilon_0^2 m^2 u^3}.\tag{2.19}$$

This is the large angle collision rate, however small angle collisions are much more likely and can be found by multiplying by the Coulomb logarithm $\ln \Lambda_c$. The Coulomb logarithm comes from a diverging integral over scatting angle and can be written as the natural log of the ratio of the maximum and minimum initial distances from the test to background particle, $\ln(b_{max}/b_{min})$ [88]. The value of b_{max} is taken to be the Debye length, $\lambda_D = \sqrt{\frac{\epsilon_0 k_B T_e}{ne^2}}$
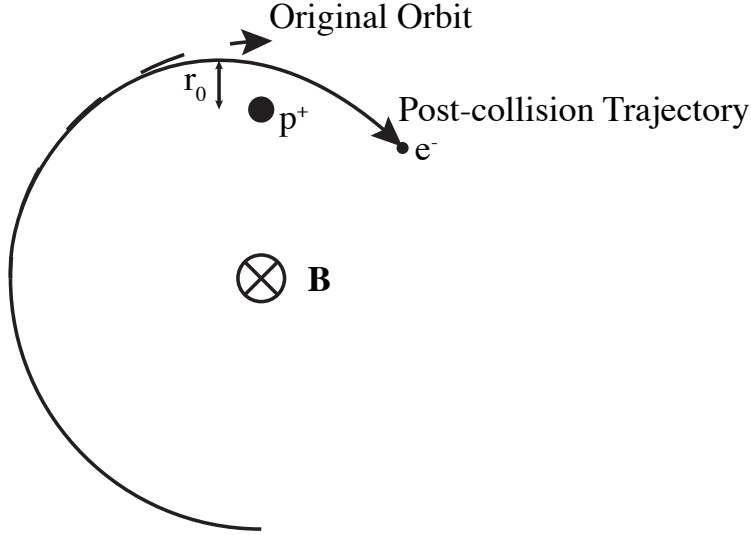
Figure 2.2: Electron orbiting in a magnetic field experiences a collision with a proton causing it break from its original trajectory.

assuming that collisions occur faster than ions can respond. The value of b_{min} is taken to be $r_c = e^2/4\pi\epsilon_0 k_B T_e$ where T_e is the electron temperature and k_B is the Boltzmann constant.

For the purpose of categorizing the physics of systems the important parameter is the mean free path $\lambda_{mfp} = u_{th}/\nu_{ei}$, where u_{th} is the thermal velocity. This defines the characteristic distance that an electron will travel before experiencing a collision. If this distance is small compared to the system size then the system is collisional. If it is large compared to the system size then the system is said to be collisionless. The majority of the physics presented in this thesis are in the collisionless regime.

2.4 Electromagnetic Wave Propagation in Plasma

At the start of this chapter we used the terms overdense and underdense, two terms that will be defined here. To understand how a laser will propagate through a plasma we must find the dispersion relation for an electromagnetic wave through a material where electrons
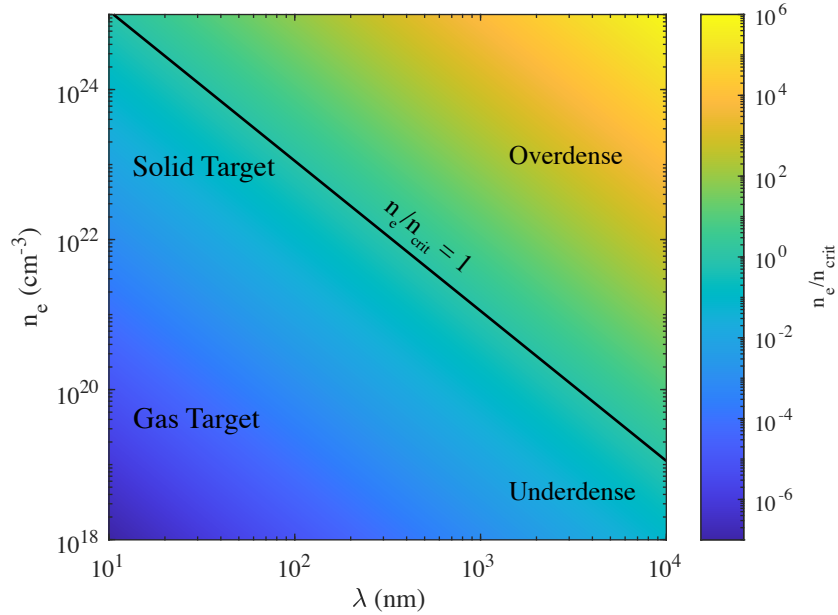
Figure 2.3: A plot of the densities required to be over or underdense for a particular laser wavelength.

are free to oscillate. To derive the dispersion relation we start with Ampère's law:

$$\nabla \times \mathbf{B} = \mu_0 \left(\mathbf{J} + \epsilon_0 \frac{\partial \mathbf{E}}{\partial t} \right). \tag{2.20}$$

One then takes the derivative with respect to time and substitutes $\partial \mathbf{B}/\partial t$ for $\nabla \times \mathbf{E}$ from the Maxwell-Faraday equation. A plane electric field of the form:

$$\mathbf{E} = E_0 e^{i(kz - \omega t)} \hat{x} \tag{2.21}$$

is substituted into the resulting equation. This gives:

$$-k^2 \mathbf{E} = \mu_0 \frac{\partial \mathbf{J}}{\partial t} - \frac{\omega^2}{c^2} \mathbf{E} \tag{2.22}$$

where $\mathbf{J} = -e n_e v_x$ is due to electron motion because ions are too slow to respond to the fields. This equation is then linearized and the following non-relativistic equation of motion

23

for the fast motion of the electrons is used:

$$\frac{\partial v_{x1}}{\partial t} = -\frac{e}{m_e}E_x.$$ (2.23)

After some algebra the following dispersion relation is found:

$$\omega^2 = \omega_{pe}^2 + k^2 c^2,$$ (2.24)

where $\omega_{pe} = \sqrt{\frac{n_e e^2}{m_e \epsilon_0}}$ is the electron plasma frequency. This is the characteristic rate at which electrons with a density n_e respond to perturbations. From Eqn. 2.24, if $\omega < \omega_{pe}$ then k is imaginary and if substituted into Eqn. 2.21, the wave is seen to rapidly attenuate as it propagates in the z-direction. The density at which the onset of attenuation occurs is the critical density:

$$n_{crit} = \frac{\omega_L^2 m_e \epsilon_0}{e^2},$$ (2.25)

where ω has been replaced with ω_L, the laser frequency. For $n_e > n_{crit}$ the electrons can respond to the laser, causing it to reflect from the plasma. This is known as an overdense interaction. Conversely when $n_e < n_{crit}$ the laser can propagate in the plasma and is known as an underdense interaction as shown in Fig. 2.3.

2.5   Ponderomotive Force

The ponderomotive force occurs as a result of spatial gradients in the laser electric field. If we consider the movement of an electron in the oscillating field of a plane wave, the electron will simply follow the oscillations of the electric field. However if we now consider the motion of an electron in an oscillating electric field with a spatial gradient one finds that over a number of oscillations the electron is accelerated in the direction of weakening field, i.e., in the opposite direction of the gradient. Intuitively, this is because the electron will experience an oscillating field that pushes them from the center of the laser pulse outward during the

first half of the laser period. The electron begins the second half the laser period away from the center of the pulse in a region where the fields are weaker, therefore it will feel a smaller returning force and will not make it back to the center of the laser pulse when the next laser period begins. The accumulation of this force imbalance during each laser cycle is known as the ponderomotive force.

To write this mathematically, we follow the derivation presented by Gibbon by first considering laser fields with a gradient [79],

$$\frac{\partial v_y}{\partial t} = -\frac{e}{m_e} E_y(y).$$ (2.26)

Taylor expanding $E_y(y)$ gives:

$$E_y(y) \approx E_0(y) \cos \phi + y \frac{\partial E_0(y)}{\partial y} \cos \phi + ...,$$ (2.27)

where $E_0(y)$ represents the spatial distribution of the laser electric field and $\cos \phi$ represents the oscillation of the field where $\phi = \omega t - kx$ for a wave propagating in the x-direction. The zeroth order term substituted into the Lorentz force equation simply gives the oscillation velocity which when integrated gives:

$$y^{(0)} = \frac{v_{osc}}{\omega} \cos \phi.$$ (2.28)

This can be substituted for y in the first order term of the Taylor expansion to give:

$$\frac{\partial v_y^{(1)}}{\partial t} = -\frac{e^2}{m_e^2 \omega^2} E_0 \frac{\partial E_0(y)}{\partial y} \cos^2 \phi.$$ (2.29)

Averaging over a laser cycle and multiplying by electrons mass forms the non-relativistic

version of the ponderomotive force:

$$F_p = -\frac{e^2}{4m_e\omega^2}\frac{\partial E_0^2}{\partial y}. \tag{2.30}$$

The relativistic ponderomotive force can be derived starting from the fluid version of the Lorentz force:

$$\frac{\partial \mathbf{p}}{\partial t} + \mathbf{u}\cdot\nabla\mathbf{p} = -e\mathbf{E} - e\mathbf{u}\times\mathbf{B}. \tag{2.31}$$

The fields can be written as vector potentials by using $\mathbf{E} = -\partial\mathbf{A}/\partial t$ and $\mathbf{B} = \nabla\times\mathbf{A}$. Additionally, if we use the vector identity $\mathbf{u}\times(\nabla\times\mathbf{A}) = (\nabla\mathbf{A})\cdot\mathbf{u} - (\mathbf{u}\cdot\nabla)\mathbf{A}$ we get:

$$\frac{d}{dt}(\mathbf{p} - e\mathbf{A}) = -e(\nabla A)\cdot\mathbf{u}, \tag{2.32}$$

where $\frac{d}{dt} = \frac{\partial}{\partial t} + (\mathbf{u}\cdot\nabla)$ is the total derivative. The total derivative comes from taking the derivative with respect to time of some quantity that has a coordinate system that is time dependent e.g. $\mathbf{u}(t, x(t), y(t), z(t))$, the velocity of some fluid element that is being tracked in a system. The momentum is then separated into fast and slow components $\mathbf{p} = \mathbf{p}^f + \mathbf{p}^s$ where $d\mathbf{p}^f/dt \gg d\mathbf{p}^s/dt, \nabla A$. Therefore $\mathbf{p}^f = e\mathbf{A}$ from Eqn. 2.32. The slow variation can be extracted from this equation by taking the average over the oscillating momentum:

$$\mathbf{p}^s = \frac{1}{2\pi}\int_0^{2\pi}\mathbf{p}\,d\xi, \tag{2.33}$$

where ξ is the phase of the oscillating momentum. Noting that $(\nabla\mathbf{A})\cdot\mathbf{A} = \frac{1}{2}\nabla(\mathbf{A}^2)$ and taking the time average of Eqn. 2.32 gives:

$$\frac{d\mathbf{p}^s}{dt} = -\frac{e}{2\langle\gamma\rangle m_e}\nabla(\langle A^2\rangle), \tag{2.34}$$

where $\langle\rangle$ represents the time average. This is the relativistic ponderomotive force. This can be written in a few different ways by noting that $a = eA/m_e c$, $\langle a^2\rangle = a_0^2$ for a circularly

polarized laser and $\langle a^2 \rangle = a_0^2/2$ for a linearly polarized laser. Additionally $\langle \gamma \rangle = \sqrt{1 + \langle a^2 \rangle}$.

2.6 Laser Absorption

In Section 2.2 the mechanisms for laser ionization were covered. Once a plasma has been generated through ionization, a fraction of the remaining energy in the laser pulse will be converted to kinetic energy of the electrons followed by the ions. In the interaction of a spatially uniform laser pulse with an electron, the electron will oscillate in the laser fields. However there will be no net energy gain, and therefore there must be some other mechanism to transfer energy to the plasma. Although there are several mechanisms for electrons to be accelerated, the main ways that bulk plasma heating occurs is through the generation of plasma waves followed by Landau damping, or by the acceleration of electrons followed by collisions.

2.6.1 Inverse Bremsstrahlung or Collisional Absorption

For the long-pulse moderate intensity inteactions ($I_L < 10^{15}$ W/cm^2) discussed in this thesis, the dominant absorption mechanism is inverse bremsstrahlung or collisional absorption. In the interaction of a laser pulse with an electron that is not bound to an atom, although the electron will oscillate in the laser field, it will gain no net energy. To transfer energy to the plasma the electron must experience a collision, such that it becomes out of phase with the laser fields. To model this process we must add a collisional term to the Lorentz force equation:

$$\frac{\partial u_e}{\partial t} = -\frac{e}{m_e}\mathbf{E} - u_e \nu_{ei}. \tag{2.35}$$

If u_e and E are $\propto \exp(\mathbf{k} \cdot \mathbf{r} - \omega t)$ then one can use the above force equation with Ampères law and the Maxwell-Faraday equation to obtain the following dispersion relation:

$$\left(\frac{kc}{\omega}\right)^2 = 1 - \frac{\omega_p^2}{\omega^2} + i\nu_{ei}\frac{\omega_p^2}{\omega^2}. \tag{2.36}$$

The imaginary part of k, the rate at which the laser is attenuated, is given by:

$$k_{im} = \frac{\nu_{ei}}{2c} \left(\frac{n_e}{n_{crit}} \right) \sqrt{1 - \frac{n_e}{n_{crit}}}.$$ (2.37)

From Eqn. 2.19 we can note that collisions become less important as the plasma temperature increases, therefore this mechanism becomes less important as laser intensity increases. In Chapter 5 a hydrodynamic simulation is performed to generate an accurate long-pulse laser generated plasma plume. Inverse bremsstrahlung is used to calculate the laser absorption in that simulation.

2.6.2   Resonance Absorption

Resonance absorption is an absorption mechanism that appears in overdense interactions. It requires a laser pulse to be obliquely incident on a plasma gradient that increases to some density in excess of the critical density. In this interaction, the laser will not propagate to the critical density and reflect, it will instead propagate to the point where $n_e = n_{crit} \cos \theta$, where θ is the angle of incidence. For s-polarized light, where the electric field is perpendicular to the plane of incidence, the fields oscillate electrons along lines of constant density and absorption does not occur. For p-polarized light, where the electric field is in the plane of incidence, electrons oscillate along density gradients and plasma waves are driven. These plasma waves occur at the critical density position, however we noted that the laser field are reflected before this position. Instead, the fields must tunnel to the critical density position where a resonant interaction occurs and plasma waves are driven. These plasma waves give up their energy to the plasma through Landau damping where electrons moving near the phase velocity of the plasma wave are accelerated.

The fraction of absorbed light is given by:

$$f_{abs} \approx \frac{\phi(\tau)^2}{2},$$ (2.38)

where,

$$\phi \approx 2.3\tau \exp\left(-\frac{2}{3}\tau^3\right), \tag{2.39}$$

$$\tau = \left(\frac{\omega L}{c}\right)^{1/3} \sin\theta. \tag{2.40}$$

This is true for a plasma with a linear density gradient that has a slope $L = \nabla n/n$ known as the scalelength. The maximum absorption occurs when the angle of incidence is:

$$\theta_{max} \approx \sin^{-1}\left[0.8\left(\frac{c}{\omega L}\right)^{1/3}\right] \tag{2.41}$$

2.6.3 Brunel or Vacuum Heating

Brunel heating is the dominant mechanism for heating in overdense targets with sharp density gradients when the laser is obliquely incident on the interface and p-polarized. As the laser electric field interacts at the sharp density gradient it pulls electrons from the interface on the first half of the laser period and accelerates the electrons back into the target on the second half of the laser period. The laser field can only penetrate up to the skin-depth into the target, therefore electrons accelerated into the target can escape the laser fields and propagate through the target, eventually giving up energy through collisions. The electric field that pulls the electrons from the interface is from the standing wave formed by the incident and reflected laser light:

$$E_d = 2E_L \sin(\theta). \tag{2.42}$$

If the electrons are pulled out as a sheet they will have some surface number density σ and will form a picture similar to a capacitor which has an electric field $E = e\sigma/\epsilon_0$. Therefore the number density is:

$$\sigma = \frac{2\epsilon_0 E_L \sin(\theta)}{e} \tag{2.43}$$

When this sheet of charge is driven back into the bulk target it will have a velocity $v_d = 2v_{os}\sin(\theta)$ where $v_{os} = eE_L/m_e\omega_L$ is the oscillation velocity of an electron in the laser field.

This process will result in electrons bunched at the laser frequency ω_L. The ratio of the energy per unit area carried by the electrons to the intensity of the laser is:

$$\eta_{abs} = \frac{4}{\pi} \frac{\sin^3(\theta)}{\cos(\theta)} a_0 \tag{2.44}$$

Two corrections must be made to this equation for it to accurately predict the absorption. First, the reflected laser light that forms the standing wave must be reduced by the absorption. Secondly, the relativistic kinetic energy must be used for the particles. This results in the corrected relativistic equation:

$$\eta_{abs} = \frac{1}{\pi a_0} f \left[(1 + f^2 a_0^2 \sin^2(\theta))^{1/2} - 1 \right] \frac{\sin(\theta)}{\cos(\theta)}, \tag{2.45}$$

where $f = 1 + (1 - \eta_{abs})^{1/2}$. This is then a transcendental equation and must be solved numerically. More complex equations are required to model heating with finite scale-lengths. In the case where $L/\lambda = 0.1$ absorption reaches peak values of $\sim 70\%$ [89].

2.6.4 j×B Heating

$j \times B$ heating is a relativistic effect that appears as result of the magnetic field term in the Lorentz force becoming important when particle velocities approach c:

$$n_e \frac{\partial \mathbf{p}}{\partial t} + n_e (\mathbf{u} \cdot \nabla) \mathbf{p} = -e n_e \mathbf{E} - \mathbf{j} \times \mathbf{B}. \tag{2.46}$$

Previously when we discusses the ponderomotive force although we gave a general equation where the force could even act along the laser propagation direction, we motivated the force by transverse gradients in the laser field due to focusing that would result in transverse forces. We know from previous sections that a non-relativistic electron will simply oscillate along the electric field with a velocity v_{osc}. This is approximately true because the ratio of magnetic field force to electric field force is very small $|(\mathbf{u} \times \mathbf{B})|/|\mathbf{E}| \approx u/c \ll 1$ because $B/c = E$

for an electromagnetic wave. However, as $|\mathbf{u}|$ approaches c the magnetic field begins to accelerate the electron longitudally. To express this process through equations we follow very similar steps to what was done for the relativistic ponderomotive force derivation. We take a wave propagating along the x-direction polarized in the y-direction $A(x,t) = A(x)\sin(\omega_L t)\hat{y}$. Placing this into the Lorentz force equation and solving for the momentum in the y-direction we find $p_y = eA$. Now solving for the force in the x-direction one finds the following equation:

$$\frac{dp_x}{dt} = -\frac{m_e}{2}\frac{\partial v_{osc}(x)^2}{\partial x}\sin(\omega_L t)^2 = -\frac{m_e}{4}\frac{\partial v_{osc}(x)^2}{\partial x}(1 - \cos(2\omega_L t)). \tag{2.47}$$

This force is made up of two components: the standard constant ponderomotive force, and a second force that at two times the laser frequency. This causes bunches of electrons to be accelerated into the target similar to the Brunel mechanism. The resultant temperature can be approximated as [79]

$$T_{j \times B} = m_e c^2 \left[(1 + 0.73 I_{18} \lambda_\mu^2)^{1/2} - 1\right]. \tag{2.48}$$

This mechanism is most important to overdense interactions as normal-incidence, such as those studied in Chapter 6.

2.7 Hole Boring

In underdense plasmas as a laser propagates through the plasma it will rapidly displace the electrons near the center of the pulse out radially through the ponderomotive force due to transverse gradients in the electric field. This generates a plasma channel that has a net positive charge due to the left-over ions that move much slower than the electrons. This process is known as channeling. The analogous process in overdense plasmas is the hole boring process.

The process works as follows: the laser channels through the underdense plasma to the

critical density, the laser then displaces electrons longitudinally through the ponderomotive force into the dense plasma. The ions are subsequently pulled by the electric field set up by the electrons. The pressure balance at the interface between the ions and radiation pressure is:

$$(1 + R)I_L/c = 2M_i u_f^2 n_i, \qquad (2.49)$$

where the ion front moves with a speed u_f, has a density n_i, a mass M_i, and reflects a fraction R if the incident light. Prior to reaching the relativistic critical density $\gamma_{osc} n_{crit}$ where $\gamma_{osc} = \sqrt{1 + (1 + R)a_0^2/2}$ the laser will rapidly heat the electrons and R will be small. For a plasma with an exponential density gradient $n_i(x) = (\gamma_{osc} n_{crit}/Z) \exp[(x - x_c)/l_s]$ the evolution of the position of the ion front is given by [90]

$$x_f(t) = x_c + 2l_s \ln \left[1 + t\frac{c}{2l_s} \left(\frac{m_e Z}{2M_i} \frac{\gamma_{osc}^2 - 1}{\gamma_{osc}} \right)^{1/2} \right]. \qquad (2.50)$$

Several equations for the hole boring position or velocity exist and most are modified versions of this equation. In Chapter 6 we found this equation matches simulations quite well and is used in our theory.

2.8 Strong Field Quantum Electrodynamics

Quantum electrodynamics (QED) is the study of the quantum processes in dynamic electric and magnetic field interactions. Specifically, it is the study of the way radiation and charged particles interact. Strong field QED (SFQED) is the study of these interactions in a regime where interacting fields are so energetic that quantum processes with very low probabilities at standard field strengths become important. The two main processes that become important and are relevant to this thesis are multi-photon Compton emission and pair creation which will be discussed in the following sections. The primary reference for the following section is the paper by Ridgers *et al.* [91]. SFQED effects occur when field strengths become

comparable to the Schwinger or critical field:

$$E_s = \frac{m_e^2 c^3}{e\hbar} = 1.3 \times 10^{18} \text{ V/m}. \tag{2.51}$$

This field is defined by being the field necessary to accelerate an electron to gain kinetic energy equal to its rest mass within a Compton length. The Compton length is the wavelength of light that would have the same energy as a particle with rest mass energy mc^2. This is such an extreme field that it can directly generate particles from the vacuum. In terms of intensity this corresponds to an $\sim 10^{29}$ W/cm^2 laser pulse. Such an intensity is well outside of current laser technology and without significant advances in laser technology may not exist for many years. However, this does not mean that SFQED cannot be studied in the laboratory. By noting that electric and magnetic fields are not Lorentz invariant, we can see that there a simple trick that can be used to increase the relative field strengths felt by an electron. If the electron propagates through the fields with some velocity that is a large fraction of c, then it will see much larger field strengths in its rest frame. The ratio of the fields it feels to the Schwinger field is given by:

$$\eta = \frac{|F^{\mu\nu} p_\nu|}{mE_s}, \tag{2.52}$$

where $F^{\mu\nu}$ is the EM field tensor and p_ν is the relativistic 4-momentum. This terminology may be confusing if one is not familiar with special relativity. They are written as:

$$F^{\mu\nu} = \begin{bmatrix} 0 & -E_x/c & -E_y/c & -E_z/c \\ E_x/c & 0 & -B_z & B_y \\ E_y/c & B_z & 0 & -B_x \\ E_z/c & -B_y & B_x & 0 \end{bmatrix}, \tag{2.53}$$

$$p_\nu = \gamma m (c, -v_x, -v_y, -v_z). \tag{2.54}$$

These structures are convenient in special relativity because any set of quantities that form a 4-vector can be transformed as a set through both rotations and Lorentz transforms. Additionally, the Einstein summation convention, where indices that appear as both superscripts and subscripts are summed over (e.g. ν in Eqn. 2.52), allows for equations to be written in a concise way.

Returning back to the meaning of η, we can see that it is similar to a_0 in that it defines how important SFQED effects are in the interaction. Achieving a η close to 1 for a non-relativistic particle where $\gamma \approx 1$ as previous noted is non-trivial because it requires very strong fields. However, if the particle is highly relativistic then $v \approx c$ and $\gamma \gg 1$. This then reduces the required field strength in the lab frame by a factor of $\sim 2\gamma$ for a head-on collision. In the following sections the two lowest order processes that occur in SFQED will be reviewed.

2.8.1 Multi-photon Compton Emission

In standard QED one of the lowest order processes is Compton scattering whereby a photon scatters from a particle, giving energy to the particle. The inverse of this process is for a photon to be emitted from a particle. When a particle interacts with very strong fields where $\eta > 0.1$, multiple laser photons can interact with a particle to produce a much higher energy photon. This is known as non-linear inverse Compton scattering or multi-photon Compton emission. Standard inverse Compton scattering is defined by a photon energy dependent emission rate that results in a spectrum of emitted photon energy. This spectrum is the same as synchrotron radiation (radiation from high energy particles moving through a magnetic field). The classical spectrum overestimates the spectrum that is obtained in multi-photon Compton emission. Specifically, it overestimates high energy photon production. To reduce the spectrum we use the Gaunt factor $g(\eta) = P_{quantum}/P_{classical}$, where P is the power

spectrum. More explicity this equation is written as:

$$\mathbf{g}(\eta) = \frac{\int_0^{\eta/2} F(\eta,\chi)d\chi}{\int_0^\infty F_{cl}(\frac{4\chi}{3\eta^2})d\chi} = \frac{3\sqrt{3}}{2\pi\eta^2}\int_0^{\eta/2} F(\eta,\chi)d\chi. \tag{2.55}$$

For an ultra-relativistic particle the photons are emitted along the direction of the particle's momentum causing a decrease in momentum, this is known as radiation reaction. This force is written as:

$$F = -\frac{\mathbf{g}P_{cl}}{c}\hat{\mathbf{p}}, \tag{2.56}$$

where the radiated power is given by:

$$P_{cl} = \frac{2\alpha_f c}{3\lambdabar_c}m_e c^2\eta^2. \tag{2.57}$$

Here α_f is the fine structure constant, $\lambdabar_c$ is the reduced Compton length. In Eqn. 2.55 $\chi = (h\nu\eta)/(2\gamma m_e c^2)$ is the photon quantum efficiency parameter. One must be careful because in many QED papers the symbol χ will be used for what we have defined as η here. A useful fit for $\mathbf{g}(\eta) \approx [1 + 4.8(1+\eta)\ln(1+1.7\eta) + 2.44\eta^2]$.

The way radiation reaction affects the mean momentum $\langle\mathbf{p}\rangle$ and energy spread $\sigma^2 = \langle\gamma^2\rangle - \langle\gamma\rangle^2$ of a population of electrons is given by:

$$\frac{d\langle\mathbf{p}\rangle}{dt} = -\frac{\langle \mathbf{g}P_{cl}\hat{\mathbf{p}}\rangle}{c}, \tag{2.58}$$

$$\frac{d\sigma^2}{dt} = -2\frac{\langle\Delta\gamma \mathbf{g}P_{cl}\rangle}{m_e c^2} + \frac{\langle S\rangle}{m_e^2 c^4}. \tag{2.59}$$

Here $\Delta\gamma = \gamma - \langle\gamma\rangle$ and

$$S(\eta) = \frac{55\alpha_f c\gamma}{24\sqrt{3}\lambdabar\eta}m_e^2 c^4\eta^4 \mathbf{g}_2(\eta), \tag{2.60}$$

where $\mathbf{g}_2(\eta) \approx [1 + (1+4.528\eta)\ln(1+12.29\eta) + 4.632\eta^2]^{-7/6}$. The use of $\langle\rangle$ denotes the

moment of a quantity and is defined as:

$$\langle \psi(\mathbf{p}) \rangle \equiv \frac{1}{n_e} \int d^3\mathbf{p} \psi(\mathbf{p}) f(\mathbf{x}, \mathbf{p}, t), \qquad (2.61)$$

where f is the electron distribution function. From these equations we can see that radiation reaction will act on a distribution of electrons to reduce the mean particle γ. From the first term in Eqn. 2.59 the variance in the distrubution is reduced as high energy particles radiate more than low energy particle, but it is increased due to stochastic effects (second term). These equations will show up again in Chapter 6 when we discuss the measurement of magnetic fields using high energy electron beams.

2.8.2   Breit-Wheeler Pair Creation

The second process that will be discussed here is Breit-Wheeler pair creation, or in SFQED multi-photon pair creation. As will be shown in Chapter 6 this process is negligible for the laser intensities and interactions studied in this thesis, however it is still an important process for SFQED. The classical version of the process involves two photons combining to produce a single electron-positron pair $(\gamma\gamma \to e^-e^+)$. This process requires photons with a minimum combined energy of $2m_ec^2$. It also requires that these photons exist in a large enough density that the small cross-section can be overcome and pairs can be produced with a non-negligible probability. The SFQED version of this process involves the interaction of multiple photons to produce pairs $(\gamma + N\gamma' \to e^-e^+)$. Again, the photon energy must add up to $2m_ec^2$ however, this energy can be divided among several photons, therefore the photon energy requirement is less stringent.

Taken together the processes of multi-photon Compton emission and multi-photon Breit-Wheeler can form a population of pairs and photons that grow exponentially. If we start with a single electron in a laser field this electron can produce a high energy photon. This photon can then interact with the laser field to produce a pair. These pairs and the initial

36

electron can all radiate assuming they stay in the laser field and the laser has not been depleted. If this process continues it forms a pair cascade. In astrophysics pair cascades have been theorized to occur at the poles of pulsars [92]. Experimental setups have been proposed to study these cascades [93, 94].

2.9 Shocks

A shock is a mechanism to rapidly change the properties of a medium when some object or perturbation moves through a medium faster than it can respond. This response time is defined by the fastest rate of information transfer in the medium, generally the sound speed, however this can also be the Alfvén speed in magnetized plasmas. If a perturbation moves through a system in excess of the sound speed, the system rapidly attempts to respond by changing its properties such that the perturbation no longer moves faster than the system can respond. The shock appears as an abrupt transition from the plasma that cannot respond (upstream) to the plasma that can respond (downstream). The way this shock forms and its properties depend greatly on the collisionality of the system. If the mean-free-path is much smaller than the system size, then the shock will be mediated by collisions, however if the mean-free-path is much larger than the system then collisions cannot be important and the shock must be mediated by some collisionless mechanism. Here we will describe the formation of both types of shocks, however for the purpose of this thesis it is the collisionless shock formation that is important. For additional discussion of collisional shocks see [15].

2.9.1 Jump Conditions

In the highly collisional regime the plasma can be modeled as a fluid, the shock shows up as a rapid change in density, pressure, and temperature that travels through the plasma in

excess of the sound speed given by:

$$C_s = \sqrt{\frac{Z k_B T_e}{m_i}}. \tag{2.62}$$

Although the perturbation exceeds the sounds speed, the single fluid equations still remain valid:

$$\frac{\partial \rho}{\partial t} = -\nabla \cdot (\rho \mathbf{u}), \tag{2.63}$$

$$\frac{\partial}{\partial t} (\rho \mathbf{u}) = -\nabla \cdot (\rho \mathbf{u} \mathbf{u}) - \nabla p, \tag{2.64}$$

$$\frac{\partial}{\partial t} \left(\frac{\rho u^2}{2} + \rho \epsilon \right) = -\nabla \cdot \left[\rho \mathbf{u} \left(\epsilon + \frac{u^2}{2} \right) + p \mathbf{u} \right], \tag{2.65}$$

where ρ is the mass density, p is the pressure, and ϵ is the internal energy. These equations are respectively the continuity equation, conservation of momentum, and conservation of energy. If we take the shock transition to happen over an infinitely small length, then the following jump conditions can be found:

$$\rho_1 u_1 = \rho_2 u_2 \tag{2.66}$$

$$\rho_1 u_1^2 + p_1 = \rho_2 u_2^2 + p_2 \tag{2.67}$$

$$\left[\rho_1 u_1 \left(\epsilon_1 + \frac{u_1^2}{2} \right) + p_1 u_1 \right] = \left[\rho_2 u_2 \left(\epsilon_2 + \frac{u_2^2}{2} \right) + p_2 u_2 \right]. \tag{2.68}$$

These equations define how the density, pressure, and energy density change moving from the shock upstream to downstream. Such equations are commonly used in shocks driven by high-energy long-pulse lasers in inertial confinement experiments and have been applied to collisionless shock, however the validity of their application to collisionless shocks is still being studied. Bret *et al.* studied the departure from Eqn. 2.66 in collionless shock simulations [95]. They found that for electrostatic shocks where steep electric fields separate the upstream from downstream, particle reflections cause the density jump to not be perfectly accurate,

differing by a few percent.

2.9.2   Collisionless Shocks

Collisionless shocks again form in systems where a perturbation moves in excess of the local speed of information propagation, however the shock is mediated purely through collisionless mechanisms, e.g. the growth of steep electric and/or magnetic fields. These shocks can form in many ways, but they primarily form due to streaming instabilities. For example there have been experiments studying Weibel mediated shocks where the Weibel instability initiates the formation of magnetized shocks [96]. If there is no magnetic field present then the shock will be purely electrostatic. This type of shock will be the main focus of Chapter 4 and is formed from nonlinear steepening of ion-acoustic waves. Simulations have shown that the parameter that defines the formation of a electrostatic or magnetized shock is the ratio of the electron temperature to the fluid velocity [51]. This is because the dominant or fastest growing instability depends on this ratio and will define what type of shock is formed.

The fundamental theory for electrostatic shocks comes from the work of Sagdeev [97]. The electrostatic shock is modeled simply as an electrostatic potential ϕ that is supported by kinetic electrons with a Boltzmann distribution $n_e(\phi) = e n_{e0} e^{e\phi/k_B T_e}$ and ions described as a fluid that interacts with the potential. To find the ion equation, we use conservation of mass and energy across the shock:

$$n_{i0} u_{io} = n_i u_i, \tag{2.69}$$

$$u_i^2 = u_{i0}^2 - \frac{2Ze\phi}{m_i}. \tag{2.70}$$

Combing these equations and solving for n_i gives:

$$n_i(\phi) = \frac{n_{io}}{\sqrt{1 - \frac{2Ze\phi}{u_{i0}^2 m_i}}}. \tag{2.71}$$

This equation and the electron distribution are then used in Poissons equation:

$$\nabla^2 \phi = e n_e - Z e n_i. \tag{2.72}$$

We normalize this equation using a new normalized potential $\hat{\phi} = e\phi/k_B T_e$. We can also note that the Mach number $M = u/C_s$, and we can normalize the length scale to the Debye length, $\chi = x/\lambda_D$ to give the equation:

$$\frac{\partial^2 \phi}{\partial \chi^2} = \exp(\hat{\phi}) - \frac{1}{\sqrt{1 - \frac{2\hat{\phi}}{M^2}}}. \tag{2.73}$$

If we now consider $\hat{\phi}$ to be some position and χ to be time, this is an equation of motion. By integrating with respect to $\hat{\phi}$ this then forms a conservation of energy equation:

$$\frac{1}{2}\left(\frac{\partial \hat{\phi}}{\partial \chi}\right)^2 = \exp(\hat{\phi}) + M^2 \sqrt{1 - \frac{2\hat{\phi}}{M^2}} + C \tag{2.74}$$

To find the constant of integration set $\partial \hat{\phi}/\partial \chi = 0$ when $\hat{\phi} = 0$. One finds that $C = -(1+M^2)$. The resultant equation can be written in the form:

$$\frac{1}{2}\left(\frac{\partial \hat{\phi}}{\partial \chi}\right)^2 + \Psi(\hat{\phi}) = 0. \tag{2.75}$$

In this equation $\Psi(\hat{\phi})$ is the Sagdeev potential which shows up in most collisionless shock theories. This potential represents the electron and ion pressure:

$$\Psi(\hat{\phi}) = P_i - P_e = M^2 \left(1 - \sqrt{1 - \frac{2\hat{\phi}}{M^2}}\right) - (\exp(\hat{\phi}) - 1) \tag{2.76}$$

This equation represents a solitary wave or soliton. To find the maximum speed that can be reached by this soliton set $\partial \hat{\phi}/\partial \chi = 0$ when $\hat{\phi} = \hat{\phi}_{max}$. Additionally we must note that once the potential of the soliton exceeds the kinetic energy of the ions they will no longer be able
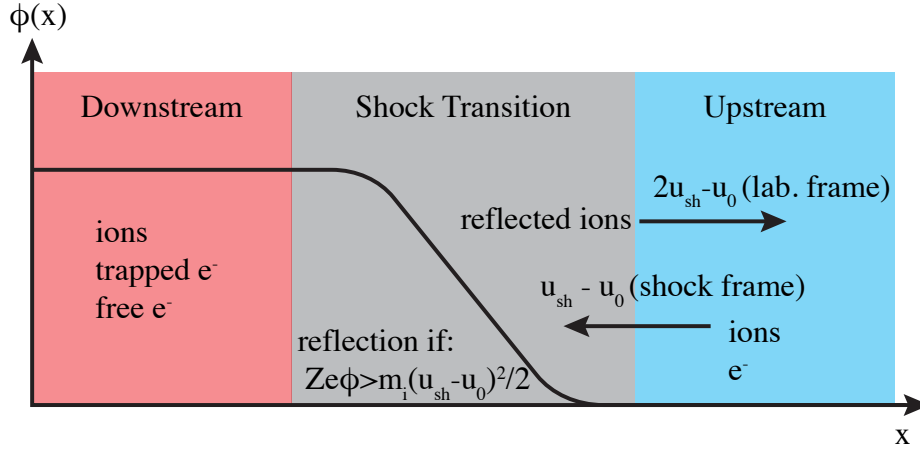
Figure 2.4: Standard steady-state shock picture used for more recent collisionless shock theory.

to pass the soliton:

$$Ze\phi > \frac{m_i u^2}{2}. \qquad (2.77)$$

Using the boundary condition and the maximum ϕ condition solving numerically we find $\hat{\phi}_{max} \approx 1.3$. Substituting back into Eqn. 2.77 gives:

$$M_{cr} = \frac{u}{\sqrt{Zk_B T_e/m_i}} \approx 1.6. \qquad (2.78)$$

This is known as the critical Mach number and defines the onset of ion reflection. For a graphical explanation of these equations see [87].

From the linearized equations for an ion acoustic wave it is not clear how a shock will form as the speed of an ion acoustic wave is the sound speed. To achieve higher Mach numbers and shock formation, non-linear theory must be used as it predicts wave-steepening and faster propagation speeds [98].

More recent laser-driven collisionless shock papers use the steady-state shock picture shown in Fig. 2.4. In the co-moving frame of the shock the upstream travels towards the shock at a speed u_s. The upstream is made up of unshocked electrons and ions and the

downstream consists of shocked electrons and ions. Between these two regions is the shock transition where the amplitude of the electrostatic potential increases from the upstream to the downstream. Electrons are able to move from the upstream to downstream freely, however only electrons with kinetic energies greater than the shock potential can move from the downstream to the upstream. Electrons with energies below the shock potential make up the "trapped" population. There were a few early papers on the distribution function of electrons trapped behind a potential wall. The common assumption for the distribution function is to use the maximum density trapping approximation where particles have a flat-top distribution, however this is not necessarily true for all shocks [99]. This shock picture was used by Sorasio *et al.* to derive equations for shocks with differing electron temperatures across the shock allowing for large Mach numbers [100]. Later, Stockem *et al.* adapted the theory to allow for relativistic electron temperatures [101]. We modify this theory in Chapter 4.

In both the more recent model and the theory of Sagdeev there is a critical Mach number above which ions are reflected. Ions which satisfy Eqn. 2.77 will be reflected. The velocity of these reflected particles is calculated as follows. Assume the shock is moving with a velocity u_{sh} and the ion is moving along this same direction with $u_0 < u_{sh}$. In the frame of the shock the ion approaches the stationary shock with a speed $-(u_{sh} - u_0)$ and is reflected back at $u_{sh} - u_0$. Converting back to the lab frame, one finds that the reflected ion has a velocity $2u_{sh} - u_0$ assuming the speeds are non-relativistic. Although this is for a single particle, if we consider an upstream ion distribution with a finite temperature, only the part of the distribution that satisfies the reflection condition will be reflected and the thermal spread will result in an energy spread in the reflected beam. These properties are included in the model of Malkov *et al.* [99].

2.10 Magnetic Field Generation in Laser-Solid Interactions

Magnetic fields are a fundamental component of our universe and can be generated in several ways in plasmas. If we consider the Maxwell-Faraday equation:

$$\frac{\partial B}{\partial t} = -\nabla \times E, \tag{2.79}$$

we can see that anywhere in the universe where there are electric fields that have a non-zero curl, magnetic fields will grow. The way these electric fields are formed are given by the non-ideal Ohm's law. There are several terms in the full Ohm's law, however for our discussion we care about the following truncated equation:

$$\mathbf{E} + \mathbf{u} \times \mathbf{B} = \eta \mathbf{J} - \frac{\nabla P_e}{e n_e}, \tag{2.80}$$

where $P_e = n_e k_B T_e$ is the electron thermal pressure. Taking the curl of this equation and substituting this equation for $\nabla \times \mathbf{E}$ in Eqn. 2.79 gives:

$$-\frac{\partial \mathbf{B}}{\partial t} + \nabla \times \mathbf{u} \times \mathbf{B} = \nabla \times \eta \mathbf{J} - \nabla \times \left(\frac{\nabla P_e}{e n_e} \right). \tag{2.81}$$

For the sake of this discussion we will focus on the magnetic field contribution from the second term on the right side of this equation. This contribution is known as the Biermann battery mechanism, however it is generally written in a different form [14]. To get to the standard form we follow the following steps. First, using the vector identity $\nabla \times \phi \mathbf{A} = \phi \nabla \times \mathbf{A} + \nabla \phi \times \mathbf{A}$:

$$-\frac{\partial \mathbf{B_{Biermann}}}{\partial t} = -\frac{1}{e n_e} \nabla \times \nabla P_e + \nabla \left(-\frac{1}{e n_e} \right) \times \nabla P_e \tag{2.82}$$

The curl of the gradient is zero which removes the first term on the right side. The second term can be further expanded by using the chain rule on ∇P_e assuming spatially varying temperature and density. Additionally, we use the distributive property of the cross-product to write:

$$\frac{\partial \mathbf{B_{Biermann}}}{\partial t} = -\frac{k_B}{en_e}\nabla n_e \times \nabla T_e - \frac{k_B T_e}{en_e^2}\nabla n_e \times \nabla n_e. \tag{2.83}$$

The second term is zero and using the anticommutative property of the cross-product we get the standard form of the Biermann battery:

$$\frac{\partial \mathbf{B_{Biermann}}}{\partial t} = \frac{k_B}{en_e}\nabla T_e \times \nabla n_e. \tag{2.84}$$

From this equation we can see that, in plasmas with perpendicular temperature and density gradients, magnetic fields will be generated. Such gradients occur in laser generated plasma plumes where the density of the plasma plume increases toward the target surface and the temperature decreases radially. These perpendicular gradients setup azimuthal magnetic fields within the plasma plume which have been measured in experiment [19, 102]. Two of these plumes have been generated side-by-side on foils to create a magnetic reconnection geometry [34].

Experiments and simulations both show that Biermann is the dominant field generation mechanism for moderate intensity lasers. It was also shown by Shukla *et al.* that Biermann is dominant outside the focal volume for $a_0 \approx 1$ with Weibel field generation being the dominant mechanism within the focal volume [103]. However, field generation for $a_0 \gg 1$ in the highly relativistic regime has not been studied. A simple model was derived from the integral form of Maxwell's equations where the field generation results from relativistic electrons streaming along the surface of the target by Schumaker *et al.* [71]. First we assume that the interaction of a laser pulse on a solid target is azimuthally symmetric and the laser

propagates in the z-direction. Start with the integral form of the Ampère-Maxwell equation:

$$\oint_{\partial \Sigma} \mathbf{B} \cdot d\ell = \mu_0 \left(\iint_{\Sigma} \mathbf{J} \cdot d\mathbf{S} + \epsilon_0 \frac{d}{dt} \iint_{\Sigma} \mathbf{E} \cdot d\mathbf{S} \right). \tag{2.85}$$

We want to find the azimuthal field above the target at some position z. Assuming the displacement current normal to the target is small:

$$B_\theta(r, z, t) \approx \frac{1}{c^2 r} \frac{d}{dt} \int_0^r E_z(r', z, t) r' dr'. \tag{2.86}$$

Next we combine the integral form of Gauss' law with the continuity equation:

$$\iint_{d\Omega} \mathbf{E} \cdot d\mathbf{S} = \frac{1}{\epsilon_0} \iiint_{\Omega} \rho dV, \tag{2.87}$$

$$\frac{d\rho}{dt} = -\nabla \cdot \mathbf{J}. \tag{2.88}$$

We can form an equation to replace the radial integral of E_z in Eqn. 2.86 by taking the time derivative of Eqn. 2.87 and substituting Eqn. 2.88 for $d\rho/dt$. This results in the final equation:

$$B_\theta(r, z, t) \approx -\mu_0 \int_z^\infty j_r(r, z', t) dz'. \tag{2.89}$$

In Chapter 6 we find that this equation can be used in simulations to quite accurately construct the magnetic fields outside the focal volume. We build upon this equation allowing for estimates of magnetic fields for interactions in the range of $a_0 = 50$ to 500 starting from laser parameters.

2.11 Magnetization

In Section 2.3 it was noted that the magnetization of a plasma depends on how well the particle trajectories couple to magnetic field lines. A different definition of magnetization

appears in astrophysics in the form of the parameter σ. It does not compare the timescales of particles orbiting in magnetic fields to collisional timescales; instead, it is the ratio of the magnetic enthalpy density to the relativistic plasma enthalpy density. It is therefore a comparison between the energy that exists in the magnetic fields to the energy in the plasma. Before showing the equation for σ, we should note why it is important. In plasmas, shear Alfvén waves can be generated due to perturbations transverse to the magnetic field lines. The field lines oscillate due to magnetic tension which pulls on the plasma. The speed at which these waves travel, the Alfvén velocity can be written in terms of σ:

$$V_A = c\sqrt{\frac{\sigma}{1+\sigma}}. \tag{2.90}$$

Notably, this velocity defines the outflow speed and therefore the rate of magnetic reconnection. If $\sigma \gg 1$ then $V_A \approx c$ and the reconnection outflow can be relativistic. If $\sigma \ll 1$ then $V_A \approx c\sqrt{\sigma}$.

Magnetization is defined as:

$$\sigma \equiv \frac{B^2}{\mu_0 w}, \tag{2.91}$$

where B is the magnetic field, and w is the relativistic enthalpy density of the plasma i.e., the sum of the internal energy density (which includes the rest-mass energy density $n_s m_s c^2$) and the pressure p_s, summed over the particle species s. For a polytropic gas the pressure is related to the density as $p_s \propto n_s^{\gamma_a}$, where γ_a is the adiabatic index [15]. For a relativistic gas, where the temperature $k_B T_s \gg m_s c^2$, $\gamma_a = 4/3$. While for a non-relativistic gas $k_B T_s \ll m_s c^2$, $\gamma_a = 5/3$. In either case, the pressure is $p_s = n_s k_B T_s$ where k_B is the Boltzmann constant and T_s is the temperature of the particular species. Pressure is related to internal energy as $p/(\gamma_a - 1)$. Therefore, for an ultra-relativistically hot plasma:

$$\sigma_{hot} = B^2/\mu_0 \sum_s (4 n_s k_B T_s). \tag{2.92}$$

While in the limit of sigma where $k_B T_s \ll m_s c^2$, i.e. a relativistically cold plasma:

$$\sigma_{cold} = B^2/\mu_0 \sum_s \left(n_s m_s c^2 + \frac{5}{2} n_s k_B T_s \right). \tag{2.93}$$

In this limit, the denominator of the equation is dominated by the rest mass energy density of the particles. If the particles have similar densities then σ_{cold} is dominated by the particle with the largest mass. This form of σ is quite useful because except for a factor of $1/2$, it gives the amount of energy in the magnetic field per particle, normalized to the particle rest mass energy. Magnetic reconnection converts magnetic field energy to particle kinetic energy, therefore σ_{cold} can be used to estimate how energetic particles will be in the reconnection outflow. Additionally, we can note that if $\sigma_{cold} \ll 1$, then when substituted into Eqn. 2.90 we can retrieve the classical Alfvén speed:

$$V_A = \frac{B}{\sqrt{\mu_0 n_i m_i}}. \tag{2.94}$$

Here we have assumed that the denominator is dominated by a single ion species with mass m_i and density n_i.

In the context of laser-plasma interactions it is likely that electrons will be ultra-relativistically hot, while ions will be relativistically cold, therefore the use of σ_{hot} or σ_{cold} will depend on the particle species. Additionally, in ultra-intense laser-solid interactions there may be regions where the electrons are coupled to the magnetic fields while the ions are not, or regions where only electrons exist, therefore $n_e \gg n_i$ and we can define electron magnetization:

$$\sigma_{hot,e} = \frac{B^2}{4\mu_0 n_e k_B T_e}. \tag{2.95}$$

From this equation, varying T_e and keeping all other values constant, we can note that $\sigma_{hot,e}$ decreases with increasing T_e, therefore hot relativistic electrons will have a smaller $V_{A,e}$ than cold electrons.

Finally, it is important to note which frame σ should be calculated in. In reconnection studies σ is commonly calculated in the reconnection upstream, i.e. the region where magnetic fields have yet to reconnect. In that frame the plasma is stationary. In Chapter 6 we calculate σ in the frame co-moving with the relativistic electrons traveling along the surface of the target. In the two-beam reconnection geometry this outflow from the laser focal volume would make up the reconnection upstream. The frame σ should be calculated in will depend on the experimental geometry and how the magnetic fields are expected to interact.

CHAPTER 3

Methods and Capabilities

3.1 OMEGA EP

In Chapter 5 experimental work performed on the OMEGA Extended Performance (EP) laser system at the University of Rochester Laboratory for Laser Energetics is presented. This facility houses two laser systems: the OMEGA laser system; a 60 beam high-energy system designed primarily for inertial confinement fusion studies; and the OMEGA EP system, a 4 beam system used for a diverse set of experiments [104]. OMEGA EP operates as a user facility where researchers are awarded a set number of shot days to have their experiments be performed by a large team of technicians and scientists. This is necessary as the laser system is extremely large and performs new experiments everyday, therefore the facility must operate very efficiently.

OMEGA EP has several capabilities that allow us to run experiments that cannot be performed elsewhere. It includes 4 highly energetic beams, two of which can be compressed to short pulses [105]. The short-pulse beams originate as $\sim$ 200 fs pulses before being temporally stretched and amplified through optical parametric amplification (OPA). The combination of these processes is known as optical parametric chirped pulse amplification (OPCPA) and allows the initial signal pulse to see large gain while maintaining its bandwidth. Two stages of OPCPA allow for the initial pulse to be amplified from 2 nJ to 250 mJ. The long-pulse beams originates as a continuous wave output from a commercial oscillator. This

beam is shaped by pulse-shaping systems that allow for specified pulse shapes and durations to be requested. Several stages of amplification are used before this beam is injected into the main amplifiers where the short-pulses are also injected. Each beam has a separate set of amplifiers, however the design for the main amplifiers is the same. In the amplifier a set of spatial filters and a deformable mirror is used to clean up the spatial profile of each pulse.

Following amplification, the long-pulse beams can be frequency tripled from 1053 nm to 351 nm central wavelength and focused into the target chamber. Additionally a distributed phase plate (DPP) can be used to produce super-gaussian focal spots with focal spot diameters from 400 to 2000 μm. Pulse durations can range from 100 ps to 10 ns. Allowed maximum energies depend on the chosen pulse duration and range from 100 J to 5 kJ.

For the short-pulse, after being amplified the beams can be sent to the upper and lower compressors where a set of tiled gratings are used to compress the pulses to user requested durations in the range of 0.7 to 100 ps. A deformable mirror is then used to correct phase-front errors before the beams are transported to the target chamber and focused by f/1.8 off-axis parabolic mirrors to maximum intensities $> 10^{20}$ W/cm^2. Delays can be placed on each beam independently to obtain a specific beam timing with and error of ± 25 ps.

OMEGA EP hosts a large suite of diagnostics including ones which can be placed into the main chamber through a set of secondary chambers known as the ten inch manipulators (TIM). Target positioners can be placed into the TIMs, however there are also a set of dedicated target positioners and target positioning optical systems that are compared to schematics made in the CAD software VisRad to accurately position the targets and lasers.

Typically for experiments involving both long pulse and short pulse beams like those in Chapter 5, shots are taken every 1.5 hours. This generally results in a total of 7 shots during a typical shot day.

3.2 Radiochromic Film

In Chapter 5 radiochromic film (RCF) is used as a proton detector in the primary diagnostic. The following will be a short summary of RCF and its usage. For a more detailed discussion see the thesis of Paul T. Campbell [106]. The particular film used was the HD-V2 film produced by Gafchromic™. This film initially appears as a thin transparent yellow plastic sheet that darkens to green due to proton or x-ray flux. The film is made up of a 97 μm polyester substrate coated with an 8 μm active layer consisting of di-acetylene monomers suspended in gelatin. Physically the sides of the film can be determined by the finish, the active layer having a matte finish and the substrate having a glossy finish. The darkening of the active layer is due to polymerization induced by radiation.

RCF is a commonly used detector in experiments with sufficient proton flux to induce changes in the active layer of the film. This is due to its high resolution and ability to provide immediate results. The downside to RCF is that it is single use, however the features on the RCF can remain for years if it is stored correctly. RCF is typically digitized using a high-quality flatbed scanner such that it can be analyzed using a set of image analysis techniques.

In experiments performed on OMEGA EP using TNSA protons, pieces of RCF are generally arranged in stacks. These stacks leverage the proton Bragg peak to generate a timeseries of data on a single shot. Due to the time of flight from the TNSA proton source foil to the interaction that is probed, each energy in the proton beam captures the dynamics of the interaction at a unique time. If only a specific proton energy could be collected on a detector then a particular time in the evolution of the interaction that is being probed could be observed. This is approximately what is done by using a stack of RCF. By carefully choosing thicknesses for metal foils to place throughout the stack of RCF, the Bragg peak for a specific energy of proton can be designed to align with the active layer of a particular piece of RCF. As a reminder, the Bragg peak is the sharp spike in the deposited energy into a material as a function of distance propagated into a material and is an inherent property of protons. The

energy deposited on each piece of RCF will be dominated by protons within a small energy range and therefore it will capture a particular time with a small error. Images are formed on the pieces of RCF through the method of proton deflectometry (see below). This method is used in Chapter 5. The method is reviewed in the following section and modifications of it are discussed in Chapter 6.

3.3   Proton Deflectometry

The standard experimental geometry to perform proton deflectometry is shown in Fig. 3.1. The diagnostic begins with a source of protons. The commonly used sources are protons generated by a D^3He implosion which produces a spherically expanding source of quasi-monoenergetic protons at 14.7 MeV [102] or TNSA protons which exist as a beam with a large energy spread [107]. These protons travel from the source to the object plane where they experience deflections by electric and magnetic fields from the interaction that is being probed. The particles then propagate ballistically along their new trajectories to the image plane where they are detected on an RCF stack as discussed in the previous section.

In the work by Kugland et al. [63], it was shown that in this setup one can relate the intensity at a position (x_0, y_0) in the object plane to the intensity at a position (x,y) in the image plane by calculating the transformation of each infinitesimally small area $dx_0 dy_0$ to the corresponding area $dxdy$. We can find this transformation by first noting that a particle which passes through the point (x_0, y_0) will experience some deflections α_x, α_y, due to the fields and will have an initial angle $\tan(x_0/l) \approx x_0/l$, $\tan(y_0/l) \approx y_0/l$ assuming protons start from a point source. The equations for the position in the image plane are then,

$$x = x_0 + \frac{L}{l}x_0 + \alpha_x L \tag{3.1}$$

$$y = y_0 + \frac{L}{l}y_0 + \alpha_y L \tag{3.2}$$
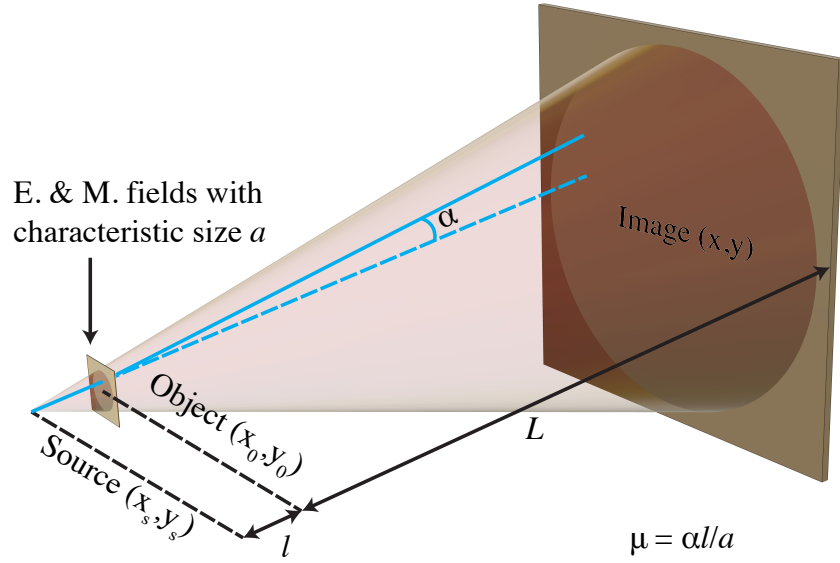
Figure 3.1: The standard point-project proton radiography experimental setup

where $\tan \alpha \approx \alpha$. This can be viewed as a coordinate transformation, therefore we can write,

$$\begin{bmatrix} dx \\ dy \end{bmatrix} = \begin{bmatrix} 1 + \frac{L}{l} + \frac{\partial \alpha_x}{\partial x} L & \frac{\partial \alpha_x}{\partial y} L \\ \frac{\partial \alpha_y}{\partial x} L & 1 + \frac{L}{l} + \frac{\partial \alpha_y}{\partial y} L \end{bmatrix} \begin{bmatrix} dx_0 \\ dy_0 \end{bmatrix}, \tag{3.3}$$

where the determinant of the transformation matrix $|\partial(x,y)/\partial(x_0,y_0)|$ is equal to the change in area due to the coordinate transformation. To transform the undisturbed proton beam in the image plane, $I_0(x_0, y_0)$, to one formed from deflected protons, $I(x, y)$, the following equation can then be used:

$$I(x,y) = \frac{I_0(x_0,y_0)}{\left| \frac{\partial(x,y)}{\partial(x_0,y_0)} \right|}. \tag{3.4}$$

If the deflections are small such that v_z, the velocity normal to the object plane, is approximately constant then deflections from magnetic fields are given by:

$$\alpha_x = \frac{\Delta p_x}{p_z} = -\frac{q}{\gamma m v_z} \int B_y \mathrm{d}z, \tag{3.5}$$

53

$$\alpha_y = \frac{\Delta p_y}{p_z} = \frac{q}{\gamma m v_z} \int B_x \mathrm{dz}. \tag{3.6}$$

These equations can also be written for deflections from electric fields:

$$\alpha_x = \frac{q}{\gamma m v_z^2} \int E_x \mathrm{dz}, \tag{3.7}$$

$$\alpha_y = \frac{q}{\gamma m v_z^2} \int E_y \mathrm{dz}. \tag{3.8}$$

From Eqn. 3.4, if I and I_0 are known, then an inverse problem is formed where the fields that caused the deflections can be solved for. The derivation for this problem is described by Kugland *et al.* where it is shown that the path-integrated fields can be solved for through a Poisson's equation. For a detailed discussion of this method and different solvers known as inversion methods that can be used, see the thesis of Paul T. Campbell [106], or the paper by Bott *et al.* [108].

In high intensity interactions where magnetic fields can have magnitudes of 1000's of T, performing quantitative analysis is not possible. One of the main assumptions of proton deflectometry analysis is that deflected particle trajectories do not cross, otherwise a unique solution cannot be found. This is quantified through the parameter $\mu = \alpha l/a$. If μ approaches or exceeds 1 for a specific probing geometry, quantitative analysis breaks down. In practice, for high intensity interactions like those in Chapter 5, proton radiographs must be analyzed qualitatively and can be compared to simulations. Additionally the method of forward scattering can be used where a guess is made for the fields in the object plane and protons are numerically propagated through these fields to form synthetic radiographs. These synthetic radiographs are then compared with experimental data and fields are revised until the data matches well.

3.4 Particle-in-Cell Simulations

Particle-in-cell (PIC) simulations are an extremely important tool used in all chapters of this thesis. Unlike hydrodynamic codes that treat the plasma as a fluid, in PIC codes the plasma is divided into a user-specified number of macroparticles. Each particle species has a specific charge to mass ratio, however the individual particles each have a unique density, position, and velocity. The simulation domain is divided into a set of cells in which the particles are able to move. The particles respond to electric and magnetic fields through the Lorentz force. The fields are affected by the distribution of particles and are solved on the grid that makes up the simulation domain.

The PIC code that is used in this thesis is the OSIRIS code [109,110], a fully relativisitic 3D3V code. To setup a simulation one must specify the size of the simulation domain, the number of grid cells in each direction, the timestep, the particle species, their density profiles, and the number of particles per cell. OSIRIS initializes the simulation domain based on these parameters, constructing the user specified density profiles by dividing the initial density for each cell into a number of macroparticles. These macroparticles can also have a specified temperature, fluid velocity, or a laser can be injected into the simulation domain such that there are dynamics when the simulation is run. Here we will summarize the main loop and function of a PIC code both classically and with QED effects. A much more extensive discussion of these ideas can be found in the thesis of Marija Vranic [111].

The simulation loop used by OSIRIS is similar to many other PIC codes and works as follows. First, the fields at the position of each particle is calculated. The fields exist on the grid and the particles exist within the cells of the grid therefore interpolation must be used to evaluate the contribution of each point on the grid at the particle position. This is done using a user specified interpolation scheme (linear, quadratic, cubic, etc.). The force from the fields on each particle can then be evaluated through the Lorentz force equation. This equation includes a time derivative and therefore must be discretized through a finite differencing scheme such that it can be solved computationally. The positions of the particles

are then updated based on this force and their previous velocity. The fields must then be updated to reflect the change in particle position. This is done by adding up the current contribution from each particle at the points on the grid. The current is then used to update the fields through the following Maxwell's equations:

$$\frac{\partial \mathbf{E}}{\partial t} = c^2 \nabla \times \mathbf{B} - \frac{\mathbf{J}}{\epsilon_0},$$ (3.9)

$$\frac{\partial \mathbf{B}}{\partial t} = -\nabla \times \mathbf{E}.$$ (3.10)

These equations must also be discretized such that they can be solved. The standard method used in OSIRIS is the Yee scheme [112]. This loop then continues until the specified number of timesteps are performed.

PIC simulations have a few considerations that must be made. The timestep must be set such that electromagnetic wave propagation is resolved such that damping or unstable growth of waves does not occur. This is defined by the Courant Fredricks Lewey (CFL) condition [113]:

$$\frac{1}{c^2 \Delta t^2} > \frac{1}{\Delta x^2} + \frac{1}{\Delta y^2} + \frac{1}{\Delta y^2}.$$ (3.11)

Additionally, all length scales must be well resolved and there must be sufficient particles to resolve the phase-space. To determine the required grid resolution and particles-per-cell (PPC), convergence testing must be performed. This is generally done by performing scans of these two quantities while looking for changes in phase-space. As the resolution and PPC are increased there will be a point above which the phase-space stays approximately the same, therefore the physical processes are well resolved. This is an important step from a computational resources perspective as PIC simulations can be very computationally intensive, therefore one cannot choose arbitrarily large PPC and resolution. One must additionally set boundary conditions for both particles and fields. The choice of boundary conditions and the way the plasma interacts with this boundary can greatly affect the physics

of the system and how accurate the results are. Finally it is important to note that collisions are not accounted for in the basic PIC loop, therefore only collisionless systems can be accurately simulated without additional computation to take collisions into account.

For the work in Chapter 6 an additional QED module in OSIRIS was used that expands the standard PIC loop as shown in Fig. 3.2. An additional term is added to the Lorentz force equation to account for radiation reaction [114]. For each particle in the simulation there is some probability that it will emit a photon of a certain energy based on the energy of the particle and the acceleration that it experiences. If a particle emits a photon then it must experience an equal and opposite force. This process is accounted for by a Monte Carlo algorithm during the particle pushing step. This calculation is performed under the Local Constant Field Approximation (LCFA), whereby equations assuming a constant field can be used given that the photon formation time is much smaller than the time and spatial variation of the fields the particle experiences [115]. Given that the photons have a large enough energy and are in strong enough fields there is also some probability that the emitted photons will generate electron positron pairs. To account for this, when a particle emits a photon that photon becomes a "real particle" in the simulation that can propagate. Prior to the current deposition step the photons in the simulation box will stochastically form pairs, which then must be accounted for as new particles. A possible error can occur if the chosen timestep is larger than the formation time of photons. A rough estimate of the correct timestep is $\Delta t < 1/a_0$ where Δt is normalized to the laser frequency.

OSIRIS can output data on several quantities such that the dynamics of the simulation can be understood. Each particle in the simulation has properties of charge density, momentum, and position. Outputting the data for all particles is possible, however for large simulations with many particles the raw data can be very large. Data such as fields, charge density, current, velocity, etc. are commonly cell averaged and output as 2D arrays. Phase space diagnostics are generally output as 2D histograms e.g. charge density as a function of position and momentum along the x-direction. Particles can also be tracked through the

Initialization

Main Loop

Read parameters from input deck:
domain size, resolution, timestep, particle species, etc.

Setup simulation domain with user specific number of cells and particles-per-cell to generate the density profiles for each particle species

Interpolate fields from the grid to the particle positions and calculate the Lorentz force

Numerically integrate equations of motion including radiation reaction:
$$\frac{d\mathbf{p}}{dt} = \mathbf{F}_L + \frac{d^2 P_\gamma}{dt\, d\chi}$$
where $\mathbf{F}_L$ is the Lorentz force and $\frac{dP_\gamma}{dt\, d\chi}$ is the recoil from photon emission calculated through a Monte Carlo algorithm. Move particles to their new positions

Generate photons and pairs

Integrate the contributions from each particle to find the current on the grid

Solve numerically:
$$\frac{\partial \mathbf{E}}{\partial t} = c^2 \nabla \times \mathbf{B} - \frac{\mathbf{J}}{\varepsilon_0}$$
$$\frac{\partial \mathbf{B}}{\partial t} = -\nabla \times \mathbf{E}$$
to update the fields on the grid

Figure 3.2: The initialization process and PIC simulation loop used by the OSIRIS QED module.

simulation domain as was done in Chapter 4. The simulation needs to be run twice: once to generate particles with tags, and a second time choosing specific particle tags to track.

Simulations are generally used in two ways: to be predictive, or to understand experiments that have already been run. In Chapter 4 simulations are used to predict what might happen in a laser-driven ion acceleration experiment with multiple ion species. If the experiment was run then the simulations could be validated and if discrepancies are found changes could be made to the simulation setup or code to better match the experiments. In Chapter 5 we use particle-in-cell simulations to understand an experiment that had already been performed. This was necessary as information that can be extracted from diagnostics was limited and did not give a complete picture of the interaction. The simulations were able to elucidate the experimental data and predicted the existence of features that could not be resolved by the diagnostic used in the experiment.

CHAPTER 4

Multiple Species Ion Shock Acceleration

In this chapter two-dimensional particle-in-cell simulations are used to explore laser-driven collisionless shock acceleration of ions in a multi-species plasma. Simple plasma slab simulations consisting of electrons, protons, and fully ionized carbon are used, varying the carbon ionization state, the relative fraction of ions, and the ratio of downstream to upstream plasma density. We find that two shocks can simultaneously propagate with different velocities defined by the dominant ion species reflected by each shock. The appearance of two shocks allows for ions to be accelerated twice, but can also cause trapping and heating of ions. We modify the current collisionless electrostatic shock theory reviewed in Chapter 2 to include a second ion fluid. This fluid model is unable to calculate the Mach number at which both ions will reflect, therefore we propose a kinetic model that may better model multi-species shocks. Scans are also performed in simulations with a laser pulse and realistic density profile that show reduced proton peak energies with the inclusion of carbon ions. Double shocks are only seen in simulations with steep density profiles, demonstrating the experimental importance of tailored density profiles. These shocks are driven along the propagation direction of the laser and are purely electrostatic, unlike the shocks that will be presented in Chapter 5 which are driven by magnetized relativistic electrons.

4.1 Introduction

As noted in Chapter 1 there is great interest in laser-driven ion acceleration for producing multi-MeV beams with small emittance and short temporal duration from plasmas. A tuneable, quasi-monoenergetic and single species beam would be a desirable source for various applications across many scientific, technological and medical fields. A beam with these properties could be used in cancer therapy [56,116], as an injector source for accelerators [117], as a picosecond resolution probe of large electromagnetic fields in high energy density physics experiments [118], as a compact and directional high energy neutron source [119, 120], to isochorically heat matter for warm dense matter experiments [121], and for isotope production for positron emission tomography [122]. Plasmas are a promising medium to provide a compact source because they can sustain huge electric fields, enabling acceleration to occur over very short distances.

Several laser-driven ion acceleration mechanisms have been identified and studied, each with unique properties that are highly dependent on both the target and laser pulse properties. The targets used are typically above the critical plasma density (overdense). Strong transfer of laser energy to the plasma electrons occurs around n_{crit}. For relativistic intensities ($I_L \lambda_L^2 > 10^{18}$ Wcm$^{-2}\mu$m^2), where the electrons oscillate in the laser fields to velocities approaching the speed of light, the modification of the effective mass of the electrons to $\langle \gamma \rangle m_e$, where $\langle \gamma \rangle$ is the time-averaged Lorentz factor, enables the propagation of the laser to the higher relativistic critical density $n_{\gamma crit} = \langle \gamma \rangle m_e \varepsilon_0 \omega_L^2 / e^2$.

The most rigorously studied acceleration mechanism is target normal sheath acceleration (TNSA) [123]. It is a robust method for accelerating ions, using relatively thick foil targets (i.e. $n_e \gg n_{crit}$) to produce beams with excellent transverse emittance properties, making it suitable for imaging applications [124]. By reducing the target thickness to sub-wavelength thicknesses, it has been theorized that quasi-monoenergetic beams can be generated by radiation pressure acceleration (RPA) or light-sail acceleration, where the whole target is accelerated together [125]. Using such targets requires excellent laser contrast and very

high-intensity laser pulses. Practically, small focal spot intensity gradients [126] or target instabilities [127] can limit RPA, although there has been recent progress in mitigating these problems [128, 129].

A promising alternative mechanism that can generate narrow energy-spread spectral features is collisionless shock acceleration (CSA) [50, 130–132]. An electrostatic shock is generated and used to reflect ions to high energies with a very small energy spread. Unlike RPA, this method does not require extreme laser pulse intensity contrast ratios, but instead requires tailored targets with density profiles that allow for the production of strong shocks while limiting the energy spread of the beam due to inherent TNSA by fields produced at the rear of the target [96]. Experiments by Haberberger *et al.* [130] and Palmer *et al.* [131] demonstrated that CSA can produce very narrow energy spread beams from the interaction of a laser with a marginally overdense hydrogen gas jet. The peak density and spatial profile of the target were found to be critical to the shock formation. In both cases CO_2 lasers were used due to their long emission wavelengths (λ_L=10 μm), reducing the target density needed to meet the critical density of the laser. In addition, Haberberger *et al.* used a train of pulses to generate a steep density gradient at the front edge of the target allowing for the production of a strong shock. This method accelerated proton beams with energies of $\sim$20 MeV and extremely narrow energy spreads $\Delta E/E_{FWHM}$ <1%.

Fiuza *et al.* subsequently derived the ideal conditions for laser-driven shock acceleration [57]. A set of 2D particle-in-cell (PIC) simulations showed that the conditions for producing a viable proton beam for proton therapy could be met with currently available lasers and realistic target density profiles. The ideal target density profile proposed in this report used a linear density ramp to a slightly overdense peak followed by an exponential density decay to suppress TNSA. The laser pulse incident on the linear ramp would isothermally heat the electrons to temperatures of $\sim$MeV and cause density steepening near the peak, thereby generating the conditions for shock formation. A scan of accelerated proton energy as a function of normalized laser intensity a_0 showed that with this ideal profile, beams with

energies >100 MeV could be produced with $a_0 \sim 10$.

Recent experiments have investigated several potential ways to produce this ideal density profile for laser systems producing pulses with a central wavelength of $\sim 1~\mu$m. At this wavelength n_{crit} is at an intermediate density between a typical gas and a solid, making density profiles with sharp gradients and near-critical peak densities difficult to achieve. Pak *et al.* [58] used a 0.5 μm thick Mylar target and a laser to ablate the back surface of the target to generate a rear scale length. Kordell *et al.* [133] used a cryogenically cooled supersonic Ar/H gas jet with a knife edge to modify the density profile of the gas jet. Hicks *et al.* [134] used a high pressure hydrogen gas jet to reach high densities, and additionally formed a blast wave using a lower power prepulse to produce a sharp density gradient on axis, similar to the work of Helle *et al.* [135]. Chen *et al.* used an extremely high pressure hydrogen gas jet [136], similar to that characterized by Sylla *et al.* [137]. These experiments were able to achieve overdense targets, but this was only achieved through the use of cooling, additional lasers, special high pressure valves and gas jets, or with a multi-species target due to the higher number of ionization states. This experimental reality is contrary to most shock theory where only a single ion species is considered. Although collisionless shock theory allows for multiple species by simply using an average ion mass and charge or by adding more terms to Poisson's equation when calculating the shock potential, these changes do not correctly incorporate the physics of an additional ion species.

Previous multiple ion species simulations have investigated intricacies that arise, such as instabilities in the upstream plasma due to the streaming of multiple species [138], in idealized low Mach number simulations below the critical Mach number [139], in specific cases to support experimental data [140], and at high laser intensities [141]. Shock formation in plasmas with multiple ion species has only been studied comprehensively for the collisional regime where collective effects drive the separation of ion species [17, 142].

To understand how the introduction of a heavy ion affects proton beam generation, here, we perform particle-in-cell (PIC) simulations consisting of three particle species (protons,

electrons, C^{6+}). This three species scenario is relevant to the use of methane (CH_4) as a gas target or CH as a solid target for laser-driven shock acceleration. In Section 2.9 collisionless shock theory was reviewed. In the following section this theory will be expanded upon to include multiple ion species. Section 4.3.1 describes the simulations we have performed for multi-species shocks using the simple plasma slab model of Fiuza *et al.*. In Section 4.3.2, we modify the laser-generated shocks demonstrated by Fiuza *et al.* to investigate whether the properties seen in the idealized plasma slab simulations are also observed in the more realistic simulations of laser-plasma interactions. At the end of Section 4.3.2 we discuss our findings and what implications these simulations have for future experiments.

4.2   Collisionless Electrostatic Shock Theory

Collisionless shock acceleration has been theorized for the last 50 years or so, with much of the theory being first derived by Sagdeev [97]. In Sagdeev's theory, basic conservation and electrostatic equations were used to describe the conditions for the formation of a soliton and for this soliton to reflect ions and become a shock. This theory was shown in Section 2.9.

Since the initial derivation by Sagdeev, this method for deriving the conditions for reflection has been used for many situations, sometimes with slight modifications. Sorasio *et al.* treated the electrons kinetically, assigning separate densities to the electrons ahead of the shock (upstream) and behind the shock (downstream) [100]. These modifications allowed for $M_{cr} > 1.6$ when the electron temperature and density are not the same in the shock upstream and downstream. The ratio of downstream to upstream electron density was given by $\Gamma = n_{e,down}/n_{e,up}$ and the temperature ratio was given by $\Theta = T_{e,down}/T_{e,up}$. This theory was later generalized by Stockem *et al.* to include relativistic effects, allowing for relativistic electron temperatures, relevant to high-intensity laser driven shocks to be considered here [101].

These theories treat the ions as a single fluid, which is integral to finding the reflection condition. As will be shown here, a single fluid treatment of the ions cannot correctly predict the structure of multi-species shocks. In Section 2.9 when solving for the Sagdeev potential of a soliton we found an ion pressure given by:

$$P_i(M, \hat{\phi}) = M^2 \left(1 - \sqrt{1 - 2\hat{\phi}/M^2}\right). \tag{4.1}$$

If we consider a multi-species plasma with two ions that make up a fraction α and $1 - \alpha$ of the ion number density respectively, the Sagdeev potential will include two terms for ion pressure with different Mach numbers,

$$P_{i,l}(M_l, \hat{\phi}) = \hat{Z}_l \alpha M_l^2 \left(1 - \sqrt{1 - 2\hat{\phi}/M_l^2}\right), \tag{4.2}$$

$$P_{i,h}(M_h, \hat{\phi}) = \hat{Z}_h (1 - \alpha) M_h^2 \left(1 - \sqrt{1 - 2\hat{\phi}/M_h^2}\right), \tag{4.3}$$

where $\hat{Z}_i = Z_i/(\alpha Z_l + (1 - \alpha)Z_h)$, and h and l represent the heavy and light ion respectively. If we follow the standard shock analysis and input the potential to reflect one of the ions, i.e. $\hat{\phi}_{max} = M_l^2/2 = u_{i,l}^2/(2Z_l k_B T_e/m_{i,l})$, then $P_{i,l} = \hat{Z}_l \alpha M_l^2$. Therefore, we can note that ion reflection corresponds to the argument of the square root going to zero, and for larger potentials the ion pressure becomes imaginary as our assumption that the ion distribution is that of a single fluid and can be described by Eqn. 2.71 becomes invalid. If we assume that the two ion species have the same upstream fluid velocities, then the ratio of Mach numbers $M_l/M_h = \sqrt{Z_h m_{i,l}/Z_l m_{i,h}}$. Following the analysis to obtain M_{cr} for each ion, one finds that it is imaginary for the heavy ion and therefore can only be solved for the higher charge to mass ratio (light) ion. This is because our fluid assumption for the light species will break down for $\hat{\phi} > M_l^2/2$, i.e. Eqn. 4.2 becomes imaginary, however reflection of the heavy species is expected to occur when $\hat{\phi} > M_h^2/2$. $M_h > M_l$, therefore the light ion pressure will be imaginary in the range of Mach numbers where the heavy ion critical Mach number is

expected to occur, invalidating the calculation of M_{cr} for this ion.

Once reflections occur, energy will be transferred from the shock to the reflected ions, thereby slowing the shock. This limits the shock velocity to be approximately given by M_{cr}. From our previous analysis we may then expect that a shock propagating through a multi-species plasma will be limited by the Mach number necessary to reflect the light ion species, therefore heavy ions will remain as a fluid background. Our simulations show this is only partially true. As expected, most of the light ions will reflect, but this leaves the shock downstream dominated by the heavy ion species. This allows for the formation of a second, slower shock that reflects the heavy ions and also interacts with the light ions that do not meet the reflection condition of the primary shock. The dynamics of this double shock will be explored in the following sections.

4.3   Simulations

4.3.1   Plasma Slab Shock Model

In the work by Fiuza *et al.* a simple simulation model of two semi-infinite plasma slabs was used to study shock formation based on the initial temperature ratio Θ and density ratio Γ between the slabs [57]. To directly build from this work, we used the same model, only modifying the ion species used. This simulation model is useful for elucidating the underlying physics because it removes the complexities of the laser-plasma interaction and a realistic density profile. Simulations were performed using the 2-dimensional OSIRIS 4.0 PIC code [143, 144]. A simulation box with dimensions $4098 \times 128(c/\omega_p)^2$ with a grid of 8196×256 cells was used. Periodic boundary conditions in the x_2 direction, perpendicular to the shock propagation, create effectively infinite plasma slabs. The simulations ran for $5000\omega_p^{-1}$ with a time step of $0.35\omega_p^{-1}$. Two ion species were used, one with the equivalent charge-to-mass ratio of a proton, and another equivalent to fully ionized carbon. Each
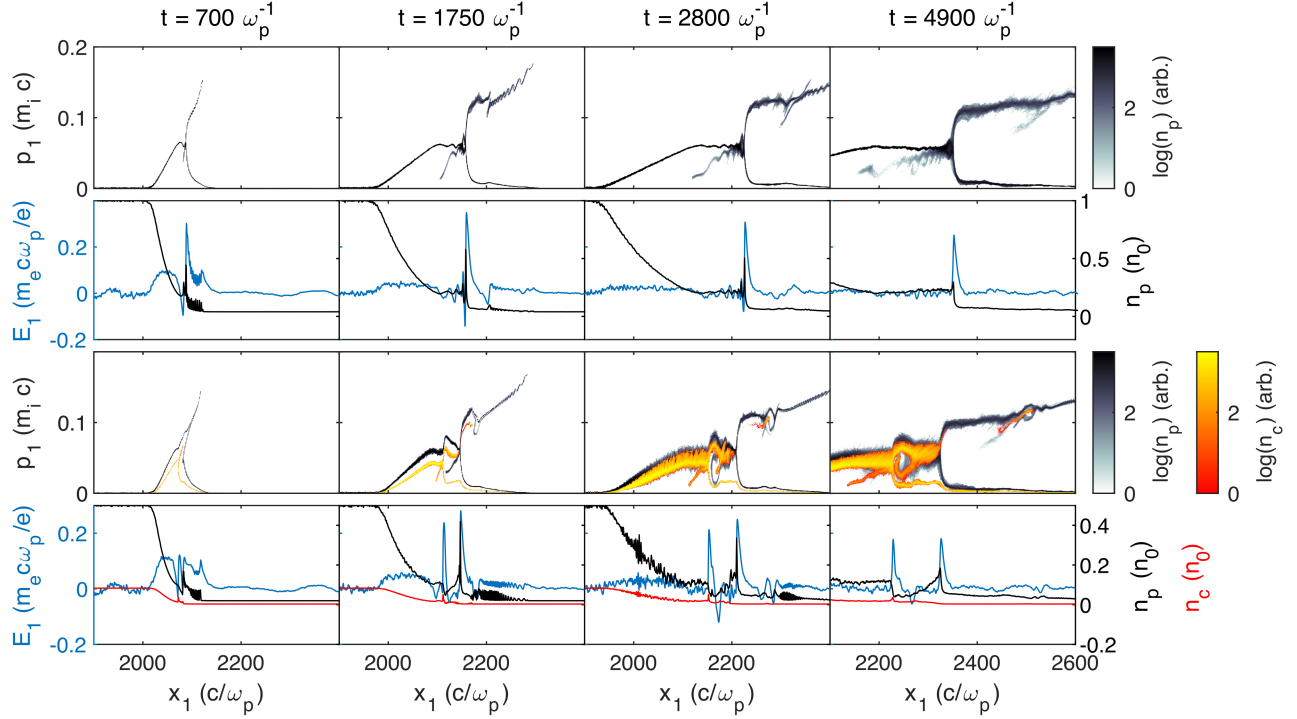
Figure 4.1: The propagation of shocks from plasma slab simulations for only protons (rows 1, 2) compared to $0.5n_e$ protons and C^{6+} (rows 3, 4). The ion phase space (rows 1, 3), and the electric field and ion densities (rows 2,4), are shown at different times as the shocks form and reflect protons or carbon ions.

particle species was initialized with 36 particles per cell. The x_1 direction was divided evenly into two plasma slabs with different densities consisting of cold ions, and electrons with a uniform temperature of 1.5 MeV ($\Theta = 1$) represented by a Maxwell-Jüttner distribution. A simulation box much larger in the shock propagation direction than the distance travelled by the reflected ions during the duration of the simulation was used to reduce acceleration due to TNSA and boundary-effects.

Fig. 4.1 shows the characteristic propagation of a multi-species shock (with an equal charge density contribution by protons and carbon ions) compared to that of a single species proton shock where the initial plasma density ratio between the downstream ($x_1 < 2048c/\omega_p$) and upstream slabs ($x_1 > 2048c/\omega_p$) $\Gamma = 25$, i.e. the single species case closely replicates the result presented in reference [57]. The $\Gamma = 25$ data is reported here because significant ion reflection occurs at this density ratio. As will be shown later, at smaller values of Γ the

shocks become weak and reflections are negligible. In both the single and multi-species cases, shocks were formed from an ion acoustic wave driven by instabilities due to the propagation of the more dense electrons of the downstream slab into the less dense upstream slab. As the electrons propagate into upstream, they generate a space-charge field that pulls the ions at the edge of the slab toward the upstream direction, this is seen in the decaying boundary between the slabs. Ions in the shock upstream that meet the reflection condition are reflected, steepening the electrostatic field. Ions that do not meet the reflection condition propagate through the shock into the downstream where they are decelerated in the frame of the shock.

In the multi-species case two shocks are formed, a feature that has not been previously observed in single species and low-Mach number multi-species simulations, but was recently reported at high laser intensities [140,141]. From the theory shown in Section 4.2, we would expect a single shock to form that only reflects protons, the higher charge-to-mass ion species. One reason this is not true is due to the change in the downstream plasma conditions of the primary shock which are effectively the upstream conditions of the secondary shock. During the formation time of the shocks, the primary shock meets the reflection condition for the protons first which slows the shock, limiting the maximum speed to be close to that given by M_{cr}. Due to the protons being initially cold, if the shock condition is met then almost all the protons will reflect. We calculated the Mach number of the primary shock from the simulations using the average upstream Z and atomic number A which were approximately 1.7 and 2.5 respectively. The velocity of the primary shock was $\sim 0.056c$ corresponding to a Mach number of ~ 1.7. Due to the larger shock potential required to reflect the carbon ions, they are only accelerated in the positive x_1 direction by the electrostatic field of the primary shock to a velocity smaller than both the primary and secondary shocks, allowing the ions to propagate into the primary shock downstream and subsequently interact with the secondary shock. This forms an upstream for the secondary shock made primarily of carbon ions that have been accelerated in the laboratory frame, corresponding to a deceleration in the frame of the secondary shock, allowing them to meet the reflection condition at lower potentials.

To calculate the Mach number of the shock we used the average upstream Z and A only including those ions with velocities smaller than the secondary shock velocity, i.e. the ions that interact with the shock. This resulted in $A \approx 8.1$ and $Z \approx 4.2$, with a shock velocity of $\sim 0.037c$ this corresponds to a Mach number of ~ 1.3. If we consider the upstream carbon ion velocity ($\sim 0.016c$) in this calculation by subtracting it from the shock velocity then this only gives a Mach number of ~ 0.7.

To better understand the reflections from the double shock, particle tracking was performed. Using the multi-species simulation shown in Fig. 4.1, particles were randomly chosen from both the carbon and proton populations with $p_1 > 0.05 m_i c$ and $x_1 > 2142 c/\omega_p$ at $t = 2450 \omega_p^{-1}$. Many of these particles followed very similar phase space trajectories, however a few characteristic phase space trajectories were identified and have been plotted in Fig. 4.2. Four general trajectories were found for the protons and are overlaid on the proton phase space and electric field in Fig. 4.2(a-b). Tracks (1) and (2) represent reflected protons that originated from the edge of the dense slab ($x_1 = 2048 c/\omega_p$) and from the low density slab respectively. Track (1) represents the highest energy protons that are transiently reflected during shock formation and can be seen in Fig. 4.1 as the cause of the break in the reflected ions in phase space. Macchi *et al.* [145] also noted this break in laser-driven shock simulations, and found that it was caused by oscillations of the electrostatic component of the shock at early times. Track (2) is representative of the steady-state reflection of the low density slab protons being reflected by the shock. Track (3) represents the trajectory of protons that originate further into the high density slab. From Fig. 4.2(b) this particle experiences smaller initial electric fields than that of track (1) resulting in a smaller initial velocity given by the inverse slope of the track. This velocity is larger than the steady-state velocity of both shocks, allowing the particle to move from the secondary shock downstream into the primary shock downstream and begin to be accelerated by the primary shock at late times. Finally, track (4) represents protons from the low density slab that did not meet the shock condition, and instead pass through the shock. These protons become trapped
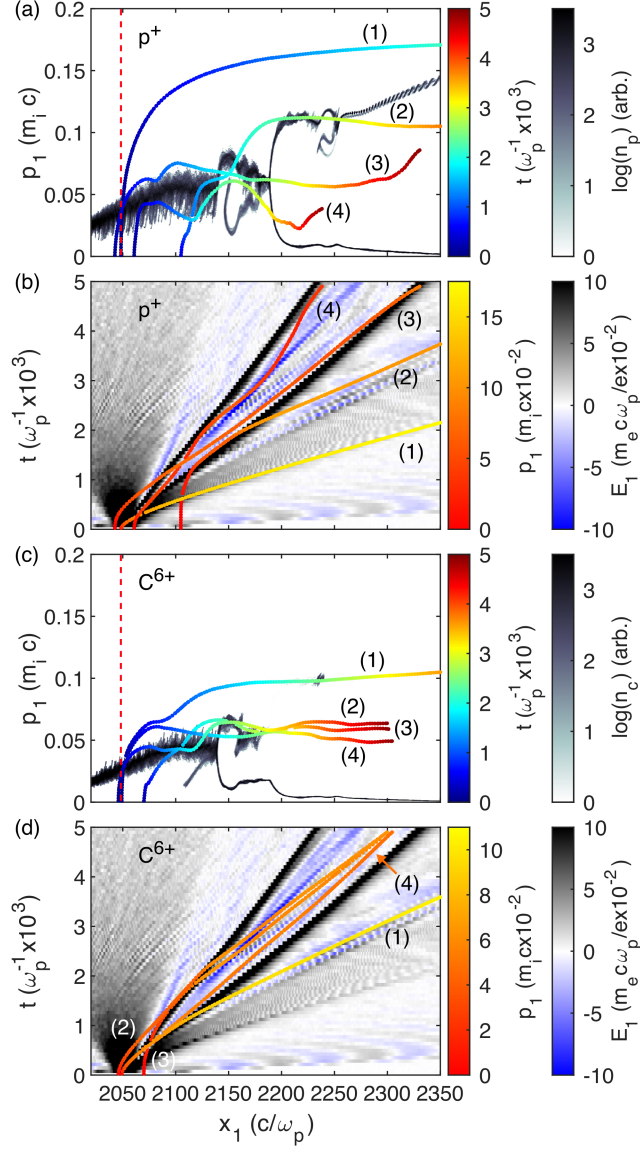
Figure 4.2: Selected characteristic trajectories of (a-b) protons and (c-d) C^{6+} overlaid on their respective phase space profiles at $t = 2450\omega_p^{-1}$ and temporal maps of E_1 where the dotted red line denotes the initial interface between the slabs with an initial density ratio $\Gamma = 25$.

between the two shocks, generating a spiral in phase space.

Very similar trajectories are seen for the carbon ions in Fig. 4.2(c-d). The exception is for track (1), that shows two stages of acceleration where it is reflected by the trailing secondary shock and then further accelerated by the primary shock. This only occurs very early in the shock formation when carbon ions reflected from the secondary shock can propagate just ahead of the primary shock to gain energy from the electrostatic fields. It should be noted that the secondary acceleration the carbon ion experiences at the primary shock is not a reflection. At intermediate times, in Fig. 4.1 we can see that carbon ions reflected from the secondary shock are accelerated to velocities too small to pass through the primary shock and are instead decelerated by the oscillatory fields and trapped between the shocks. These oscillatory fields are observed between the shocks in Fig. 4.2(d), increasing the slope of the ion trajectories, corresponding to deceleration of the ions. At late times, when the primary shock slows and the electrostatic fields weaken, we can see that some carbon ions begin to pass the primary shock.

To further study the characteristics of these multi-species shocks, we varied the ratio of densities Γ, the ratio of protons to carbon ions, and the charge-to-mass ratio of the carbon ions. The results of the simulations scanning Γ are shown in Fig. 4.3. A similar study by Fiuza $et\ al.$ for a purely proton shock found that for $\Gamma \approx 2$ an ion acoustic wave is driven as the high density slab expands into the low density slab, but ion reflection does not occur until larger density ratios of $\Gamma \geq 4$ [57]. When the charge density consists of equal parts protons and C^{6+}, we observe slightly different results. In the case of $\Gamma = 2$, protons are accelerated and trapped due to the buildup of carbon ions. By $\Gamma = 3$, the acceleration and trapping of C^{6+} begins a few oscillations behind the leading edge of the ion acoustic wave and protons are seen to reflect. For increasing Γ, the Mach number of both the primary and secondary shocks are increased, enabling significant ion reflection. When $\Gamma = 100$, the C^{6+} trapping becomes low enough such that these ions can interact with the primary shock, allowing them to be boosted to even higher energies. This results in three co-propagating
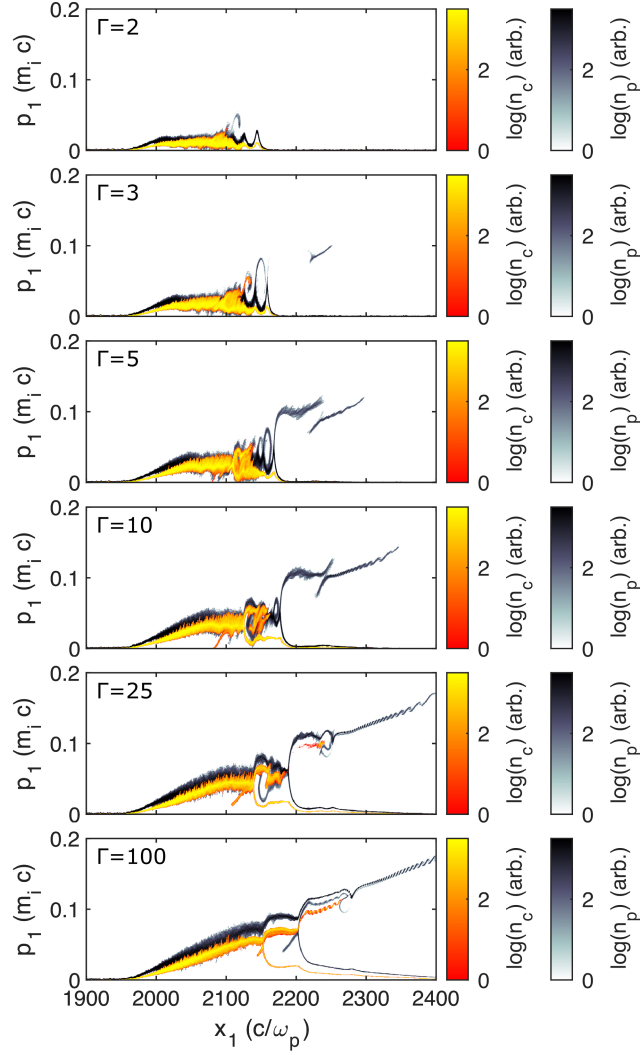
Figure 4.3: Plasma slab proton and ion momentum evolution at $t = 2450\omega_p^{-1}$ using various Γ with an initial $T_e = 1.5$ MeV and $n_p = 0.5n_e$.
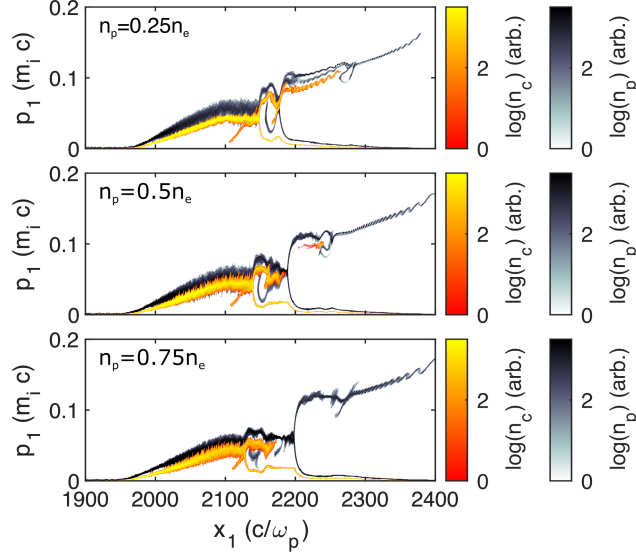
Figure 4.4: Plasma slab proton and ion momentum evolution at $t = 2450\ \omega_p^{-1}$ using a $\Gamma = 25$ with an initial $T_e = 1.5$ MeV and n_p is varied as shown in the plot.

bunches of ions with slightly different energies. For the carbon ions to meet this boosting condition the velocity of the reflected ions must exceed the shock velocity of the primary shock. The boosted protons are not reflected, instead seeing a double boost as they move from the secondary shock downstream into the primary shock upstream. In Fig. 4.4 it can be seen that by reducing the number of protons and increasing the number of carbon ions to maintain the initial neutrality, the necessary Γ to meet the boosting condition is reduced. This is due to the secondary shock velocity increasing, while the primary shock velocity decreases.

The effect on the shock structure by varying the ionization state of carbon (i.e. the charge-to-mass ratio) is shown in Fig. 4.5. Plotting the measured velocities for the measured parameter space (Fig. 4.6(a)), it is found in the high-Mach number limit (large Γ), the ratio of shock velocities approximately scales as $\sqrt{A_C/Z_C}$ where A_C is the atomic number of carbon and Z_C is the ionization state. The scan includes the fictional ionization state of C^{10+} to extend the trend. Plotting the velocity of the shocks as a function of Γ for C^{6+} (Fig. 4.6(b)) and fitting to the ratio of the primary to secondary shock velocities gives
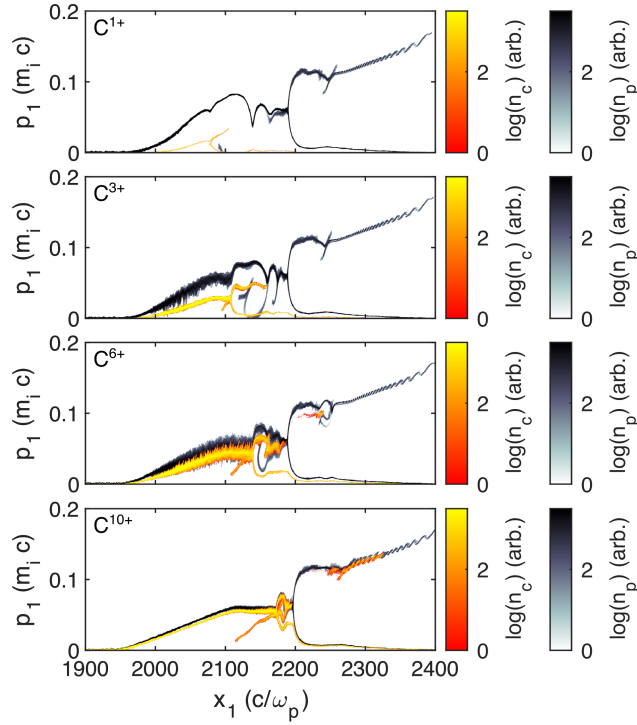
Figure 4.5: Plasma slab proton and ion momentum evolution at $t = 2450\ \omega_{\mathrm{p}}^{-1}$ using a $\Gamma = 25$ with an initial $T_e = 1.5$ MeV and $n_p = 0.5 n_e$. The ionization state of the carbon ion is varied while the charge density is held constant. Note the fictional C^{10+} ionization state is included to observe the trend.

$u_{sh,1}/u_{sh,2} \propto 1/(a\Gamma + b) + \sqrt{2}$ where $a \approx 0.4$ and $b \approx 0.88$. We can also note from Fig. 4.4 that changing the fraction of ion species will also change the ratio of shock velocities.

In deciding how to model these trends we made a few important considerations. Firstly, the initial conditions outlined in the simulations e.g. density ratios Γ and ion fluid velocities evolve to a set of steady-state conditions which can be greatly different from the initial conditions. This is a problem because the current models define the shock properties at steady-state, therefore we would need to also model the evolution of these properties. Although Γ is defined for the electrons, from Fig. 4.1 rows 2 and 4 we can see how the density ratio decays for the ions from an initially large ratio to a much smaller ratio at the shock steady-state. This steady-state ratio Γ_{ss} is shown for the primary and secondary shocks in Fig. 4.6(c) which shows that although the density ratios start at very different values, they decay to very similar ratios. Secondly, ion fluid velocities in the shock upstreams differ from the initial values due to acceleration by electric fields formed by reflected ions and for the secondary shock upstream, acceleration by the primary shock. The acceleration by the primary shock can greatly affect the fluid velocity of the ions in the secondary shock upstream as demonstrated by Fig. 4.5. Thirdly, the double shock structure is made of many populations of ions e.g. reflected and trapped which require a kinetic description. Finally, we must note that although we are simply changing the charge of the carbon ions in Fig. 4.5, the number density of these ions will also change to maintain the charge density.

Although a rigorous model will need to treat the ions kinetically as we will later discuss, as a first attempt we made approximations to model the ions as two fluids and the shocks as being independent. For the purpose of our simple model we assumed that the primary shock was made of two ion species, reflecting only the light ion species, and the secondary shock was a single species shock only including the heavy ion species. The primary shock was modeled using the relativistic electron pressures derived by Stockem *et al.* [101],

$$P_{e,up}^r(\hat{\phi}, \Gamma_{ss}) = \frac{\hat{\phi}(1 - \mu_0)}{1 + \Gamma_{ss}},\tag{4.4}$$
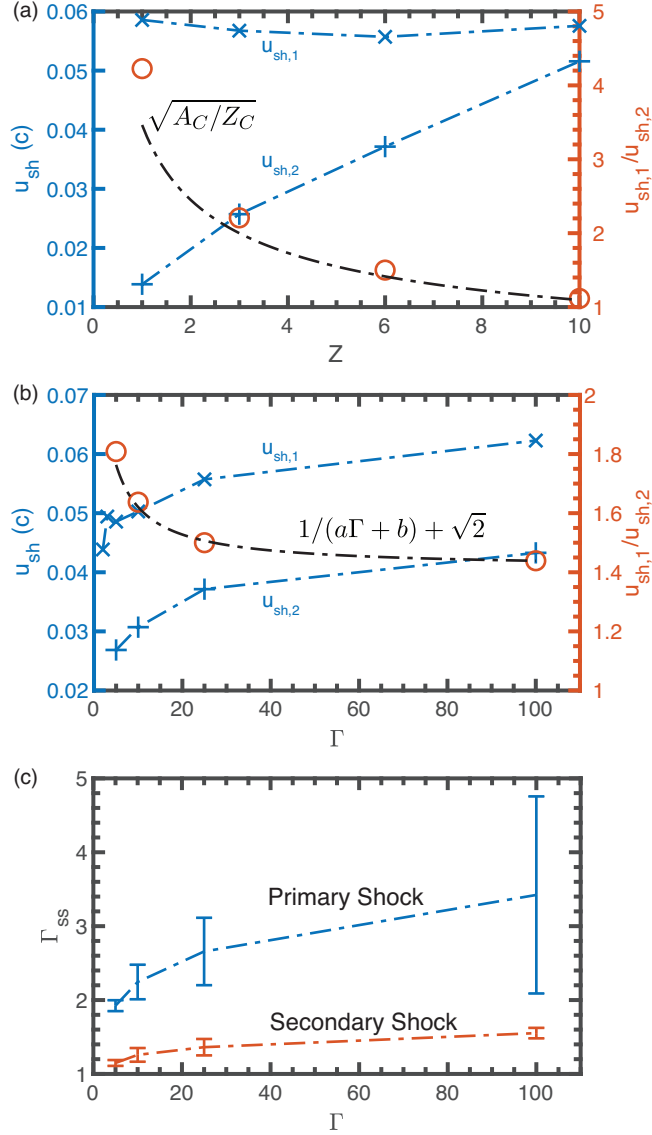
Figure 4.6: Velocities in the lab-frame of the primary (reflects p^+) and secondary (reflects C^{Z+}) shocks generated from semi-infinite slabs with a uniform electron temperature of 1.5 MeV and various (a) charge-to-mass ratios from figure 4.5 and (b) density ratios Γ from figure 4.3. The ratio of velocities as a function of Γ is approximately given by $1/(a\Gamma+b)+\sqrt{2}$ where $a \approx 0.4$ and $b \approx 0.88$. The steady-state ratio of electron densities across the shocks Γ_{ss} differs from the initial ratio Γ shown in (c) at $t = 2450 \, \omega_p^{-1}$.

$$P^r_{e,down}(\hat{\phi}, \Gamma_{ss}, \Theta) = \frac{\hat{\phi}\Gamma_{ss}}{\Theta(1+\Gamma_{ss})}\left[\hat{\phi}\left(1 - \frac{\mu_0}{\Theta}\right) + \Theta\left(1 + \frac{\mu_0}{\Theta}\right)\right], \tag{4.5}$$

where $P_{e,up}$ and $P_{e,down}$ are the upstream and downstream electron pressures in the relativistic limit where $\mu_0 = m_e c^2/k_B T_e \ll 1$ is the normalized upstream electron temperature, and Θ is the ratio of downstream to upstream electron temperatures. The Sagdeev potential can then be constructed from these electron pressures and the multi-species ion pressures we derived in Eqn. 4.2 and 4.3. To solve for the Mach number to reflect the light ion species we set $\hat{\phi} = M_l^2/2$ and $\partial\hat{\phi}/\partial\chi = 0$ in Eqn. 2.75. Solving for M_l gives the critical Mach number $M_{cr,l}$,

$$M_{cr,l} = \sqrt{2\Theta\left[\frac{2\zeta - 1 + \mu_0}{\Gamma_{ss}(1 - \mu_0/\Theta)} + \frac{2\zeta - 1 - \mu_0/\Theta}{1 - \mu_0/\Theta}\right]}, \tag{4.6}$$

$$\zeta = \hat{Z}_l\alpha + \frac{Z_l A_h}{Z_h A_l}\hat{Z}_h(1-\alpha)\left(1 - \sqrt{1 - \frac{Z_h A_l}{Z_l A_h}}\right). \tag{4.7}$$

In the case of a single species ($\alpha = 1$, $\zeta = 1$) these equations simplify to equation 12 in the report by Stockem *et al.* [101]. We used this single species equation to calculate the velocity of the secondary shock assuming a heavy ion only plasma. To obtain the ratio of the primary shock velocity to the secondary shock velocity we assume that the shocks will move at the velocity needed to reflect the light and heavy ions respectively at steady state i.e. $u_{sh,1} = \sqrt{Z_l k_B T_e/m_{i,l}}M_{cr,l}$ and $u_{sh,2} = \sqrt{Z_h k_B T_e/m_{i,h}}M_{cr,h}$. We must also take into account the fluid velocity of the heavy ions in the upstream of the secondary shock because M_{cr} is calculated in the frame where the upstream ions are stationary. Using conservation of energy and noting that $\hat{\phi} = M_l^2/2$ gives the velocity of the heavy ions in the laboratory frame as,

$$u_{0,h} = u_{sh,1}\left[1 - \sqrt{1 - \frac{Z_h A_l}{Z_l A_h}}\right]. \tag{4.8}$$

This velocity is due to the acceleration of the heavy ions as they pass through the electrostatic fields of the primary shock without being reflected. We can then calculate the ratio of shock

velocities as:

$$\frac{u_{sh,1}}{u_{sh,2} + u_{0,h}} = \frac{1}{1 + u_{sh,2}/u_{sh,1} - \sqrt{1 - Z_h A_l/Z_l A_h}}. \tag{4.9}$$

To plot these equations we used Γ_{ss} calculated from the average of electron densities on either side of both shocks as shown in Fig. 4.6(c). This value varies for changes in both the initial Γ and the choice of carbon charge state Z. The ratio of electron temperatures across the shocks Θ can differ from unity and can be different for both shocks, but we found the temperature to be similar to the initial isothermal conditions in this case. Fig. 4.7 shows the values calculated from equation 4.6 for the primary and secondary shock velocities compared to the values extracted from the simulations. For changing Γ and Z, the theory predicts similar values to the simulations for $u_{sh,1}$, although the trends are not correctly modeled. This discrepancy may be due to many of the properties not captured by the model e.g. reflections, upstream ion drift velocity, etc. which could have a small effect on the shock velocity. The theory overestimates the secondary shock velocity by a factor of 2-3 in both the Γ and Z scans, although it predicts a similar trend for the Z scan. The simulations show that the secondary shock velocity should be closer to the primary shock velocity, suggesting that protons cannot be neglected in the secondary shock.

In a rigorous model of the secondary shock, the protons should be included in two populations: protons that freely drift from the shock downstream to upstream, and trapped protons in the shock upstream. This kinetic treatment could build from the model for a single species including reflections proposed by Malkov *et al.* [99]. In this kinetic model one also needs to consider the electron distributions on either side of the shock. In the model of Stockem *et al.* used here, the downstream of both shocks is assumed to be made of two population of electrons: trapped and free. The trapped electrons are assumed to follow the maximum density trapping approximation [146]. This approximation may not be true between the shocks. In our simple analysis the shocks were taken to be independent, therefore the upstream electron distribution of the secondary shock was taken to be a Maxwell-Jüttner distribution. These shock are coupled, therefore the upstream distribution of the secondary
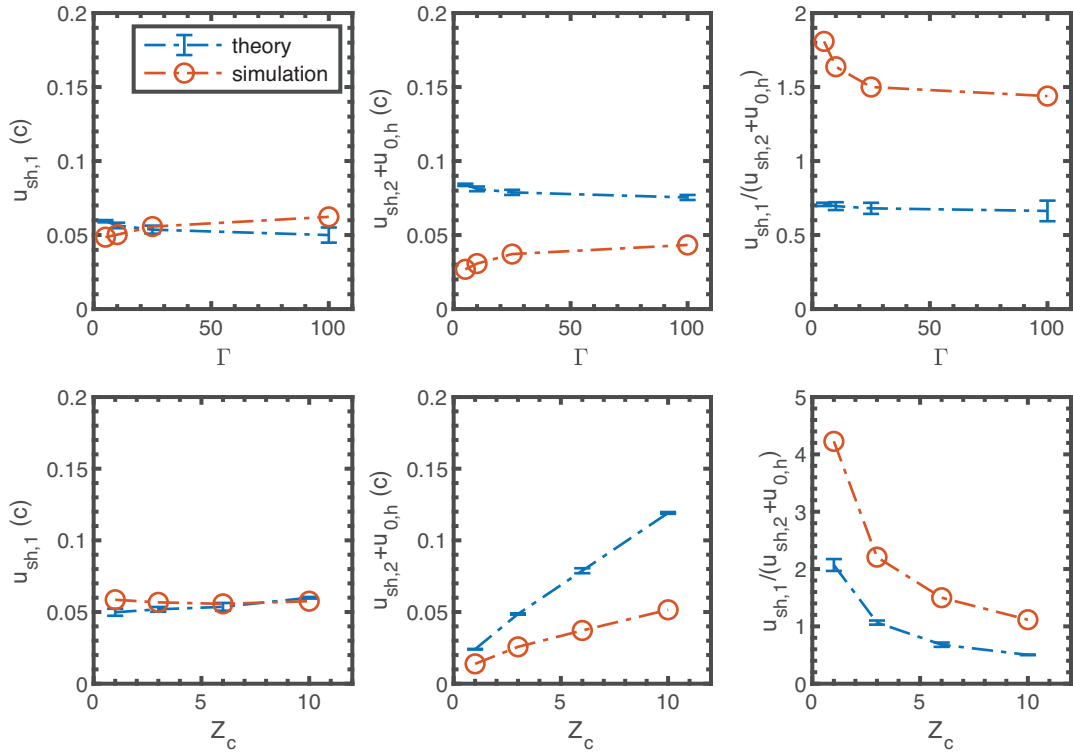
Figure 4.7: Comparison of simulated shock velocities with those calculated from Eqn. 4.6 and 4.9 using Γ_{ss} from the simulations. The top row is for varying Γ and the bottom row is for varying Z_c.

shock should match that of the primary shock downstream. A kinetic model would be very useful in accurately estimating reflected ion energies which cannot be done with the simple model presented here.

4.3.2   Laser-Driven Shock

In order to connect the conclusions from the slab simulations to laboratory experiments, we explored laser-driven shocks by adapting the ideal profile described by Fiuza *et al.* to include multiple ion species. These simulations were performed in 2D with a $3840 \times 240(c/\omega_0)^2$ simulation box and a grid of 12288×768 cells. A laser pulse with infinite spot size and a normalized intensity $a_0 = 2.5$ was injected to propagate along the x_1-direction of the simulation box, linearly polarized in the x_2-direction. The rise and fall time of the laser pulse was $2473.9\omega_0^{-1}$, equivalent to a 1 ps full-width half-max pulse duration for a 1 μm wavelength laser. The laser was incident on a density profile consisting of $2.5n_{crit}$ electrons and a combination of protons and C^{6+} with a cumulative charge density equal to that of the electrons. Each species was initialized with 36 particles per cell. The density profile used a linear increase over $10\lambda_0$ followed by an exponential decrease with a characteristic decay length of $20\lambda_0$ where λ_0 is the wavelength of the laser [57].

Just as in the case of the plasma slab, we compared the single species shock formation with that of the multi-species shocks as shown in Fig. 4.8. The laser pulse incident on the rising edge of the density profile accelerates electrons into the plasma which drives a return current. The return current is then accelerated by the laser, allowing for a larger region of electrons to be heated. The electrons in a small region near to where the shock is formed will have a more uniform temperature, however it should be noted that laser accelerated electrons will not have a Maxwellian distribution; instead, a high-energy tail will be generated. The overdense target and a high-intensity laser pulse allow for density steepening to occur near the peak of the profile and a shock to form. In both cases, a single shock is formed near the density peak that propagates, only reflecting protons. Electron heating in the single-
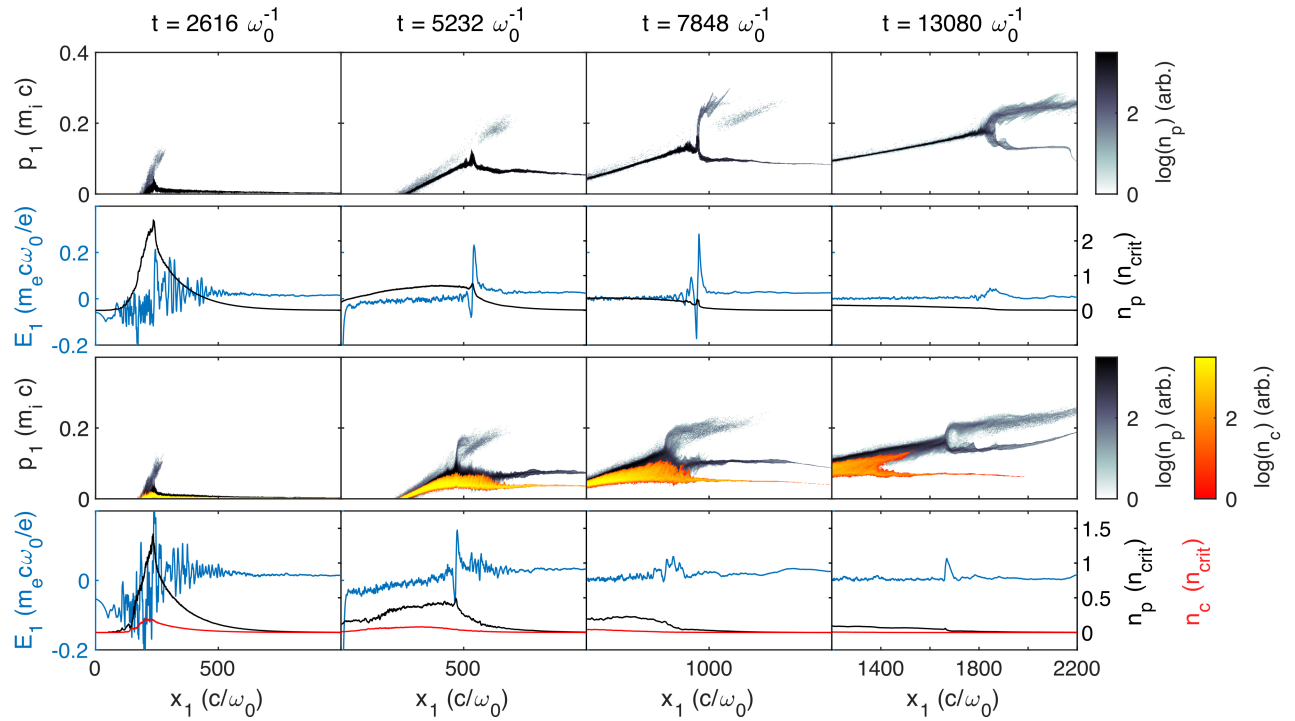
Figure 4.8: Propagation of a laser-driven single ion species shock (rows 1 and 2) and multi-species plasma shock (rows 3 and 4). The proton and ion phase space (rows 1, 3), and the electric field and proton and ion densities (rows 2,4), are shown at different times as the shocks form and reflect protons or ions.

species and multi-species simulations was compared by looking at the electron phase space (p1 vs. x1). The phase spaces were very similar at all times, giving comparable electron temperatures of ∼0.9 MeV at t = $7848\omega_0^{-1}$ in the shock upstreams of the single and multi-species simulations, suggesting that heating is similar in both cases. We performed several simulations with different ion ratio compositions, but in all cases only a single shock was formed (Fig. 4.9). This is inconsistent with the results found with the semi-infinite plasma slabs. Although at late times the multi-species phase space appears to show reflected carbon ions, the acceleration of these carbon ions occurred in the shock upstream due to streaming instabilities [138], and near the shock as the ions cross the electrostatic potential without being reflected. A notable result was found at extremely low fractions of protons ($0.01n_{crit}$) where protons are initially reflected, and later, due to a decrease in proton density, a carbon shock is able to form. Therefore, the laser energy is sufficient to drive a single shock in either ion species.

The generation of only a single shock suggests that the plasma is not driven strongly enough to generate a double shock, or the shock formation mechanism is different from the simple slab model. One difference is seen in the way that the electrons are initially driven. Compared to the slab case where the electrons are initially isothermal, here the laser will impart a drift velocity into the electrons and ions which travel into the cold upstream. The drift velocity is given by the hole boring velocity [147]:

$$v_{HB} = c\sqrt{\frac{Z}{2A}\frac{m_e}{m_p}\frac{n_{cr}}{n_e}a_0^2}, \tag{4.10}$$

that is derived assuming perfect laser reflection and therefore overestimates the drift velocity in this case. Using the average Z/A for the $n_p = 1.25n_{crit}$ simulation, and a steepened electron density of $5n_{crit}$, near the peak of the density profile $v_{HB} = 0.015c$. This is much smaller than the steady-state shock velocity of $\sim 0.12c$. The upstream electron temperature varies during shock propagation, but on average $T_e \approx 1.5$ MeV. Using these values and the average
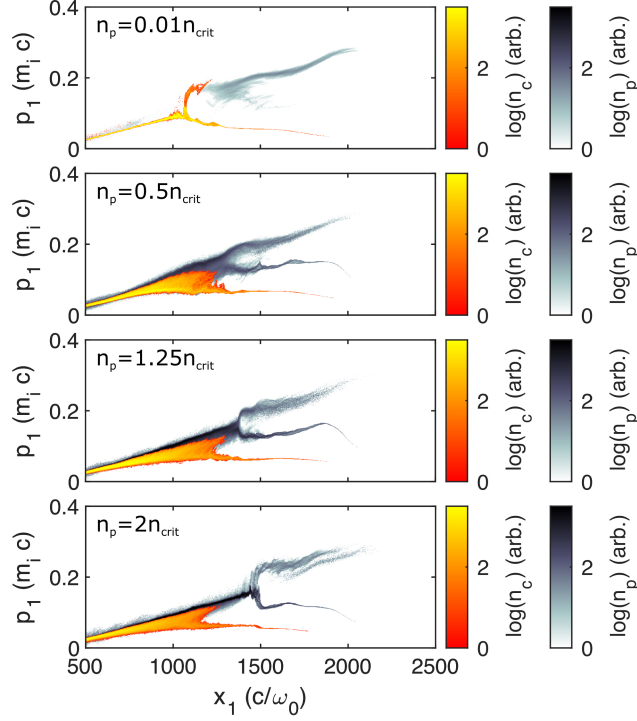
Figure 4.9: Comparison of multi-species laser driven shocks using the ideal density profile and a cumulative ion charge density of $2.5n_{crit}$ at $t = 11366c/\omega_0$.

Z and A during steady state propagation gives a Mach number of ~ 1.4 for the multi-species shock in figure 4.8 rows 3 and 4 where we have subtracted the upstream proton drift velocity of $0.07c$. Steady-state proton reflection occurs at approximately the same time $(4360\omega_0^{-1})$ that the electrons become isothermal near the shock. Stockem *et al.* [51] found that the ratio of the drift to fluid velocity defines the shock formation mechanism, and therefore the shock formation time. For both the slab and laser-driven shocks the temperatures and fluid velocities should cause the formation mechanism to be purely electrostatic. The hole boring velocity is also much smaller than the shock velocity, therefore the shock is not simply being pushed by radiation pressure. This suggests that the dominant driving mechanism could be the density steepening that occurs as the laser propagates toward the peak of the density profile, consistent with the work of Zhang *et al.* [148].

To further investigate this discrepancy, the density profile (Fig. 4.10 row 1) was split into
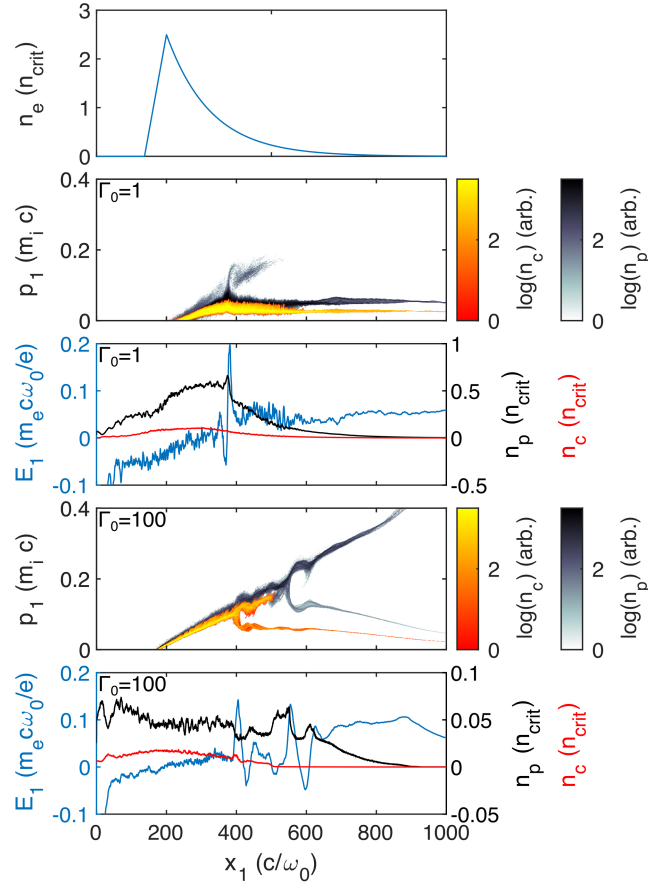
Figure 4.10: Comparison of laser driven shocks at $t = 4360c/\omega_0$ using a modification of the initial ideal density profile shown in row 1 where Γ_0 is the initial ratio between the peaks of the density up-ramp and decay.

two parts: the linear increase and exponential decay. The overall density of the exponential decay was divided by an integer Γ_0 creating a density ratio between the two parts of the profile, analogous to large density steepening near the peak. This density ratio is not perfectly equivalent to the Γ in the plasma slab case, because further density steeping can occur in the laser driven case. As the laser interacts with the rising edge of the plasma it heats the electrons allowing a double shock to form (Fig. 4.10) at the interface between the two regions of the density profile just as in the slab simulations. The double shock forms prior to the laser reaching the peak density, instead forming as a result of the charge separation at this interface. This suggests that the formation of a double shock is allowed by the separation of ion species which does not occur in the laser driven case using the ideal density profile (Fig. 4.10 row 1) because the ions are driven together at the hole boring velocity and upstream electric fields are suppressed by the exponential decay of the density profile. Double shocks may therefore be more prevalent in targets with sharp interfaces where strong electric fields and ion separation can occur. Consistent with our results, a recent report by Kumar *et al.* looked at larger laser intensities and showed that double shocks only form for $a_0 > 10$ using a density profile similar to that shown in figure 10 row 1 [141].

For the slab and laser driven cases we calculated the reflected proton energy spectra (Fig. 4.11). In this case we have only shown the reflected protons from both the primary and secondary shocks to study the change in ion energy, but one should note that in experiment these spectra would also include the TNSA ions and those in the secondary shock downstream. In the case of the plasma slabs (Fig. 4.11(a) and (b)) the spectra show that the maximum proton energy increases with larger Γ, and a larger initial fraction of protons as expected from the momentum plots. For $\Gamma \geq 5$ we see the formation of two populations of protons, a high energy population due to reflections from the primary shock, and a lower energy population due to reflection and trapping between the secondary and primary shocks. At $\Gamma = 100$ the high energy population ($E > 6$ MeV) is seen to be multi-peaked due to instabilities and the addition of a proton bunch boosted from the primary shock downstream. The
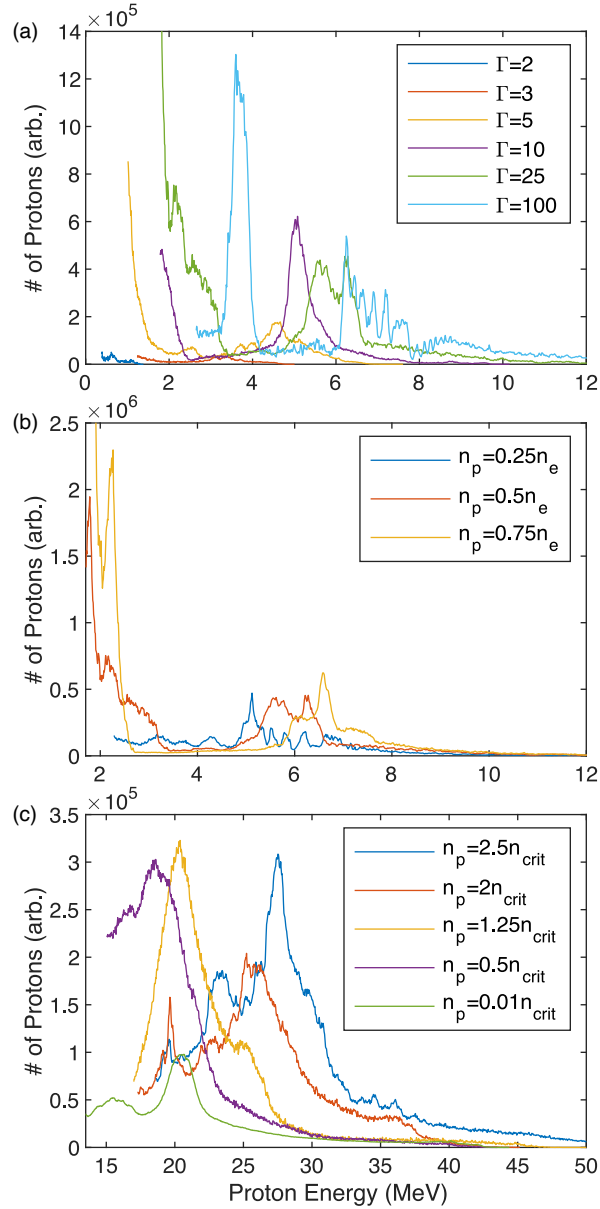
Figure 4.11: A comparison of reflected proton energies from (a-b) slab shocks ($t = 2450\omega_{\mathrm{p}}^{-1}$), varying Γ (Fig. 4.3) and the ion fraction (Fig. 4.4) and (c) laser driven shocks ($t = 13080\omega_0^{-1}$), varying the ion fraction (Fig. 4.9)

lower energy bunch has an energy of ~3.6 MeV with a full-width half-maximum (FWHM) energy spread $\Delta E/E \approx 12\%$. This is much smaller than the low energy populations seen at all other Γ. From Fig. 4.3 this is seen to be as a result of the reduced trapping between the shocks in the $\Gamma = 100$ case.

Similar to the plasma slab case, as the fraction of protons is decreased the peak proton energy also decreases. In the purely proton simulation ($n_p = 2.5n_{crit}$) a proton bunch is formed at ~27.5 MeV with $\Delta E/E \approx 16\%$. The proton peak energy decreases with approximate values of 25, 20, and 18.6 MeV for proton densities of 2, 1.25, and $0.5n_{crit}$ respectively. In the anomalous case of an extremely low proton density ($n_p = 0.01n_{crit}$) an ~20.6 MeV bunch with a energy spread of $\sim 14\%$ is formed, giving it a similar energy to the $n_p = 1.25n_{crit}$ case.

To translate these results to experiments the effects of the many simplifications we have made should be understood. Although these are 2D simulations, by using periodic boundaries and infinite focal spots we have neglected effects due to the realistic focusing of a laser. In near-critical plasmas instabilities such as hosing and filamentation are expected which may greatly affect the shock front as seen in the results of Puyuelo-Valdes *et al.* [149]. The significant density steepening in our simulations may only exist in a small region near the focal spot and could potentially be broken up due to filamentation. In the realistic density profile of a gas jet, transverse density gradients will exist which may also affect laser focusing and the directionality of the shock. As noted by Fiuza *et al.* in 3D, TNSA field amplitudes will be smaller, therefore energy spreading by TNSA will be reduced [57]. In the context of multi-species plasmas this may result in reduced separation of ion species and therefore the suppression of multiple shocks. In our work we included a second ion species and scanned the ionization state in the plasma slab simulations, therefore we know that shock velocities depend on the ion charge-to-mass ratio, and ions with similar charge-to-mass ratios will form double shocks that propagate at similar speeds. From these results it is unclear how shocks will form in experiments where several ionization states exist at the time of shock formation,

although it is likely that at least a single shock will form due to the ion with the largest charge-to-mass ratio. These results are then most applicable to experiments where only two ions exist at the time of shock formation.

If only two ions exist in the plasma then we can use our results to make a couple experimentally important statements. Firstly, density steepening is important to the generation of strong shocks that can reflect protons to high energies. The slab shock simulations showed that the highest proton energies were reached at large density ratios between the upstream and downstream even with the appearance of a secondary shock. In fact, as seen in the slab simulations the secondary shock may aid in accelerating more protons by boosting them in the primary shock downstream to a velocity large enough that they can be accelerated by the primary shock. Density steepening will depend on the initial density profile of the target and the laser intensity [148]. Secondly, the target composition greatly impacts the maximum energy reached by the protons. In both the slab and laser generated shock simulations, as the secondary ion fraction increased, the peak proton energy decreased. In experiment, an optimal target composition may exist where the fraction of the secondary ion is large enough to create an overdense plasma, but small enough that it does not significantly impact the energy of accelerated protons. Several target density profiles and compositions should be tested to find the optimal conditions.

4.4   Conclusion

The numerical modeling presented here demonstrates that for large Mach numbers, in excess of the critical Mach number where reflections are significant, having multiple ion species within the plasma means complex effects like double shocks and multiple stages of acceleration can occur. We showed these effects cannot be described by the standard method of shock analysis where ions are treated as a single fluid. Using a semi-infinite plasma slab model, we built on the work of Fiuza *et al.* [57], expanding the parameter space to include a

second ion species. Several simulations were performed varying the ratio of densities between the slabs, the fraction of densities of the two ion species, and the charge-to-mass ratio of the second ion. These simulations showed that the ratio of the velocities of the shocks is approximately given by the square root of the inverse charge-to-mass ratio of the heavy ion. Using the relativistic model of Stockem *et al.*, we derived a simple model that allowed us to calculate the velocities of the two shocks. This model was able to predict the primary shock velocity quite accurately. The secondary shock model neglected important physics and was therefore inaccurate, differing from the simulated velocity by a factor of 2-3. A kinetic model including all populations of trapped and reflected ions is necessary. One promising basis for this model is that of Malkov *et al.* where ions are treated kinetically [99].

To connect these slab-driven shocks to laboratory experiments we performed simulations using the laser-driven shock conditions derived by Fiuza *et al.* [57]. These simulations showed only single shock formation, reflecting the light ion species, contradictory to the double shocks found in the slab simulations. To reconcile this discrepancy we modified the density profile to include a steep drop in density after the peak, effectively increasing the density steepening and therefore the shock strength. This showed the formation of a double shock, but this shock was generated prior to the laser reaching the peak density, suggesting that it is the separation of ion species that leads to double shock formation. In the context of experiments, this means that the density profile and ion species are very important to the number and strength of shocks formed. In gas jet targets where density transitions are smooth, density steepening will depend on the laser parameters and therefore only a single shock may form, reflecting the light ion species. In ablated solid targets like those used by Pak *et al.* [58], double shocks may be driven due to the sharp density change at the back-surface of the target.

The make up of the density profiles is also very important to the velocity of the reflected ion species. By scanning the ratio of ions we found that an increased fraction of heavy ion species will decrease the shock velocity and therefore the energy of the reflected protons. If

one is optimizing for the maximum proton energy, there is likely an optimal target composition to be found that includes enough of a secondary ion species to create a dense enough target to drive a strong shock, but not too much of that species such that it decreases the shock velocity.

When considering the addition of a second, or multiple ion species there are still many areas that need to be investigated both theoretically and experimentally. Our analysis ignored ionization effects which may be important to the formation of shocks if the plasma cannot reach a state of uniform ionization prior to shock formation. Multiple ion species may also affect instability formation rates, and therefore the shock formation time. In laser-driven shocks, as also noted by Pak *et al.*, one may be able to tailor density profiles to achieve a required ion beam [58]. In multi-species shocks, the idea of what the "ideal profile" is may differ from single species as the fraction of ion species can be varied and one may want to suppress the formation of a second shock. In experiment, the composition of the target may act as a tuning parameter, potentially allowing for the discovery of beneficial processes such as multiple stages of acceleration, or at low proton densities, the acceleration of narrow energy spread proton beams as we have shown.

CHAPTER 5

Semi-Relativistic Magnetized Shock Formation in the Laboratory

In this chapter, an experiment studying strongly magnetized quasi-perpendicular collisionless shocks driven by relativistic electrons using proton deflectometry is presented. The shock forms as energetic electrons and the associated strong magnetic field generated by a short-pulse laser interaction impinges on a cooler plasma produced by a long-pulse laser. PIC simulations reveal that this relativistic-electron-driven shock forms at an interface that is unstable to shear and streaming instabilities. The shocks considered here are multispecies as was discussed in the previous chapter, however only a single ion species is simulated as the simulations are already computationally intensive with a single ion species. The shocks driven in Chapter 4 were purely electrostatic and traveled parallel to the laser propagation direction, however in this chapter the shock downstream is magnetized and forms > 1 mm from the laser focal spot. Most notably, the shocks here are semi-relativistic in two ways: firstly, they are driven by a flow of electrons with a fluid velocity of $\sim 0.5c$, secondly, they are so strongly magnetized that the magnetic energy per electron $> m_e c^2$ and the Alfvén speed exceeds $0.7c$ along the interface.

5.1 Introduction

As noted in Chapter 1 and shown in the previous chapter, high power lasers are a useful tool for driving shocks in high-energy-density conditions with a broad range of applications, including ion beam acceleration [16,50], compression of materials [150], and laboratory studies of the underlying mechanisms governing astrophysical shock formation and particle acceleration [35,69,77,151]. To date, experiments motivated by astrophysical shocks have primarily focused on the non-relativistic regime. Charged particle and optical diagnostics can probe the densities, temperatures, and electromagnetic fields around the shocks. For example, Fiuza *et al.* used high-power lasers to study particle energization in conditions relevant to the shocks formed between young supernova remnants and the interstellar medium [35].

In the highest energy astrophysical systems, including active galactic nuclei jets, gamma ray bursts, and PWNe, relativistic inflow velocities are expected [9]. Additionally, shock formation can occur in the presence of extreme magnetic fields, as in PWNe where the magnetic energy density may exceed the plasma energy density, $\sigma = B^2/\mu_0 \gamma_0 \rho c^2 > 1$ [46]. However, experimental exploration of shock formation in relativistic electron plasma conditions has thus far been limited to laser-driven electrostatic shock ion acceleration concepts [16,132].

5.2 Experiment

In this work, experiments using two laser pulses with very different intensities and pulse durations established plasma conditions for collisionless shock formation driven by relativistic electrons and with magnetization, $\sigma > 1$. A schematic of the experimental setup at the OMEGA EP laser facility is shown in Fig. 5.1.

First, a moderate intensity interaction was driven by a UV long pulse (LP) beam (λ_L = 351 nm) with 1250 J of energy in a 1 ns square temporal profile focused on to thin foil targets of either 50 μm thick CH plastic, 25 μm thick copper, or 25 μm thick aluminum. The beam was focused using a Distributed Phase Plate (DPP) to produce an 819 μm di-
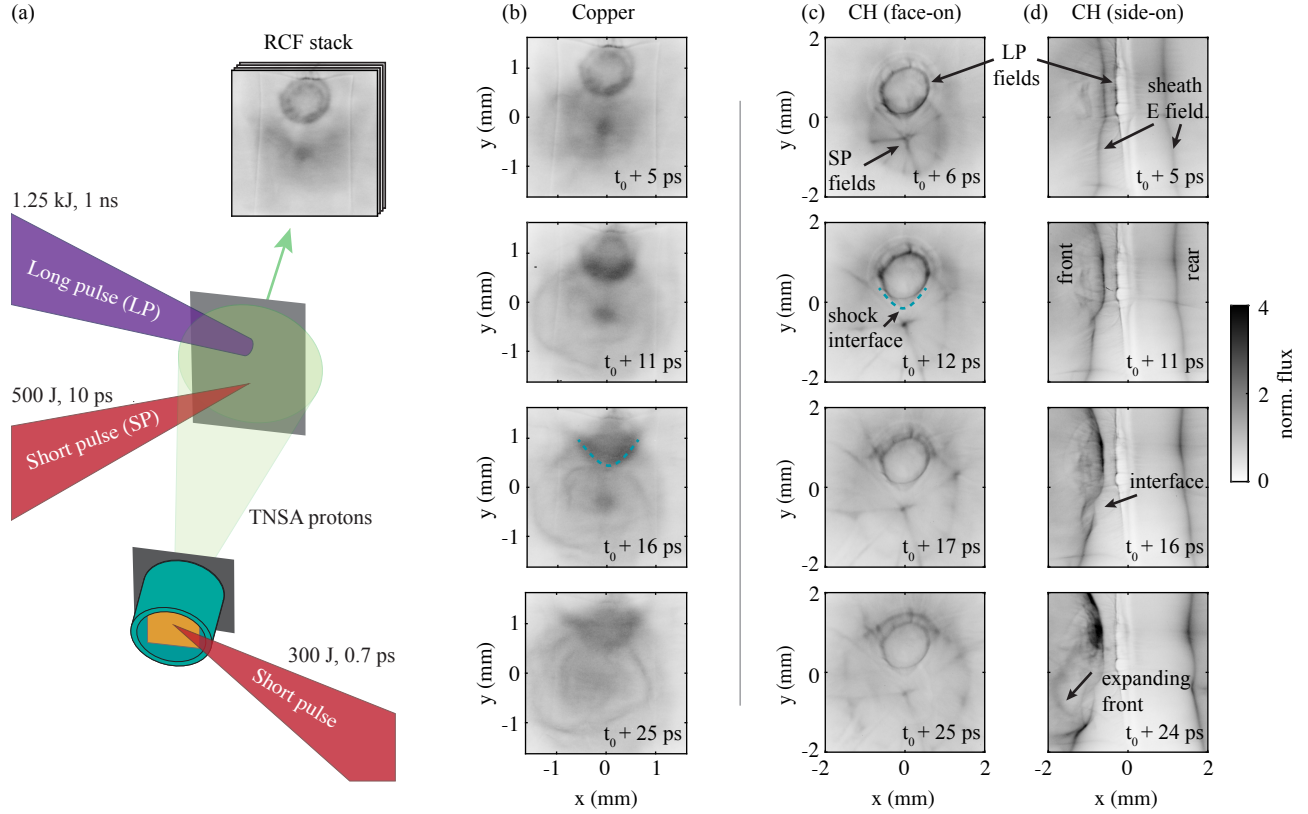
Figure 5.1: Experimental setup and results (a) Laboratory semi-relativistic quasi-perpendicular shock conditions were created by focusing a short-pulse (SP) laser next to a long-pulse (LP) laser-solid interaction. The high-intensity SP laser arrives at the foil target (copper or CH) at $t = t_0$, after the LP-produced magnetic fields had evolved for 750 ps. Protons accelerated by a second high-intensity laser-plasma interaction probe the magnetic field dynamics. A stack of Radiochromic film (RCF) recorded the proton images. (b)–(d) Experimental proton images show the temporal dynamics for three shots: (b) face-on probing of the interactions on a copper foil, (c) face-on with a CH foil, and (d) side-on with a CH foil (the main target rotated 90° with respect to the proton probe). Shock features appear in the face-on images ~ 10 ps after the SP-driven fields begin to evolve. The side-on images capture the strong sheath electric field due to target charging, as well as late-time field expansion from the shock region. Note that edges of the rectangular foil target are visible in the copper-target results (b). Larger foils and lower magnification were used for the CH-target shots in (c) and (d).

ameter (diameter encircling 95% of the energy) super-Gaussian spot with an intensity of approximately 2×10^{14} Wcm^{-2}. As the laser pulse ablates the surface, perpendicular temperature and density gradients in the plasma plume spontaneously generate an azimuthal magnetic field $\mathcal{O}(\text{MG})$ via the Biermann battery mechanism ($\frac{\partial B}{\partial t} = \frac{k_B}{en_e}\nabla T_e \times \nabla n_e$) [14, 152]. The self-generated magnetic field expands radially with a velocity near the plasma sound speed ($v \sim 10^5 - 10^6$ m/s) [19, 153]. Nernst advection confines the fields to the high density plasma near the target surface where the plasma pressure dominates the magnetic pressure ($\beta = nk_BT/(B^2/2\mu_0) \sim 1 - 100$) [154–156].

After the moderate intensity interaction had evolved for 0.75 ns, a high-intensity pulse was focused nearby, with a center-to-center spot separation of 1.25 mm. This was an infrared (IR) wavelength short-pulse (SP) containing 500 J in 10 ps was focused to a 15 μm (radius encircling 80% of the energy) spot with an intensity of $5 \pm 1 \times 10^{19}$ Wcm^{-2}. At these intensities, the laser accelerates electrons within the focal volume to relativistic velocities. The rapid expansion of a relativistic surface current establishes a target-normal sheath electric field [157] and generates an azimuthal magnetic field surrounding the focal spot. The magnetic field generated by the SP can be orders of magnitude stronger than the Biermann fields in the LP-produced plasma $\mathcal{O}(100 \text{ MG})$ [20, 71]. Indeed, the SP magnetic fields can be so strong that the magnetic energy density exceeds the rest mass energy density of the plasma electrons ($\sigma_{cold,e} > 1$) [39]. The neighboring LP-produced plasma is effectively a quasi-static obstacle to the flow of relativistic electrons and the associated magnetic field.

Protons accelerated by the target normal sheath acceleration (TNSA) mechanism [123, 158–160] were used to image the magnetic field dynamics under the asymmetric reconnection setup in a point-projection geometry with geometric magnifications of $\sim$10–14. The second OMEGA EP high-intensity laser with 300 J in a 0.7 ps pulse was focused to intensities exceeding 10^{20} Wcm^{-2} on to 1×1 mm^2 foils. The proton source foils, either 50 μm thick copper or 20 μm thick gold, were mounted within a plastic tube capped by a 5 μm tantalum foil in order to protect them from x-ray preheat and coronal plasma produced during the

main interaction. After passing through the magnetic fields, the proton beams were detected by stacks of radiochromic film (RCF). Deflections from fields will result in proton fluence modulations on the film, and the relative distribution compared to the undisturbed beam profile can provide a quantitative measurement of path-integrated field strengths [63, 107, 161].

During transit between the source and main interaction, time-of-flight dispersion of the broad proton spectrum makes possible single shot, time-resolved measurements of ultrafast dynamics with picosecond temporal resolution. The relative timing between laser pulses could be adjusted with ±20 ps accuracy in order to measure the dynamics of more slowly evolving features associated with the moderate intensity interactions. Based on the RCF stack design, the relative time-of-flight between RCF layers was 3 ps to 6 ps.

The experimental results are summarized in Fig. 5.1(b)-(d) and analyzed in Fig. 5.2. Each column in Fig. 5.1(b)-(d) shows single-shot proton imaging of the field generation and interaction dynamics over picosecond-timescales for three configurations. The shots in Fig. 5.1(b) and (c) measured the fields in a face-on probing geometry (as illustrated in the setup schematic Fig. 5.1(a)) for a copper or plastic (CH) foil target, respectively.

In both cases, the LP-produced plasma has already evolved for 750 ps and the Biermann battery magnetic fields deflect protons inward to create a ring-shaped feature of proton accumulation. The time $t = t_0$ is defined by the onset of features associated with the SP which evolve over the following time slices. As described in Sarri *et al.* [20], the SP-driven fields produce a central spot surrounded by an expanding ring in the proton image. This is evidence of a competition between the focusing magnetic field orientation generated on the front surface (spot) and defocusing orientation on the rear surface fields (ring). While the rear fields do not directly interact with the LP-produced plasma, the ring feature helps delineate the extent of the relativistic electron flows which sweep across both surfaces with similar speeds [20, 71]. Consistent with Ref. [20], tracking the ring-feature expansion yields an estimated initial flow velocity of ∼0.5c, which slows to ∼0.1c as the ring reaches a radius
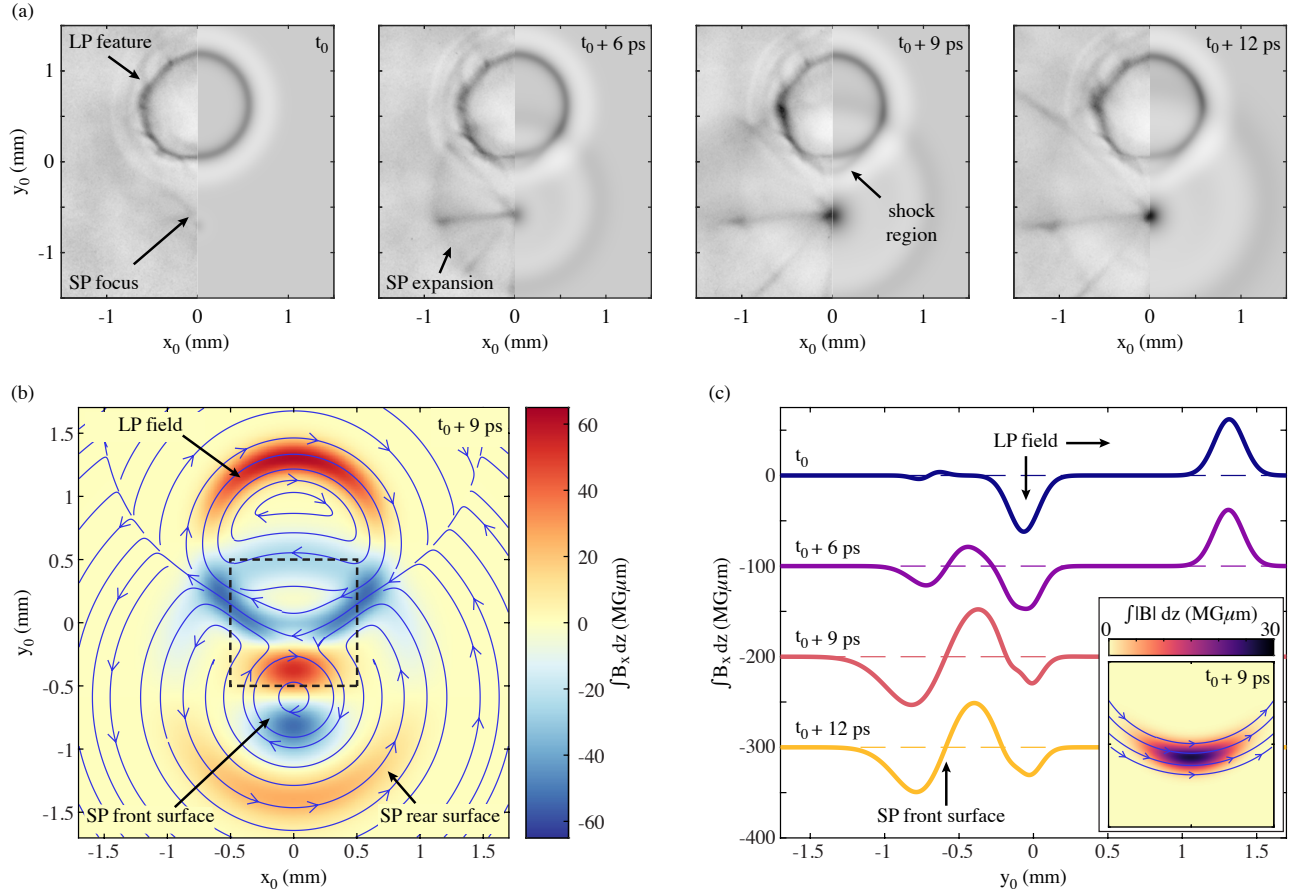
Figure 5.2: Summary of experimental results (a) Experimental proton images (left half of each time slice) from a single shot are compared to corresponding forward modeling results (right half). (b) An example path-integrated field map from the forward modeling analysis for $t = t_0 + 9$ ps shows the magnetic structure of the shock region between the LP fields and the SP front surface fields. Streamlines of path-integrated magnetic field are overlaid on a map of the horizontal field component ($\int B_x dz$). The path-integrated amplitudes appear similar between the LP and SP-produced fields, but the SP fields are generated in a thin layer along the surface ($\Delta z_{SP} \ll \Delta z_{LP}$) so the fields are significantly stronger ($B_{SP} > 10 \times B_{LP}$). (c) Line-outs from the field profiles for each time slice in (a) demonstrate the ultrafast temporal evolution of the magnetic fields and the modulation of the LP-produced Biermann fields at the shock. Rear-surface fields are excluded from (c) to emphasize the front surface dynamics. The inset plot in (c) shows an isolated 2D view of the draped magnetic field modulation from the dashed box region in (b).

exceeding 1 mm. The proton images for the CH foil also exhibit spoke-like features in the SP fields likely caused by azimuthal perturbations due to the resistive filamentation instability in the cold and dense parts of the insulating target [162] (this effect is not considered in the forward modeling of the asymmetric reconnection dynamics shown in Fig. 5.2).

After t_0+5 ps, the two plasmas collide and a cone-like feature develops at the discontinuity as the SP fields are driven into the Biermann battery fields (highlighted by dashed lines in Figs. 5.1(b) and (c)). Note that the image resolution for the shot with a copper foil is degraded due to probe proton scattering in the target. In addition, the image contrast is impacted by a non-uniform background signal of protons emitted by the main target itself. Switching to a CH foil for the main target improved the image resolution, and facilitated further analysis of the magnetic field profiles (summarized in Fig. 5.2).

The probing geometry was rotated 90° to enable side-on proton deflectometry of similar times during the system evolution. The side-on measurement (Fig. 5.1(d)) is most sensitive to the sheath electric fields generated by target charging during the SP interaction. Nevertheless, the proton images capture the disruption of the sheath field at the discontinuity, as well as evidence of an expanding front at later times. This likely indicates a build-up of SP-generated fields at the discontinuity to cause the increased proton deflections.

To elucidate the magnetic field dynamics measured in the face-on geometry, a forward modeling method was employed whereby the experimental proton radiographs are compared to synthetic images generated using test magnetic field profiles. The path-integrated fields were described by mathematical expressions, and the resulting proton deflections and synthetic images were calculated based on the analysis presented in Ref. [63].

Each experimental image shown in Fig. 5.2(a) was normalized by an estimate of the undisturbed proton profile. This helps isolate features due to fields from the background beam shape. Undisturbed profiles were generated using a low-pass Fourier filtering. The filter shape was a 2D-Gaussian with full width at half maximum (FWHM) of $2\pi/(1 \text{ mm})$.

Parameters of the test field profiles were varied to match key features between the ex-
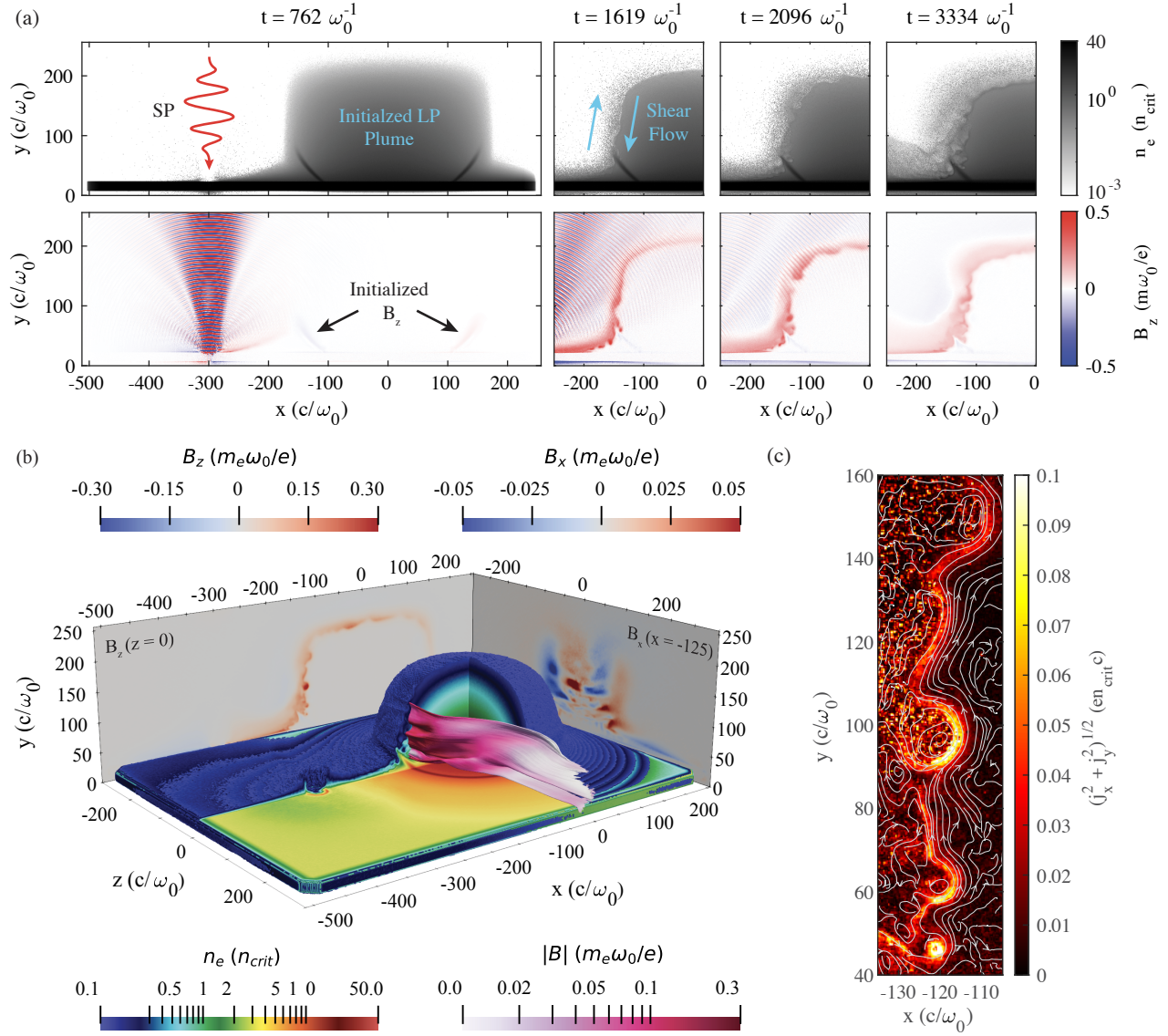
Figure 5.3: Evolution of reduced scale 3D OSIRIS simulation. (a) Slices at $z = 0$ show the interaction of an $a_0 = 5$ laser with the foil target and the subsequent flow of fast electrons driving shear and streaming instabilities at a discontinuity seen in the electron density n_e and B_z. (b) 3D isosurface of electron density at $t = 2667\omega_0^{-1}$ cutout to show the highly perturbed field lines of the SP that drape and warp due to vortices formed in the x-y plane. The roll-up is associated with strong regions of B_z (-z wall) and complex structures in B_x (+x wall). (c) A zoomed-in view of the current density in the x-y plane at the discontinuity shows several vortices that grew from unstable waves at the discontinuity formed between the hot SP accelerated electron flow and the strong return current seen here at $x \gtrsim -120c/\omega_0$.

perimental data and synthetic images (such as ring radius, cone position, and peak signal in the SP position). The expression used to define the SP front surface fields is given:

$$B_f(r_{SP}) = B_{0,f}\sqrt{\pi}l_{z,SP}\frac{r_{SP}}{a_f}\exp\left(-(r_{SP}/a_f)^2\right) \tag{5.1}$$

where $B_{0,f}$ is the peak path-integrated strength on the front, $l_{z,SP}$ is the thickness of the SP fields along the proton propagation direction ($\hat{z}$), $r_{SP} = \sqrt{x^2 + (y - y_{0,SP})}$ is the radial coordinate centered at the SP vertical position, and a_f is the characteristic transverse width. This expression is based on the ellipsoidal blob magnetic field profile discussed in Ref. [63]. The SP rear surface field is defined using a toroidal Gaussian profile:

$$B_b(r_{SP,b}) = B_{0,b}\sqrt{\pi}l_{z,SP}\exp\left(-\left((r_{SP,b} - R_{0,b})/l_{r,b}\right)^2\right) \tag{5.2}$$

where $B_{0,b}$ is the peak rear field (subscript b for 'back' used to help distinguish between rear and radial quantities), $R_{0,b}$ is the radial distance to the center the torus, and $l_{r,b}$ describes the width. Note that the front and rear SP fields are not necessarily exactly concentric.

The toroidal profile is also used for the LP fields:

$$B_{LP}(r_{LP}) = B_{0,LP}\sqrt{\pi}l_{z,LP}\exp\left(-\left((r_{LP} - R_{0,LP})/l_{r,LP}\right)^2\right) \tag{5.3}$$

but here $l_{z,LP}$ is the thickness of the LP fields, and $r_{LP} = \sqrt{x^2 + (y - y_{0,LP})}$ is the radial coordinate centered at the LP vertical position, $R_{0,LP}$ is the radial distance to the center the torus, and $l_{r,LP}$ describes the width.

Finally, the draped field enhancement feature (subscript d below) is represented by a truncated torus composed of an elliptical ring multiplied by a Gaussian in the angular direction:

$$B_d(r^*_{LP}, \theta_{LP}) = B_{0,d}\sqrt{\pi}l_{z,d}\exp\left(-\left((r^*_{LP} - y_{0,d})/l_{r,d}\right)^2\right)\exp\left(-\left(\theta_{LP}/\theta_0\right)^2\right). \tag{5.4}$$

Here, $r_{LP}^* = \sqrt{\epsilon x^2 + (y - y_{0,LP})^2}$, where ϵ defines the eccentricity of the ellipse centered on the LP fields, and $y_{0,d}$ sets the vertical offset distance between the LP and draped field features. The width is defined by $l_{r,d}$, θ_0 describes the angular extent of the draped field around the LP, and θ_{LP} is the angular coordinate for the LP field with $\theta_{LP} = 0$ along the central axis between the two laser spots.

For each time slice in Fig. 5.2(a), the panel is split to compare experimental data (left half) with synthetic proton images generated using the previously stated analytic expressions to describe the magnetic fields. Key features of the experimental proton images can be reproduced, including the cone feature at the discontinuity. Fig. 5.2(b) shows the horizontal component of the path-integrated field profile at t_0+9 ps. The LP-produced Biermann battery fields are located in the upper half of the image, and the path-integrated field strength is consistent with previous experimental measurements [18]. The fields associated with the SP expand from the lower half of the target into the LP plasma obstacle. This also happens to be an asymmetric magnetic reconnection geometry [163] that is formed between the LP Biermann battery fields and the SP front surface fields. While the path-integrated amplitudes appear similar between the LP and SP-produced fields, the SP fields are generated in a thin layer along the surface ($\Delta z_{SP} \ll \Delta z_{LP}$), and the fields are significantly stronger ($B_{SP} > 10 \times B_{LP}$).

Fig. 5.2(c) shows the temporal evolution of the interacting fields from the forward modeling analysis (excluding rear surface fields for clarity). Over the picosecond-timescale, the SP fields grow and expand, driving modulation and reduction of the near-side path-integrated Biermann magnetic field profile. This modulation yields the cone feature in the proton images and develops over super-sonic and super-Alfvénic timescales with respect to LP-produced plasma. The zero-crossing point moves with $v \sim 0.07 - 0.1c$, compared to characteristic LP speeds $v_A = 5 \times 10^4$ m/s and $c_s = 2 \times 10^5$ m/s, calculated for fully-ionized CH ions using nominal values of $B_{LP} = 1$ MG, $T_e = 1$ keV, and $n_e = Zn_i = 1 \times 10^{21}$ cm^{-3} (the critical density for the SP laser frequency).

The cone-like modulation cannot be reproduced by a simple superposition of the LP and SP fields, and the 2D projection (inset in Fig. 5.2(c)) suggests a pile-up and draping of SP-driven magnetic fields at the discontinuity. The projected region thickness is 50 – 75 μm, which is comparable to the ion skin depth (d_i), where $d_i = c/\omega_{pi} \sim 10$ to 100 μm along the LP-produced plasma plume. This measurement represents an upper bound, and the region may be thinner if the interface is tilted with respect to the proton probing path. While face-on proton imaging is typically most sensitive to magnetic fields [161], the observed features may also correspond to electric fields generated at the discontinuity. The formation of electric fields or the pile-up of magnetic fields both point to the formation of a shock from the discontinuity.

Due to the extremely high energy density and ultrafast timescales of feature evolution, it is likely that the complete dynamics would not be captured by the proton images which have $\sim$ps temporal resolution. In addition, the proton images are path-integrated measurements. Information about fast dynamics driven by relativistic electrons could be lost during the relatively slow transit of protons across the fields. The relatively thin shock region also indicates that electron-scale microphysics could influence the dynamics below the spatial resolution of the proton source ($\sim$15 μm).

5.3   Simulations

To study the relativistic electron-driven shock microphysics, a reduced scale 3D simulation was performed using the fully relativistic particle-in-cell code OSIRIS 4.0 [109, 110]. A convergence tested, full-scale 3D PIC simulation of the interaction with box dimensions $\mathcal{O}(\text{mm})$ and time duration $\mathcal{O}(\text{ns})$ is not possible on currently available supercomputers, therefore several simplifications were made. The LP-generated plasma plume was initialized in OSIRIS based on fits to extended-MHD simulation results at t = 750 ps. The density, temperature, and fields of the long-pulse generated plume were informed by the results

of extended-magnetohydrodynamics (MHD) simulations using realistic laser parameters and target densities performed with the code GORGON [164–166]. Details of the extended-MHD modeling discussed in Ref. [18]. Fits were performed to the GORGON data and input into OSIRIS at 1/25th reduced scale. The spatial scale and SP duration were reduced by 25 times, however, the peak magnetic field strength, temperature, and density of the LP-generated plume near the interaction region were maintained to preserve β. A relativistic intensity laser pulse (SP $a_0 \approx \sqrt{I\lambda_{\mu m}^2/1.4 \times 10^{18}(\text{Wcm}^{-2}\mu\text{m}^2)} = 5$) was injected from the positive y-boundary and focused onto a target. The target consisted of electrons and ions with a normalized mass-to-charge ratio $m_i/Zm_e = 3672.3$, and the peak density was set to $40n_c$. A thickness of 15 c/ω_0 was found to be sufficient to stop the laser pulse from hole boring through the target. The target density profile was tapered to the boundaries to reduce boundary effects. The simulation box was initialized with dimensions of $768 \times 256 \times 600$ $(c/\omega_0)^3$, a resolution of 3 cells/(c/ω_0), 64 and 27 particles per cell for electrons and ions, respectively. A laser pulse polarized in the x-direction was injected from the +y-boundary and focused onto the surface of the target at $(x,y) = (-298.06c/\omega_0, 23.845c/\omega_0)$ with a Gaussian focal spot ($FWHM = 19.74c/\omega_0, a_0 = 5$), and Gaussian temporal profile ($t_{FWHM} = 715.4\omega_0^{-1}$). Open boundary conditions were used for both electric and magnetic fields and particles. The simulation was run on the NASA Aitken Supercomputer using 51200 cores and ~ 2.5M CPU core hours. The evolution of this system is summarized in Fig. 5.3(a).

During the high-intensity laser interaction, strong azimuthal B-fields (~ 0.3 ($\text{m}_e\omega_0/e$) or 3 kT) are generated by the expanding relativistic electrons along the target surface. These fields propagate out radially at $\sim 0.2 - 0.4c$, similar to the experimental expansion velocity. As the hot magnetized electron flow approaches the LP-generated plume, it induces a fast diamagnetic return current consisting of LP plume electrons in a thin layer that falls off exponentially with a characteristic length consistent with the LP plume electron skin depth, d_e. This return current shields the LP plasma, diverts the hot magnetized electron flow around the plume and causes the SP-driven B-fields to drape around the LP plume
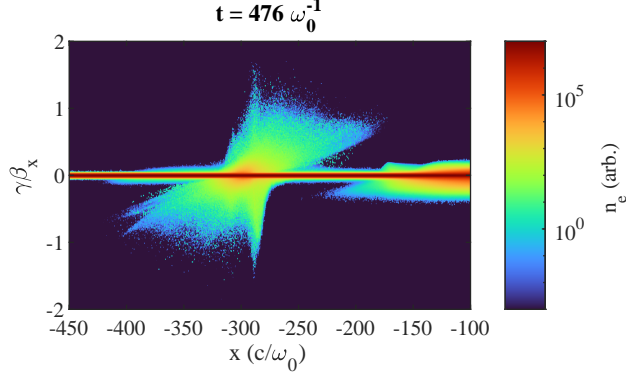
Figure 5.4: Electron momentum before interacting at the discontinuity. Electron phase space at early times integrated over the simulation box in y and z shows an inflow of electrons before interacting with the LP-generated plume. This inflow is at a large fraction of c, therefore relativistic effects will be important to the shock interaction.

(illustrated by streamlines in Fig. 5.3(b)). Along this discontinuity $\sigma_{cold,e} > 1$ within the SP-accelerated plasma. The electron inflow initially appears as a beam with a normalized momentum $\gamma v_x/c \sim 0.6$, before becoming a thermal distribution as the laser continues to heat the target and the electrons interact with the LP-generated plume (Fig. 5.4). Considering a lineout of electron density at $y = 95c/\omega_0$ and $z = 0$, the LP-generated plume initially compresses rapidly at a velocity of $\sim 0.03c$ generating a shock for $t \geq 2500\omega_0^{-1}$ that propagates at $\sim 0.006c$ into the LP plume ($+x$-direction) in the simulation frame. The compression velocity is similar to the velocity of the zero crossing point extracted from the experimental proton images through the forward model. Compared to the nominal sound speed in the LP plume ($c_s \approx 5 \times 10^5$ m/s) the late-time shock propagation corresponds to a Mach number $M \approx 4$.

This is a quasi-perpendicular shock where the magnetic fields are perpendicular to the shock normal, however, this is a special case where the fields also form a reconnection geometry at positions in y where the LP fields exist. Additionally, this system has a large shear at the discontinuity facilitating the formation of an unstable interface (Fig. 5.3(c)) likely due to the combination of magnetized electron-scale Kelvin Helmholtz instability (ESKHI) and the lower-hybrid drift instability (LHDI) [167, 168].

The instability initially appears as oscillations in B_z and n_e along the LP-generated plasma plume pedestal in the x-y plane. This unstable mode grows with a wavelength $\sim 6.5 - 14(c/\omega_0)$ and a phase velocity $0.05c$ to $0.07c$. Eventually, the wave grows into tight spirals of current density that surround B_z stronger than the SP-generated B-fields (Fig. 5.3 (c)). The instability develops ripples in the draped magnetic fields along the discontinuity and causes the field lines to twist (Fig. 5.3 (b)). These features evolve rapidly and are too small to be resolved in the side-on proton radiographs, however the late-time expansion of the unstable interface (Fig. 5.3 (a) $t = 3334\omega_0^{-1}$) may be captured in Fig. 5.1 (d) at $t_0 + 16$ ps and $t_0 + 24$ ps. Specifically, the position labeled "interface" at $t_0 + 16$ ps may be associated with the plasma near the SP focal spot expanding into the expanding LP-generated plume, forming a higher density region with an angle similar to that of the initial LP plume magnetic fields.

To investigate the instability developed at the discontinuity, two 2D simulations were performed recreating the x-y plane at z = 0 from the 3D simulation except at a larger $1/10^{th}$ scale, with a higher resolution. The SP laser pulse duration was also scaled accordingly ($t_{FWHM} = 1790.1\omega_0^{-1} \approx 1$ ps for a 1-μm laser wavelength). The simulation box was initialized with dimensions of $1920 \times 640(c/\omega_0)^2$, and a resolution of 10 cells/(c/ω_0). Other parameters, like laser intensity, peak density, or ion charge-to-mass ratio, were identical to the 3D simulation.

The LHDI growth is suppressed in the case of stationary ions where ion mass is effectively infinite [169]. Therefore, one simulation was performed with mobile ions, like the 3D simulation, and the other was performed with stationary ions. The results are compared in Fig. 5.5(a) and (b). Instabilities still form in the stationary ion simulation and generate large spirals, a characteristic feature of ESKHI. In the mobile ions simulation, some vortices are observed, however, the largest change is the appearance of a shock that propagates into the LP plume. Overall, the large-scale vortices are suppressed with mobile ions and other wave-like features along the shock could be related to the interplay between ESKHI
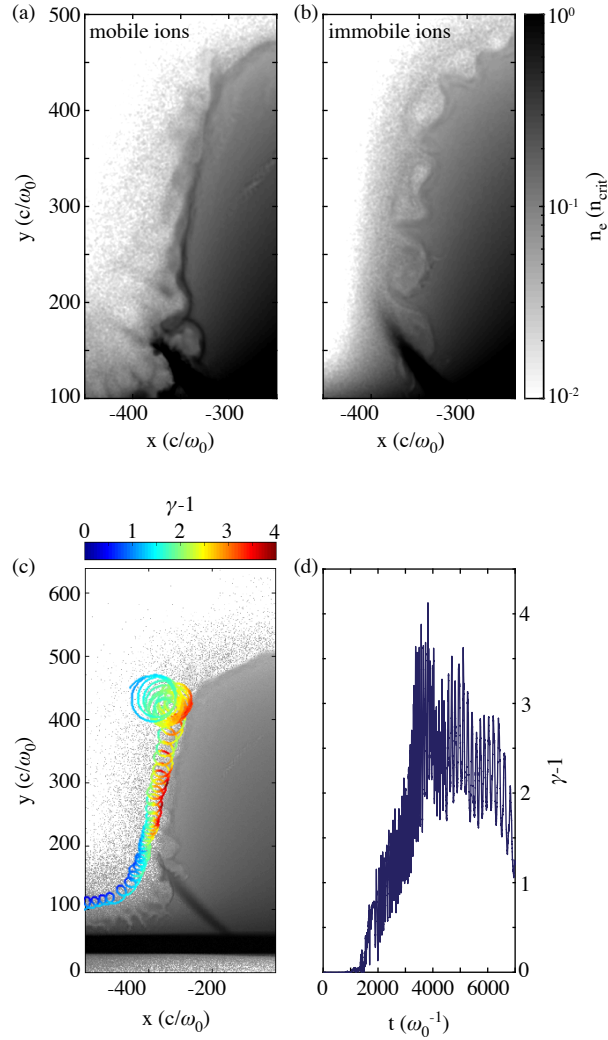
Figure 5.5: Unstable interface and particle energization. 2D simulations at $1/10^{\text{th}}$ scale with (a) mobile ions and (b) immobile ions. Immobile ions simulation shows characteristic ESKHI vortices. These vortices are largely suppressed in the mobile ions simulation. (c) Particle tracking in the mobile ions simulation shows a magnetized electron gaining energy as it drifts along the shock. (d) The evolution of the tracked electron's energy.

and LHDI [167]. The shock front is much smoother in 2D than 3D. This is likely because electrons are confined to the x-y plane in 2D and therefore must propagate along the LP interface while in 3D they can propagate out-of-plane, creating a non-uniform compression.

To explore electron energization near the shock front, the simulation tracked 200 particles that were randomly selected from the subset of electrons with $\gamma > 1.49$ located within $(-500 < x < -200(c/\omega_0))$ and $(66 < y < 280(c/\omega_0))$. Half of the tracked electrons were selected at t = 2599.8 ω_0^{-1} (near the beginning of shock formation) and the other half at t = 3899.7 ω_0^{-1} (after the instability developed) in an attempt to capture temporal changes to the acceleration. An example of electron particle tracking is plotted in Fig. 5.5(c) and (d). Following a trajectory characteristic of shock drift acceleration (SDA), the electron gains energy while gyrating along the shock front. SDA can play a critical role in pre-energizing particles from the thermal background for injection into diffusive shock acceleration, the mechanism widely invoked to explain energetic cosmic rays and non-thermal emission from supernova remnants [170, 171]. Although some electrons follow similar trajectories, they make up a small fraction of the total hot electron population including electrons from the SP focal region. In experiments, global electron acceleration will likely be dominated by laser-plasma interactions, therefore signatures of SDA may be challenging to distinguish. However, future laser-driven shock experiments built on this work could enable laboratory measurements of electron energization at quasi-perpendicular shocks.

Analyzing the dynamics of the anti-parallel magnetic fields that may reconnect at the discontinuity is non-trivial. Quadrupolar Hall-type magnetic fields are formed in 2D slices of the x-z plane indicative of collisionless reconnection, however, these fields could also be generated by the shear flow at the discontinuity (Fig. 5.6). The formation of large target-normal electric fields around the unstable discontinuity precludes the use of standard 2D analysis where the reconnection rate is extracted from the out-of-plane electric field inside the current sheet. Therefore, reconnection cannot be conclusively demonstrated from this simulation. The many filaments that form in the x-z plane, and the current density vortices
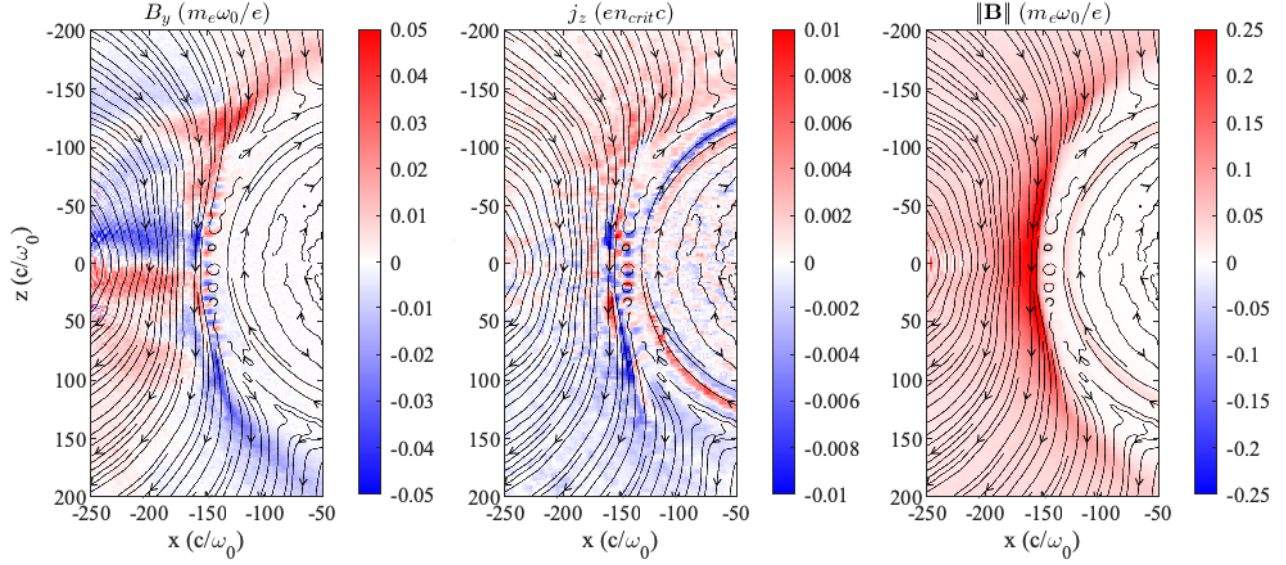
Figure 5.6: Dynamics of anti-parallel fields at the discontinuity. Slices at $y = 43.8c/\omega_0$, $t = 1524\omega_0^{-1}$, colormaps show the diagnostic noted in the title of each plot. Streamlines depict the $B_x - B_z$ field lines which form an asymmetric reconnection geometry at the discontinuity. Hall-type field patterns are seen in B_y with associated current density j_z, however, these field and current density patterns may also be regulated by the shear flow at this discontinuity.

at the discontinuity (Fig. 5.3(c)) may prevent relatively simple x-point reconnection in the experiment. Instead, the reconnection dynamics are likely impacted by 3D effects, and potentially more relevant to reconnection in turbulent systems forming on electron scales [172].

5.4 Conclusions

This work demonstrates experimental evidence of a collisionless shock driven by strongly magnetized relativistic electrons, and marks an important step towards the detailed study of shocks in conditions relevant to extreme astrophysical environments. As in-situ measurements are currently unattainable, laboratory experiments can provide critical insights into the microphysics of such shocks. Future experiments may focus on the instabilities at the discontinuity, including ESKHI which has been suggested as a possible mechanism for

broadening of spectral lines used for measuring shock velocities in a pulsar binary [173]. Next-generation ultra-intense laser facilities may also extend this experimental platform to much more energetic interactions where inflowing particle energies and fields are larger and quantum-electrodynamics processes may become important to shock physics.

Magnetic Field Generation at Extreme Laser Intensities

In this chapter magnetic field generation in ultra-intense laser-solid interactions is studied over a range of laser intensities relevant to next-generation laser facilities ($a_0 = 50 - 500$) using 2D particle-in-cell simulations. It is found that fields $\mathcal{O}(0.1)$ MT (1 GigaGauss) may be generated. However a significant fraction of the energy budget is converted to high-energy photons, $\sim 38\%$ at $a_0 = 500$, greatly reducing the available energy for field generation. A model for the evolution of the target-surface fields and their scaling with a_0 is developed using laser parameters and assumed values for the average radial velocity and reflectivity. The model and empirical scaling allow for the estimation of field strengths on the next generation of laser facilities, a necessary component to the proposal of any future magnetized experiment.

6.1   Introduction

Magnetic fields are an important component of many high energy density physics (HEDP) laboratory experiments e.g. the study of magnetized shocks [69], magnetic reconnection [34, 39, 174], and magnetized turbulence [78]. These studies are generally motivated by astrophysical systems where the magnetic fields have been theorized to be produced by the Biermann battery [14], magnetic dynamos [175], or instabilities [176]. In the laboratory,

magnetic fields can be produced external to the interacting plasma though the use of conducting coils [177] or they can be self generated by the movement of the plasma. Lasers are commonly used as a tool to generate the plasma conditions where strong magnetic fields can be generated.

In the simple interaction of a single laser pulse with a solid target strong magnetic fields can be generated. These fields are carried by the hot electrons that expand radially from the laser spot on the target. The strength and spatial profile of the fields varies greatly depending on the target material, density profile, and laser parameters. Various experiments have been performed at moderate laser intensities ($\sim 10^{14} - 10^{15}$ W/cm^2) using long-pulse (ns) lasers and have generated fields $\mathcal{O}$ (100 T) [19, 34]. Simulations have shown that field generation in this non-relativistic regime is well characterized by the Biermann battery effect where perpendicular electron density and temperature gradients are responsible for field generation, $\partial B/\partial t \propto \nabla T_e \times \nabla n_e$ [14, 18, 178].

In the higher intensity relativistic regime, where laser field strengths become large enough to accelerate electrons to energies in excess of their rest mass ($a_0 = eE/m_e\omega_L c \approx \sqrt{I\lambda_{\mu m}^2/1.4 \times 10^{18}(\text{Wcm}^{-2}\mu\text{m}^2)} > 1$), field generation is not well understood. Solid target laser experiments have been performed in this regime, measuring generated magnetic field strengths $\mathcal{O}$ (10 kT) using particle deflectometry [20, 71, 174]. Shukla *et al.* performed particle-in-cell (PIC) simulations studying field generation with $a_0 \approx 1$ and found that Biermann magnetic field generation was dominant in the outer expanding plasma [103]. Recently, other schemes for field generation have been studied including the amplification of seed magnetic fields [179], and the formation of strong magnetic fields along a channel wall formed by an intense $> 10^{22}$ W/cm^2 pulse interacting with an overdense target with a tailored density profile [180]. A method for measuring fields in even higher intensity $> 10^{23}$ W/cm^2 interactions with near-critical density targets using the spin of ejected electrons has been proposed [181].

As the next generation of laser facilities comes online and push to even higher laser
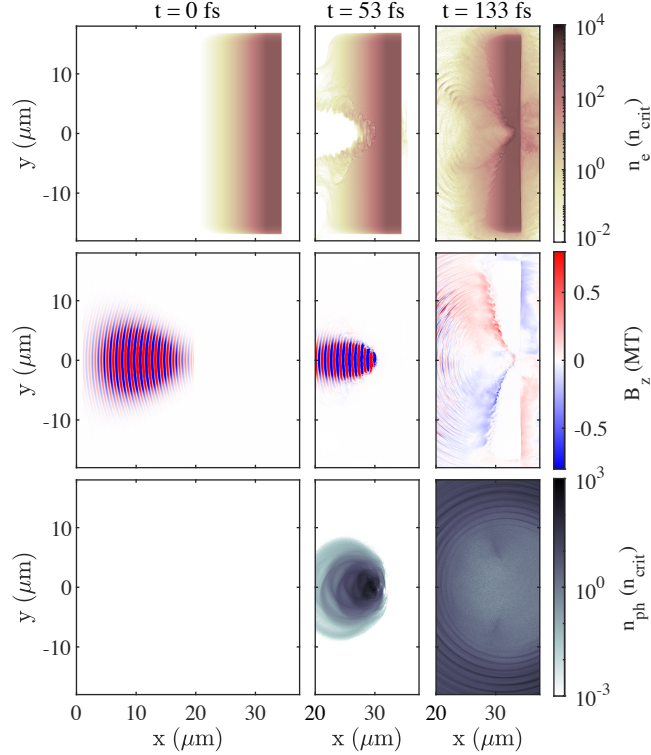
Figure 6.1: Evolution of electron density n_e, out-of-plane B-field B_z, and photon density n_{ph} for photons with energies $> 2m_ec^2$ from the interaction of a 20 fs, $a_0 = 500$ laser pulse with solid density target consisting of electrons and Al^{13+} in a 2D OSIRIS simulation.

intensities, perhaps $> 10^{23}$ W/cm^2, field generation may become more complex as quantum electrodynamic (QED) effects, i.e. nonlinear Compton emission and pair creation, could affect the dynamics of the system [2, 93]. Understanding how magnetic fields form and how the resulting field strength scales with laser intensity in this ultra-intense regime will be fundamental to any magnetized experiment performed using solid targets at these laser facilities. Here, we study the field generation in this regime using QED PIC simulations over a large range of laser intensities ($a_0 = 50 - 500$). A scaling for the surface fields formed outside the focal volume as a function of a_0 is found and equations are derived to model the interaction allowing for the estimation of field strengths from experimental parameters.

6.2   Simulations

Simulations were performed in a 2D rectangular box using the particle-in-cell code OSIRIS, which includes a Monte-Carlo model for the nonlinear Compton and Breit-Wheeler strong-field QED processes in the locally constant field approximation [182, 183]. A box with dimensions 37.4 μm $\times$ 36 μm was used. A 20 fs full-width-half-max (FWHM), 1 μm central wavelength, laser pulse linearly polarized in the y-direction was initialized in the simulation box and propagated in the $+x$-direction . The pulse was focused with a FWHM of 3 μm onto a target consisting of electrons and Al^{13+} at $x \approx 31.8$ μm. Open boundary conditions were used for particles and fields on all boundaries. The particles were initialized with a peak charge density of a fully ionized solid target ($700.3n_{crit}$ or $\sim 7.8 \times 10^{23}$ cm^{-3}) over a thickness of 2.5 μm. At this density the collisionless skin depth $c/\omega_p \approx 6$ nm. An exponentially decaying density ramp was initialized as the front edge of the target with a characteristic decay length of 1 μm to approximate a pre-plasma. It is unclear what this scale length will be because pre-plasma at these extreme intensities has not been previously characterized and will be laser-facility dependent. However, at the simulated intensities, extreme laser contrasts would be required to not have a pre-plasma, therefore simulations without a pre-plasma are not realistic. The target was tapered to the boundary in the y-direction to minimize boundary effects. The box was initialized with resolutions $\Delta x = 10.6$ nm and $\Delta y = 22.7$ nm, generating a grid with 3525×1582 cells. Each particle species was initialized with 400 particles-per-cell. Simulations were performed with a range of a_0 from 50 to 500. The timestep was set to $1/500\omega_L^{-1}$ for $a_0 = 400$ and 500, and $1/267\omega_L^{-1}$ for $a_0 \leq 267$, where the laser frequency $\omega_L = 1.885 \times 10^{15}$ rad/s. These values are smaller than the time step required for the CFL condition ($0.06\omega_L^{-1}$) [113].

6.3 Results

The dynamics of the $a_0 = 500$ simulation are shown in Fig. 6.1 which shows 2D maps of plasma density, magnetic field, and emitted photon density at 3 time snapshots. As the laser pulse interacts with the target, it rapidly accelerates the electrons from the central part of the target in all directions with electron fluid velocities approaching c. The hot electrons generate strong out-of-plane magnetic fields B_z on the front and back surfaces of the target. The spatial profile of the front-surface magnetic fields are not smooth. This is due to a combination of the modulation of the electron density by the laser and shear or streaming instabilities due to the large return current. The target is shielded from the magnetic fields by a fast moving cold return current that exists in a thin layer at the surface of the target. Due to the finite charge of the target, as the return current moves toward $y = 0$, the target electron density depletes, causing it to shrink in the x-direction. This leaves behind ions which are approximately stationary outside the focal volume. The laser-accelerated electrons flow into this depleted region, forming a density profile similar to that of the initial ion profile.

Once the laser pulse reaches the relativistic critical density given by $n_{crit} = \langle\gamma\rangle m_e \varepsilon_0 \omega_L^2/e^2$, a fraction of the pulse is reflected. As the laser reflects from the target, it sets up a standing wave that interacts with the hot electrons that exist within the channel formed by hole-boring, creating the conditions for radiation to be produced on the timescale of the interaction. Electrons begin strongly radiating within the focal volume at ~ 53 fs (Fig. 6.1 row 3). The photons shown have energies $> 2m_e c^2$ (see Fig. 6.2 for electron and photon spectra). While radiation is emitted in all directions, there is a bias towards the reflected laser direction. Since highly-relativistic electrons emit photons along their direction of motion, this radiation pattern reflects the underlying angular distribution of the accelerated electrons.

Fig. 6.3 shows the time evolution of the energy budget for $a_0 = 50$ and 500 and the trends of the energy components for various a_0. The laser pulse is initialized in the simulation
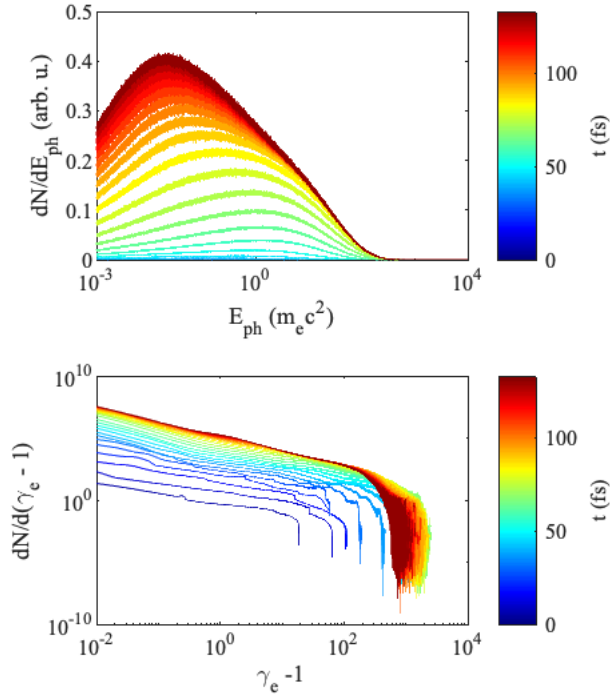
Figure 6.2: Time evolution of photon and electron energy spectra integrated over the simulation box for $a_0 = 500$. Here, E_{ph} is the photon energy normalized to the electron rest mass energy $(m_e c^2)$.
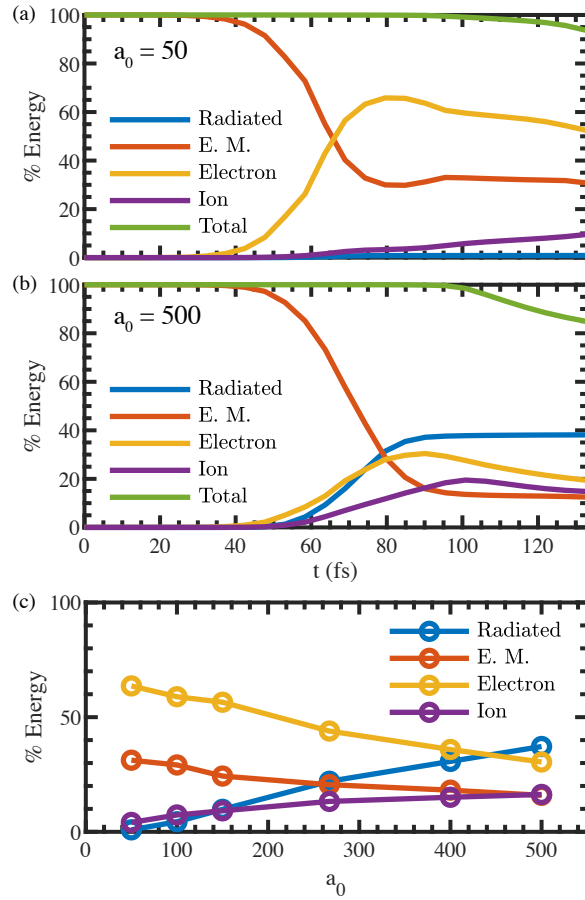
Figure 6.3: Energy budget of 2D simulations at $a_0 = 50$ and 500, and the scaling of each component of energy with a_0 at $t = 90.2$ fs.

domain and defines the initial total energy of the system. As it interacts with the target, the laser energy is initially converted into electron kinetic energy, which is subsequently converted to ion kinetic energy, radiated energy (high energy photons), and forms the electric and magnetic fields on the target. The final electromagnetic field energy (E. M. in the plot legend) is made up of the contributions from all electromagnetic fields in the simulation box. To decouple the laser field from the target fields, the fields outside the target surface were integrated at a time after the interaction was over and before the reflected laser exited the box. This gave a reflectivity of $\sim 22\%$ at $a_0 = 100$, and $\sim 14\%$ at $a_0 = 400$, showing that the reflectivity scales weakly with a_0 over the simulated range. The % Energy trends are taken at $t = 90.2$ fs, a time when the majority of energy still exists in the simulation box, i.e. $\%E_{total} \approx 100$ [Fig. 6.3(a-b)]. These trends show an increase in radiated energy with increasing a_0. Conversely, the electron kinetic energy decreases with increasing a_0 due to radiative cooling and makes up a smaller fraction of the total energy than radiation at $t = 90.2$ fs for $a_0 = 500$. Pair creation makes up a negligible fraction of the energy budget with only 0.054% at $a_0 = 500$.

To understand how surface magnetic field generation (B_z) scales with a_0, we extracted maximum values along the x-direction and averaged along the surface of the target in the y-direction outside the focal volume and plotted them in Fig. 6.4. These fields outside the focal volume have historically been used for characterizing the initial configuration for magnetic reconnection experiments in the standard two-pulse geometry and are therefore the most relevant for future experiments. The black circles in Fig. 6.4 are calculated by finding the maximum B_z in the x-direction and taking the mean of these values in the y-direction along the target surface between $y = 8$ to 12 μm. Error bars show the standard deviation in this region. The position of the surface where the maximum B-fields are generated is pushed to the positive x-direction as a_0 increases. For reference, lines of $B_z \propto a_0$ and $B_z \propto \sqrt{a_0}$ are shown. The scaling of B_z appears to reside between these two reference lines, however it is more similar to $B_z \propto \sqrt{a_0}$. Even with QED effects, for the range of simulated a_0,
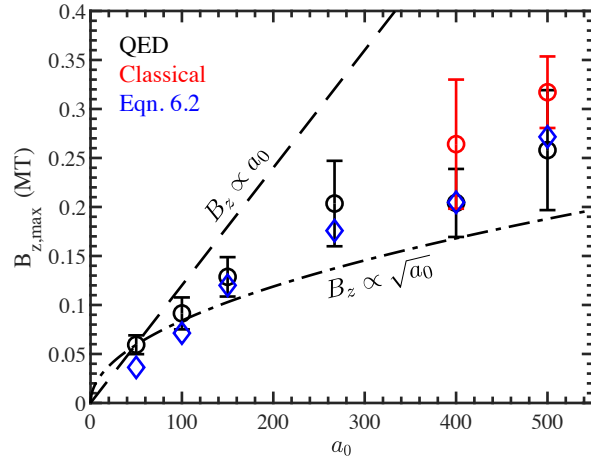
Figure 6.4: Scaling of the maximum magnetic field $B_{z,max}$ as a function of a_0. The black circles are calculated from simulations including QED effects, taking an average of maximum B_z along the target surface from $y = 8 - 12$ μm. Error bars are the standard deviation of B_z. Red circles are the mean values in simulations without radiation effects. Eqn. 6.2 was used with values of $x_{B,max}$ and $\langle u_y \rangle$ extracted from the simulation (blue diamonds).

B_z continues to grow, reaching maximum values > 0.25 MT or 2.5 GG. If a_0 were to be increased further it is unclear how the the scaling would change as pair production may become significant.

The effect of radiation reaction on field generation can be elucidated by running the simulations where photons make up a significant fraction of the energy budget, i.e. $a_0 = 400$ and 500, with QED effects switched off. The results are plotted as red circles in Fig. 6.4, which show a $\sim 29\%$ and $\sim 23\%$ increase in $B_{z,max}$ compared to the QED simulations for $a_0 = 400$ and 500 respectively. The dynamics of the interaction are quite similar outside the focal volume, however an interesting phenomenon is seen near the focal spot (see Fig. 6.5). Weibel filaments grow near the focal spot in the classical simulation, a processes previously noted by Shukla *et al.* for $a_0 \approx 1$ [103], whereas in the QED simulation these filaments are suppressed. Understanding the effects of radiation on the Weibel instability will be the subject of a future study.
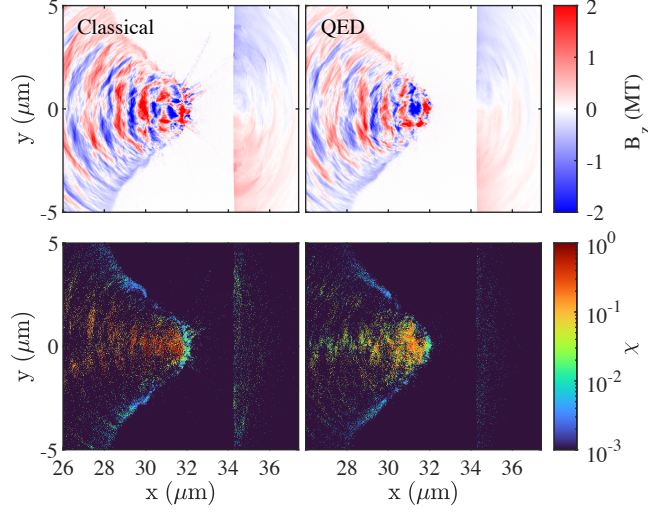
Figure 6.5: Magnetic field and χ at t = 85 fs in simulations of $a_0 = 400$ with (QED) and without (Classical) radiation showing the radiative suppression of the Weibel instability near the focal spot. $\chi = |F^{\mu\nu}p_\nu|/m_e E_{cr}$ is the ratio of the field strength in the frame of the electrons to the critical field $E_{cr} = m_e^2 c^3/e\hbar = 1.3 \times 10^{18}$ V/m and is a measure of the importance of QED effects [2]

6.3.1 Theoretical Model

To model the evolution of the fields and their scaling with a_0, we started from the following equation obtained by Schumaker *et al.* [71]:

$$B_z(x,y,t) \approx -\mu_0 \int_{-\infty}^{x} j_y(x',y,t)dx'. \tag{6.1}$$

This equation is derived from a combination of the Ampère-Maxwell equation, Gauss's law, and the continuity equation assuming negligible current normal to the target and radial electric field. Numerically integrating j_y from the -x boundary to a position x was found to give a good approximation of B_z at that position. As the laser interacts with the target, it channels and hole-bores, accelerating electrons outward, inducing a return current along the surface of the target. This causes the target to contract, leaving behind the quasi-stationary ions. The outward flowing electrons respond to the target-normal electric fields, forming a density profile similar to the initial ion density profile. The current can then be approximated

118

Figure 6.6: An example of the simple model being used to calculate the surface magnetic fields for $a_0 = 100$. (a) fit to surface where B_z is maximum from Eqn. 6.3 where x_{HB} is calculated from Eqn. 6.4 using R = 0.22. (b) blue line shows $B_{z,max}$ along y at $t = 133$ fs, dash-dot black line shows the result of Eqn. 6.2 from the surface in (a). (c) space-time plot of B_z at $y = 8$ μm and the result of Eqn. 6.3 (black line). (d) Evolution of $B_{z,max}$ (black circles) within ± 1 μm of the line in (c) and the result of Eqn. 6.2 (black line) calculated along this line with $\langle u_y \rangle = 0.12c$. An additional blue line is shown for a lineout at $y = 10$ μm.

using a spatially averaged velocity $\langle u_y \rangle = \langle j_y/n_e \rangle$ multiplied by the initial ion charge density profile $\rho_{i0} = en_0 \exp[(x - x_0)/L]$. Substituting into Eqn. 6.1 and integrating this current to the position $x_{B,max}$ of the magnetic field maximum gives:

$$B_{z,max}(y,t) \approx e\mu_0 \langle u_y \rangle n_0 L \exp\left(\frac{x_{B,max}(y,t) - x_0}{L}\right), \tag{6.2}$$

where L is the characteristic scalelength of the pre-plasma and x_0 marks the transition point from pre-plasma to bulk density. This equation is only valid for targets with a pre-plasma, however this is the realistic case because ultra-intense laser pulses are likely to have a pre-pulse.

The position $x_{B,max}$ can be approximated by noting that the laser drives the electrons outward at $\sim c$ and an approximately linear surface is formed as the channel expands. This surface is defined by two points, one at a position x_f that propagates outward at c, and the other fixed at the point the laser hole bores to x_{HB} [see Fig. 6.6(a) for diagram]:

$$x_{B,max}(y,t) = x_f - \frac{[y - c(t - t_0)](x_{HB} - x_f)}{c(t - t_0)}, \tag{6.3}$$

$$x_{HB} = x_0 + L \ln\left(\frac{\gamma_{osc}}{n_0}\right) + 2L \ln\left[1 + \frac{c}{L}\sqrt{\frac{\ln(2)\tau^2\gamma_{osc}}{4R_{qm}}}\right], \tag{6.4}$$

where $R_{qm} = M_i/Zm_e$, $\gamma_{osc} = \sqrt{1 + (1 + R)a_0^2/2}$, R is the reflectivity, x_f and t_0 are fitting parameters, and $\gamma_{osc} \gg 1$ has been assumed. Eqn. 6.4 describes the hole boring position for a laser with the envelope $a(t) \propto \exp(-2t^2/\tau^2)$ and is modified from the equation of Kemp *et al.* [90]. Eqn. 6.3 is a linear fit to the maximum-B_z surface. The modification was made by assuming the laser hole bores with a constant $a = a_0$ for the FWHM duration of the pulse. Additionally the pulse is assumed to hole bore into an exponential density profile. If the pulse reaches the bulk target, another term must be added to the integral from which Eqn. 6.4 is derived.

An example calculation for $a_0 = 100$ is shown in Fig. 6.6. The position $x_{B,max}$ is ac-
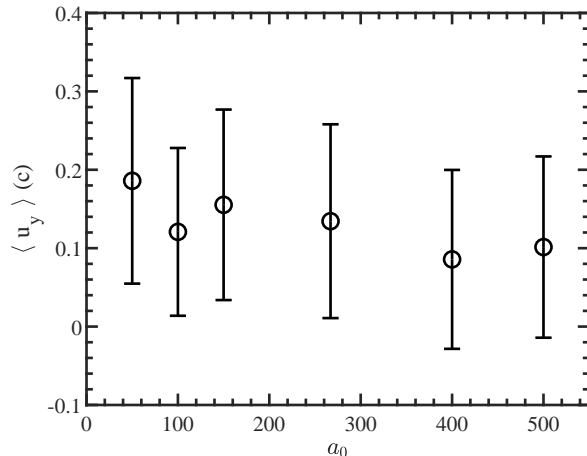
Figure 6.7: Velocity in the y-direction calculated by taking the mean of j_y/n_e in the region $y = [8, 12]\mu$m and $x = [x_{B,max} - 1\ \mu$m, $x_{B,max}]$.

curately fit through Eqn. 6.3 where x_f is taken to be the position where the exponential preplasma is truncated, and t_0 was varied until a rough fit was achieved. The value used for t_0 (20 fs) is close to the time at which the laser begins to interact with the pre-plasma. These same fitting parameter values could be used with good accuracy for all tested a_0. The maximum B_z along this line was calculated from Eqn. 6.2 and compared to the simulated values in Fig. 6.6(b). The average y velocity $\langle u_y \rangle$ was calculated by taking an average of j_y/n_e over the area defined by the positions in the y-direction from $y = 8$ to 12 μm and in the x-direction from $x_{B,max} - 1\ \mu$m to $x_{B,max}$. This y velocity scales weakly with a_0 as seen in Fig. 6.7. Similar $B_{z,max}$ magnitudes are seen outside of the focal volume; however, inside the focal volume the fields are overestimated. The equations become invalid in this region as ion motion becomes important and the surface is curved and cannot be approximated by a linear fit. However, outside the focal volume the equations provide an accurate estimate for the position [Fig. 6.6(c)] and magnitude [Fig. 6.6(d)] of the evolving fields. Additionally using Eqn. 6.2 with simulated values for $x_{B,max}$ and $\langle u_y \rangle$ a similar scaling with a_0 is found (Fig. 6.4 blue diamonds).

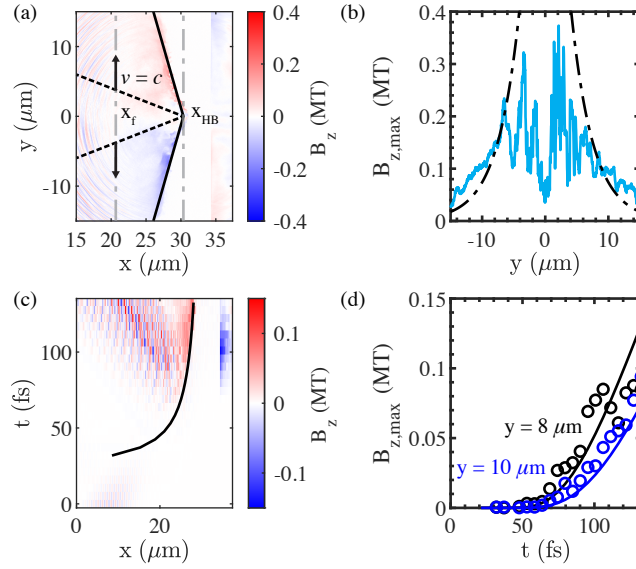Additional simulations were performed with varying scale lengths ($L = [1\ \mu$m, 0.5 μm,
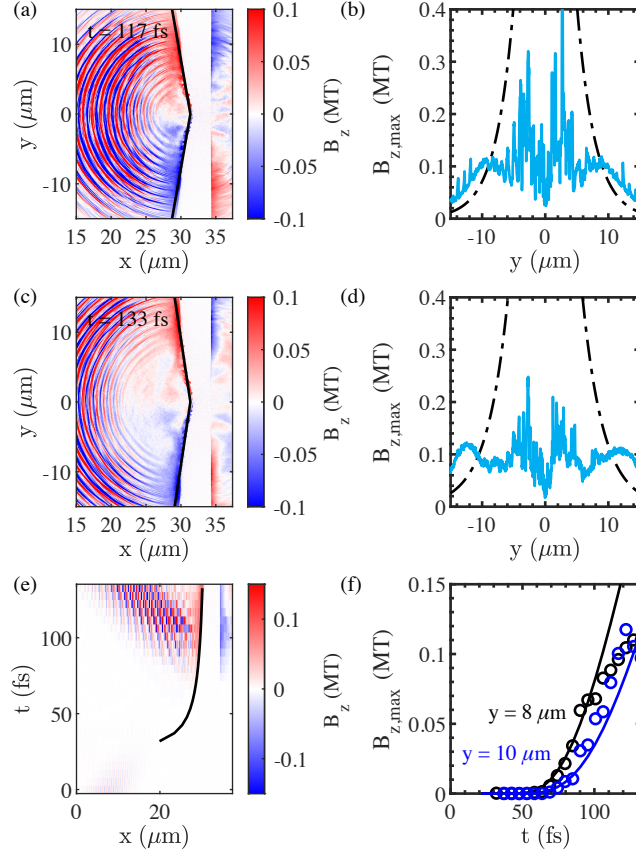
Figure 6.8: An example of the simple model being used to calculate the surface magnetic fields for $a_0 = 100$ with a 0.5 μm scale-length. (a) fit to surface where B_z is maximum from Eqn. 6.3 at $t = 117$ fs. (b) blue line shows $B_{z,max}$ along y at $t = 117$ fs, dash-dot black line shows the result of Eqn. 6.2 from the surface in (a). (c-d) are the same as (a-b) except at $t = 133$ fs. At this time the fields which appear pulse-like for this scale-length begin exiting the box and no longer match the theory. (e) space-time plot of B_z at $y = 8$ μm and the result of Eqn. 6.3 (black line) show that the surface is still well approximately by a linear fit at this smaller scale-length. (d) Evolution of $B_{z,max}$ (black circles) within $\pm 1\mu$m of the line in (c) and the result of Eqn. 6.2 (black line) calculated along this line with $\langle u_y \rangle = 0.26c$ along with values calculated from a lineout at $y = 10$ μm. This again shows that the evolution is well approximated by the equations, however at late times the theory begins to over-estimate the maximum field strength.

0.25 μm] at $a_0 = 100$). For these simulations the early evolution of the fields can be accurately calculated using the same t_0 and changing the position x_f to the position where each simulated preplasma is truncated. However the field generation in the short scale-length simulations is similar to the rear-surface field generation where the fields form as a pulse as shown in Fig. 6.8.

6.4   Conclusions

Taken together, Eqns. 6.2, 6.3, and 6.4 provide a way to estimate the maximum B_z at some radial position y on the target surface at some time t during the expansion. This estimate can be made directly from laser parameters a_0 and pulse duration τ, therefore this equation set provides significant utility in estimating field strengths for future experiments on the next generation of lasers. Aside from the laser parameters, one must use assumed values for $\langle u_y \rangle$ which can be taken to be in the range of 0.2c to 0.1c for increasing a_0 from 50 to 500. Additionally R may be measured experimentally or calculated from the equations presented by Zhang *et al.* [93].

With the > 0.1 MT fields produced outside the focal volume, it may be possible to perform experiments studying magnetized processes, e.g. reconnection, shock formation, turbulence, in a regime that is relevant to the extreme plasma environments around relativistic compact objects such as neutron stars and black holes. For example, two ultra-intense lasers may be used in the standard 2-beam geometry [34] to study highly energetic laser-driven magnetic reconnection. The regime accessed by such an experiment can be parametrized using σ as discussed in Section 2.11. For $a_0 = 400$, $\sigma_{hot,e}$, the hot electron-only σ calculated in the co-moving frame of hot electron outflow from the focal volume is in the range of 0.1-0.5 along the surface of the target. This is quite large, allowing for semi-relativistic outflows from the reconnection region, giving the already ultra-relativistically hot electron inflow a modest amount of additional energy. With the production of such energetic conditions,

next generation laser facilities will be promising platforms for the study of the magnetized processes that occur in extreme astrophysical environments.

6.5   Measuring Extreme Magnetic Fields

In this chapter we have predicted that magnetic fields generated in laser-solid interactions on next generation laser facilities should exceed 0.1 MT. Measuring fields of this strength is nontrivial. Currently the main types of field measurement rely on optical or particle probing. Optical methods rely on the use of a diagnostic laser to probe the plasma. By probing the plasma with a laser, magnetic field information is encoded into the polarization of the laser through the Faraday effect [184]. Other experiments have used polarimetry of self-generated harmonics to estimate the range of field strengths [185]. Using an optical laser as a probe suffers from the inability to probe plasmas with densities greater than the critical density for the laser used. Most experiments will use a higher-order harmonic of the driving pulse to probe the plasma such that it can probe further into the dense plasma which would otherwise be inaccessible for the fundamental. Even with higher-order harmonics, at the standard wavelength of most high-powered laser facilities ($\sim 1\ \mu$m) the fields generated in laser-solid interactions cannot be probed. Faraday rotation using x-rays has been proposed as a solution [180], but a source of well characterized x-rays co-located with a high-intensity laser source cannot be easily found.

Protons are the most common particle used for probing magnetic fields. Features in the image are compared to simulation or simple models and synthetic radiographs as was done in Chapter 5. Quantitative measurements of path integrated electric and magnetic fields can be extracted from the relative deflections of protons in the image [63]. One of the main assumptions made in proton deflectometry analysis techniques is that the deflection angle due to fields is small compared to the initial angular spread of the protons passing through the fields, therefore the paths of deflected protons do not cross. If trajectories cross then a
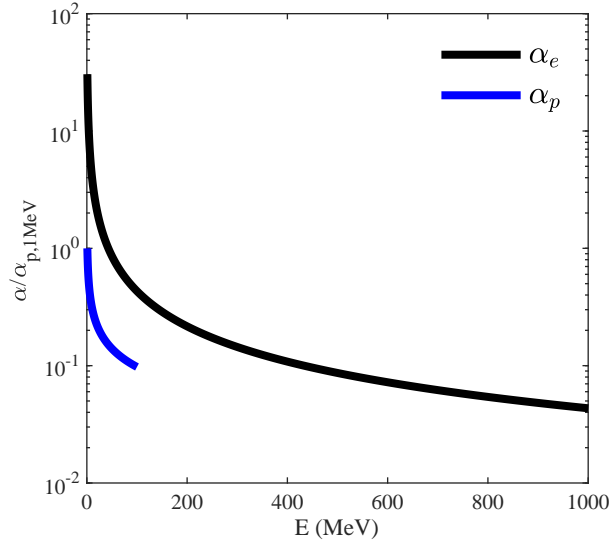
Figure 6.9: Comparison of electron and proton deflection angle in a magnetic field normalized to the deflection of a 1 MeV proton.

unique solution cannot be found when solving for the path integrated fields. To quantify the breakdown of this assumption the following parameter is used:

$$\mu \equiv l\alpha/a, \tag{6.5}$$

where l is the distance from the particle source to the object plane where the fields exist, α is the deflection angle, and a is the characteristic size of the fields. If $\mu > 1$ deflections are larger than the initial angle of particles probing the fields and quantitative analysis breaks down. TNSA protons used for radiography typically have energies are on the order of 10 MeV. At these energies deflection angles can be large in the $\sim$10 kT magnetic fields seen in relativistic laser-plasma interactions. For example, in Fig. 5.1 the front surface fields generated by the short pulse laser strongly focus the protons to a dot, therefore quantitative information about these fields cannot be extracted.

A possible solution is to use a different particle. A potential candidate is electrons accelerated by laser-wakefield acceleration (LWFA) [25]. Ion acceleration mechanisms are

inherently secondary to those of electrons, therefore electron acceleration is much more efficient. This allows electrons to reach much higher energies of ~ 8 GeV [186], compared to peak energies of ~ 100 MeV for protons [62]. To understand how this translates to particle deflectometry we can consider the relative deflection of particles. In Fig. 6.9 the deflections of electrons α_e and protons α_p in magnetic fields are normalized to the deflection of a 1 MeV proton. Although protons experience smaller deflections than electrons for the same energy, electrons can be produced at much higher energies allowing for smaller deflections. Electrons need to be produced with energies > 450 MeV to have a smaller deflection than a 100 MeV proton, which is routinely done.

LWFA electrons have previously been used to probe magnetic fields [71]. Many additional considerations must be made when using LWFA electrons to probe strong fields, some of which will be discussed here.

6.5.1 Divergence Angle

The first property to note is the divergence angle of electrons and protons. TNSA protons have large divergence angles > 30 degrees or 0.5 rad allowing them to probe the complete magnetic fields on the surface of a target with scales of a few mm and source to target distances of ~ 10 mm. LWFA electrons have much smaller divergence angles of only a few mrad [187] and therefore the source needs to be placed ~ 1 m from the target to capture the full picture of the target fields. If this difference in probing distances is taken into account, μ is much larger for electrons. To combat this issue Schumaker *et al.* placed a thin foil between the source and target to scatter the beam and increase the divergence angle [71]. This solution greatly reduces the resolution of the probe as the transverse emittance increases, hence the effective source size of the beam increases. A better solution could be to use beam optics which can increase the divergence angle of the beam without increasing the source size [188, 189].
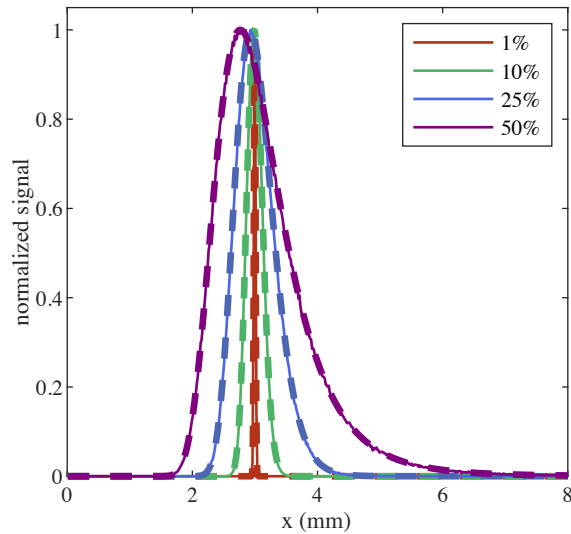
Figure 6.10: Spread in image plane of an electron beam calculated from a particle tracking code assuming deflections in a single plane (solid lines) and Eqn. 6.9 (dashed lines). The following parameters were used: $E_0 = 1$ GeV, $l = 1$ cm, $L = 1$ m, $\mathcal{B} = 0.01$ Tm, σ_E varied as shown in the legend. The particle tracking code and plot were created by Paul T. Campbell.

6.5.2 Energy Spread

Just as the source size of the beam can affect the resolution of the probe, the energy spread of the beam will also place an limit on the minimum feature size that can be resolved. For proton radiography using RCF the energy spread is generally not an issue because the spread of proton energies absorbed by a piece of RCF is very narrow. For relativistic electrons which will likely be detected by LANEX [190], all electron signal will be integrated. Deflection angle varies with particle energy, therefore features will be blurred due to the beam energy spread. If we assume that the particle energies are not changing during the propagation of the beam through the fields, and the beam is propagating along the z-direction with magnetic field in the y-direction, then the deflections are given by,

$$\alpha_x(x_0, E) = \frac{ec}{E + mc^2} \int_0^\infty B_y(x_0) \, dz_0, \tag{6.6}$$

which is derived from the ratio of v_x/v_z where $v_z \approx c$ and E is the relativistic kinetic energy. From Eqn. 6.6 we can see that particles of different energies will be deflected to different angles with the highest energy particles seeing the smallest deflection. For the purpose of finding a resolution criteria based on energy spread we need to know the width of this angular spread in the image plane.

If the electrons have a Gaussian energy distribution and propagate to the object plane from a point source, they will have a distribution at the object plane of,

$$\frac{\partial^2 N}{\partial x_0 \partial E} \propto \exp\left(-\frac{(E - E_0)^2}{2\sigma_E}\right). \tag{6.7}$$

At the object plane the electrons are deflected to a point in the image plane given by $x = x_0 + x_0 L/l + \alpha_x(x_0, E)L$. Rearranging this equation gives,

$$E = \frac{ecL}{x - Mx_0}\mathcal{B} - mc^2, \tag{6.8}$$

where $\mathcal{B} = \int_0^\infty B_y(x_0)\,dz_0$ and $M = (l + L)/l$ is the magnification. To find the distribution function in the image plane we multiply Eqn. 6.7 by $\partial E/\partial x$ and substitute Eqn. 6.8 for E. This gives the distribution function in the image plane,

$$\frac{\partial^2 N}{\partial x_0 \partial x} \propto \frac{-ecL\mathcal{B}}{(x - Mx_0)^2} \exp\left(-\frac{(\frac{ecL}{x-Mx_0}\mathcal{B} - mc^2 - E_0)^2}{2\sigma_E}\right). \tag{6.9}$$

This equation is only valid for a relativistic beam where $v_z \approx c$ and therefore only valid for small $x - Mx_0$ where Eqn. 6.8 is positive. A plot of this equation compared to results from a particle tracking code assuming deflections in a single plane is shown in Fig. 6.10. Particles are only deflected to one side of the position of a particle experiencing no deflection, i.e. $x = Mx_0$. If $\sigma_E \ll (E + mc^2)^2$ then the maximum of this distribution occurs at the position,

$$x_{max} = \frac{ecL\mathcal{B}}{E_0 + mc^2} + Mx_0. \tag{6.10}$$

The value of Eqn. 6.9 at this position is given by,

$$\frac{\partial^2 N(x_{max})}{\partial x_0 \partial x} = -\frac{(E_0 + mc^2)^2}{ecL\mathcal{B}}, \tag{6.11}$$

therefore Eqn. 6.9 can be normalized by this value to give a maximum of 1. This is simply the peak position of the exponential because the shape of the beam spread in the image plane is dominated by the exponential term for small energy spreads. We can therefore take the full-width half-maximum (FWHM) of the exponential to define a resolution criterion based on energy spread. This FWHM is given by,

$$\Delta x_{energy} = ecL\mathcal{B} \left(\frac{2\sqrt{2\ln(2)}\sigma_E}{(E_0 + mc^2)^2 - (2\ln(2)\sigma_E)^2} \right). \tag{6.12}$$

Similar to the Rayleigh resolution criterion we can note that only features with sizes greater than Δx_{energy} in the image plane will be resolved.

6.5.3   Temporal Blurring

If a highly relativistic electron beam is used to probe rapidly expanding fields on the surface of a flat target then there will be a difference in probing time between the center and edge of the target. If we consider a spherical front moving at c from a point source, the center of the front will reach target first. A ray on this front passing through the position x_0 in the object plane will arrive at a time Δt later given by,

$$\Delta t = \frac{\sqrt{l^2 + x_0^2} - l}{c}. \tag{6.13}$$

This blurring is therefore not constant and varies across the object plane as,

$$\frac{\partial \Delta t}{\partial x_0} = \frac{x_0}{c\sqrt{l^2 + x_0^2}}. \tag{6.14}$$

This is only a small correction and is especially small for $l \gg x_0$.

6.5.4   QED considerations

As high energy electrons of the probe beam are deflected by the strong fields on the target surface they will generate photons. By emitting photons the electron beam gives up energy thereby shifting the mean energy of the beam and causing the energy spread of the beam to increase. These effects are given by the equations [91],

$$\left(\frac{d\langle \mathbf{p} \rangle}{dt} \right)_{mod\ cl} = -\frac{\langle gP_{cl}\hat{\mathbf{p}} \rangle}{c}, \tag{6.15}$$

$$\left(\frac{d\sigma^2}{dt} \right)_{st} = -2\frac{\langle \Delta\gamma gP_{cl} \rangle}{m_e c^2} + \frac{\langle S \rangle}{m_e^2 c^4}, \tag{6.16}$$

$$S(\eta) = \frac{55\alpha_f c}{24\sqrt{3}\lambda_c b} m_e^2 c^4 \eta^4 g_2(\eta), \tag{6.17}$$

where Eqn. 6.15 gives the change in expectation value of the momentum and Eqn. 6.16 gives the change in the variance of a beam with $\sigma^2 = \langle \gamma^2 \rangle - \langle \gamma \rangle^2$ and $\Delta\gamma = \gamma - \langle \gamma \rangle$. P_{cl} is the classical power emission to synchrotron radiation given by,

$$P_{cl} = \frac{2\alpha_f c}{3\lambda_c} m_e c^2 \eta^2, \tag{6.18}$$

where α_f is the fine structure constant, and η is the quantum efficiency parameter defined as the ratio of the field strength in the rest frame of the electron beam to the Schwinger field $E_s = 1.38 \times 10^{18}$ Vm^{-1}. For a highly relativistic beam where $\gamma \gg 1$, $\eta \approx \gamma b = \gamma |\mathbf{E}_\perp + \mathbf{v} \times \mathbf{B}|/E_s$. The Gaunt factor $g(\eta)$ acts as a quantum correction to the classical emission spectrum for large η and has been fit to $g(\eta) \approx [1+4.8(1+\eta)\ln(1+1.7\eta)+2.44\eta^2]^{-2/3}$. The factor $g_2(\eta)$ also has been fit to a function given by, $g_2(\eta) \approx [1 + (1 + 4.528\eta)\ln(1 + 12.29\eta)+4.632\eta^2]^{-7/6}$. These equations were given in Section 2.8 and have been written here for convenience.

If we consider an electron beam with a Gaussian energy spread propagating through a constant magnetic field that is perpendicular to the propagation direction we can solve analytically for the decay in the expectation value of the momentum using Eqn. 6.15,

$$\langle \mathbf{p} \rangle \approx \left(\frac{1}{\langle \mathbf{p_0} \rangle} + \mu t \right)^{-1}, \tag{6.19}$$

$$\mu = \frac{2\alpha_f c^2 B_\perp^2}{3\lambda_c m_e E_s^2}, \tag{6.20}$$

where $\langle \mathbf{p_0} \rangle$ is the moment of the initial momentum. Here we have assumed $\eta \ll 1$ so $g \approx 1$, and additionally $\sigma^2 m_e^2 c^2 \ll \langle \mathbf{p} \rangle^2$. This can be rearranged to solve for the perpendicular magnetic field,

$$B_\perp = \sqrt{ \frac{3\lambda_c m_e E_s^2}{2\alpha_f c l_B} \left(\frac{1}{\langle p \rangle} - \frac{1}{\langle p_0 \rangle} \right) }, \tag{6.21}$$

where $l_B = ct$ is the length of the magnetic field assuming highly relativistic electrons. Eqn. 6.19 can be substituted into Eqn. 6.16 assuming $\langle \mathbf{p} \rangle = m_e c \langle \gamma \rangle$,

$$\sigma = \langle \gamma \rangle^2 \sqrt{ \frac{\sigma_0^2}{\langle \gamma_0 \rangle^4} + At }, \tag{6.22}$$

where $A = \alpha_f c^4 B_\perp^3 55 / 24 E_s^3 \sqrt{3} \lambda_c$. We can note an interesting result here. If the initial and final mean γ and energy spread can be measured then Eqn. 6.19 will give $B_\perp^2 l_B$ while Eqn. 6.22 will give $B_\perp^3 l_B$. Additionally if the deflected image can be inverted the solution will give $B_\perp l_B$, therefore if at least two of the three measurements can be made then $B_\perp$ and l_B can be found uniquely.

If η is not $\ll 1$, then g will not be constant and cannot be removed from the integrals solved to get Eqns. 6.19 and 6.22. An analytical solution can be found by Taylor expanding g, however it is not simple to manipulate the solutions to obtain $B_\perp$. If necessary, the best option may be to solve Eqns. 6.15 and 6.16 numerically to fit experimental data.

To determine whether this technique is viable in experiments I have been working with

Jason Cardarelli [191]. He has written a particle tracking code for electron spectrometers that will allow us to estimate the error in measurements of σ and $\langle \gamma \rangle$, and therefore the error in the calculated $B_\perp$ and l_B. This work is ongoing.

It is possible that even with extremely energetic multi-GeV LWFA electron beams, magnetic fields may be so strong that $\mu > 1$. In this case, the mean energy and energy spread of the beam may be used to determine the field strengths, however it may also be possible to estimate field strengths at specific points on the target using a small divergence electron beam, looking at the profile of the deflected beam. If the initial energy spread and mean energy of the beam is known, then either Eqn. 6.10 or 6.12 may be used to determine the path integrated magnetic field from the shift in the position of maximum flux and FWHM in the image plane respectively. To do this, the change in energy spread from radiation reaction may also need to be accounted for. Using this concept in the initial magnetic field measurement experiments on the next generation of laser facilities may be a good idea as it removes the complexity of beam optics and can give rough estimates of the field strengths.

CHAPTER 7

Conclusions and Future Work

This thesis studied two of the most fundamental phenomena in our universe, shock formation and magnetic field generation, over a large range of energetic regimes. The work focused on laser-driven shocks with multiple ion species, semi-relativistic magnetized shock formation, magnetic field generation at strong-field QED relevant laser intensities and the measurement of these fields. These sections will be summarized in this chapter and future diections for each topic will be discussed.

7.1 Multiple Species Ion Shock Acceleration

In Chapter 4 PIC simulations were performed and theory was developed to study the formation of shocks in a plasma with multiple ion species. This differs from the majority of shock theory which has been performed only accounting for a single ion species. However, it is more realistic as shocks in experiments and those that develop throughout the universe generally include multiple ion species or at least multiple ionization states. It was shown that the basic equations commonly used to model collisionless shocks break down when a second ion species is included. This occurs because ions are generally modeled as a fluid, however reflections which become important to the dynamics of high Mach number multi-species shock require a kinetic description.

Parameter scans were performed to study how density ratios across the shock, relative ion fraction and ionization state affect the shock dynamics. It was found that as the density

ratio increased a proton shock was generated and as the ratio was further increased double shocks could form. This double shock is not predicted by standard shock theory which breaks down after the first shock forms. The second shock is allowed to form as protons are reflected by the primary shock, creating a shock upstream that is dominated by the lower charge-to-mass ratio ion. The formation of a double shock allows for multiple stages of acceleration as ions reflected to sufficient energies can propagate from the primary shock downstream to upstream, gaining energy.

Simulations were also performed using lasers to drive the shock. Using the "ideal" density profile defined by Fiuza *et al.* [96], only a single shock that reflects protons was produced. A double shock could be formed using a modified density profile with a stepped profile, effectively increasing the density steepening. This suggests that density steepening and the resulting separation of ion species that occurs near the steepened density is required to drive a double shock. In general, the addition of a second ion species reduced the maximum energy of the accelerated high charge-to-mass ratio ion.

These results demonstrate the need for improvement in both the theoretical models and experiments performed on laser-driven collisionless shocks. One potential model to build from is that of Malkov *et al.* [99] which includes ion reflections. Additionally, the simulations that were performed assumed complete ionization of the plasma and the existence of at most two ion species. In experiment, it is possible that multiple ionization states may exist during shock formation which could greatly affect the acceleration of ions and the number of shocks that form. The simulations reported here were performed in 2D with infinite focal spots, however 3D effects including instability formation from realistic laser focusing may greatly affect shock formation. Due to the massive parameter space (target material, laser energy, target density profile, etc.) that must be studied to optimize and fully understand ion shock acceleration there is still a significant amount of work to do. Simulations are currently the best tool for rigorously understanding collisionless shock physics as the amount of experimental data studying this acceleration is quite limited. Next-generation high-energy

high rep-rate laser facilties may allow for significant progress in this field as parameters can be rapidly explored. Additionally, new target fabrication techniques may allow for tailored density profiles that can be optimized to provide more favorable acceleration conditions for generating high energy, narrow energy spread proton beams.

7.2 Semi-Relativistic Magnetized Shock Formation in the Laboratory

In Chapter 5 an experiment studying semi-relativistic magnetized shocks and a massive 3D particle-in-cell simulation performed to support this experiment were presented. The experiment was performed on the OMEGA EP laser system at the University of Rochester Laboratory for Laser Energetics. This is a massive laser facility with the capability to run experiments involving multiple high-energy and high-intensity laser pulses. We used two lasers to drive a highly asymmetric interaction between a long-pulse ns duration laser and a relativistic intensity short pulse ps duration laser. The interaction was probed using protons to generate images of the fields in the interaction.

The resultant proton images showed the expansion of strong magnetic fields from the short-pulse focal spot and the interaction of these fields with the quasi-static fields of the long-pulse generated plasma plume. The fields expanding from the short pulse focal spot propagate out at speeds of 0.1-0.6c, and are therefore carried by semi-relativistic electrons. At the point of interaction between the fields of the two laser-generated plasma plumes, a cone-like feature was observed. Forward modeling was used to construct synthetic proton images. This modeling showed that the cone-like feature cannot be generated by a simple superposition of the fields and must correspond to an additional modification to the fields. Proton deflectometry only allows for the measurement of path-integrated fields, therefore it cannot find a unique solution to the feature, however possible solutions are the annihilation of fields, or the build up of short-pulse generated magnetic fields in the region of the long-pulse

plume magnetic fields.

A massive 3D particle-in-cell simulation was run to understand the features observed in the experiment and to obtain insight into what features may not be captured by the diagnostics. This simulation was performed at 25x reduced scale and the fields and density profile of the long-pulse generated plasma plume were imported as initial conditions based on fits to simulation data from the extended-MHD code GORGON. Even with these simplifications the simulation still required >50000 cores and $\sim$ 2.5 million core hours. The resultant simulation data provided a wealth of information about the interaction between the laser-gererated plasma plumes. It was found the the electrons rapidly expand carrying strong magnetic fields $\sim$ 3kT. These electrons do not simply pass through the long-pulse generated plasma plume, instead they are diverted around the plume, forming a discontinuity. The long-pulse side of the discontinuity rapidly compresses and is followed by the formation of a shock. A large shear is setup at the discontinuity between the semi-relativistic electrons accelerated by the short-pulse and a return current formed on the long-pulse side of the discontinuity. This shear becomes unstable forming vortices and unstable wave-like structures. 2D simulations were performed to understand these instabilies which showed that some features are likely formed by the electron-scale Kelvin-Helmholtz instability and others may be generated by the lower-hybrid drift or the modified two stream instability. These features are too small and fast to be captured by proton deflectometry. The main cone feature that is seen in the experimental data is likely due to the draping and build-up of magnetic field at the contact discontinuity.

From the setup for this experiment one can note that it is similar to the standard two-beam magnetic reconnection geometry, and this was in fact the initial motivation for this experiment. The cone feature observed in the experiment could be a signature that a highly-asymmetric reconnection occurred, however diagnosing this potential reconnection in experiment and simulation is non-trivial. In the simulation, signatures of reconnection are observed: interaction of oppositely directed fields with associated Hall-type quadrupolar

magnetic fields, electron outflows and a current-sheet normal electric field. However these features could also be generated by the complex interaction at the contact discontinuity. The electron outflows can be caused by the electrons draping around the curved interface of the long-pulse generated plume. The quadrupolar fields can be caused by the electrons bending the field lines as they form a shear at the contact discontinuity. The electric field normal to the current sheet is generally used to calculate the reconnection rate, however target normal electric fields already exist due to charge separation and complex fields are generated by instabilities near the current sheet, making it very difficult to extract a reconnection rate. If reconnection does occur in the experiment due to the complex filaments and vortices it is likely that reconnection would not form as a single x-point. Additionally the reconnection would be driven primarily by electrons and would be highly asymmetric.

The observed features in the experiment and those that cannot be resolved but are predicted by the simulation create the potential for numerous future experiments. By using alternative diagnostics, e.g. 4ω-probe or some alternative probing geometry one may be able to observe some of the faster unstable features or obtain measurements of the shock and contact discontinuity. We can also envision modifying the experiment to isolate or change the properties of some of the features such that they can be more easily probed and studied in greater detail. The observation of highly asymmetric relativistic reconnection would also be very interesting as it has only been studied theoretically [192], however the experiment will need to be carefully designed such that there is clear evidence of reconnection.

7.3 Magnetic Field Generation at Extreme Laser Intensities

In Chapter 6 the generation of magnetic fields in solid target interactions with laser intensities where strong-field QED processes become important was studied. This was done through a series of 2D simulations using the QED module of the particle-in-cell code OSIRIS which

includes the dominant processes of nonlinear Compton emission and pair creation. Simulations were performed from $a_0 = 50$ to 500, covering a large range of intensities from what can be currently achieved to intensities just greater than what may be achieved by next-generation laser facilities. Studying field generation in this range of intensities is important as the possible magnetic field strengths that may be reached by next-generation facilities is currently not well understood. It is expected that QED effects will become important at these extreme intensities and may limit the energy available for field generation.

The fields on the surface of the target form rapidly as electrons are accelerated radially by the laser field. The laser pulse channels through to the relativistic critical density before it begins to hole bore and reflect. This sets up a standing wave that interacts with hot electrons in the channel forming the conditions for energetic photon production. The electrons are accelerated from the focal volume in all directions, however target normal electric fields confine the majority of the electrons to travel near the surface of the target. These target normal fields are setup by the outward propagating electrons and the return current they drive that causes a depletion of the target electrons and therefore a net positive charge along the target surface. The outward moving current is what drives the strong $\mathcal{O}(0.1\ \mathrm{MT})$ magnetic fields. These fields are canceled within the target by the return current.

The magnetic field scaling with laser intensity was extracted by taking an average of the maximum magnetic fields along the surface of the target. It was found that the maximum fields scale non-linearly with a_0, scaling closer to $\sqrt{a_0}$. Additional simulation were run without radiation reaction and pair creation at $a_0 = 400$ and 500 which showed an increase in magnetic field strength. The reason for this was elucidated through the energy budgets of the simulations. As a_0 increases, more of the energy is converted from electron kinetic energy to photons, almost 40% at $a_0 = 500$. Although many of these photons are produced with large energies $> 2m_e c^2$, very few electron-positron pairs are produced.

The evolution of these fields and the scaling with a_0 was modeled using a simple analytic model. Starting from the equation of Schumaker *et al.* [71] additional equations were derived

allowing for the estimation of field strength starting from laser parameters. This involves approximating the target surface as an approximately linear channel that unfolds at the speed of light. This model is quite accurate and can predict both the scaling of the fields with a_0 and how the maximum field strength evolves in time along the surface. The equations were tested for a few pre-plasma scale-lengths which showed good agreement during early times, however at late times in the evolution the model overestimated the field strength for the shortest scale-lengths. This is due to the fields appearing as a pulse that propagates away from the laser focal spot, causing the fields at a particular position on the front surface of the target to decrease at late times. The model is also only accurate outside the focal volume where ion motion is negligible. However these fields are the most important for magnetized experiments like those in the two-beam reconnection geometry. This model is therefore a fundamentally useful tool for the proposal of any future magnetized experiment using these target surface fields. However, it is important to note that the model was based on the results of 2D simulations. In 3D it is likely that the heating and expansion of electrons from the focal volume will be different, resulting in an average radially velocity that differs from the values found in 2D. Additionally, instabilities may form causing a non-uniform radial expansion of the fields. This was observed in Chapter 5 as a set of spoke-like features in the proton images.

Finally, in this chapter we briefly considered how these fields may be measured. It was shown that quantitative proton deflectometry techniques breakdown as the probing becomes highly nonlinear at currently available proton energies. A possible solution is to use laser wakefield accelerated electrons. Although these particles have a much larger charge-to-mass ratio they can be produced at much higher energies with narrow energy spreads [186]. Using electrons as a probe brings about many other classical considerations including the beam divergence, the detection method, and energy spread. Additionally, by probing such strong fields the probe beam may experience QED effects. It was shown that the mean energy of the beam will decrease and the energy spread will increase when passing through
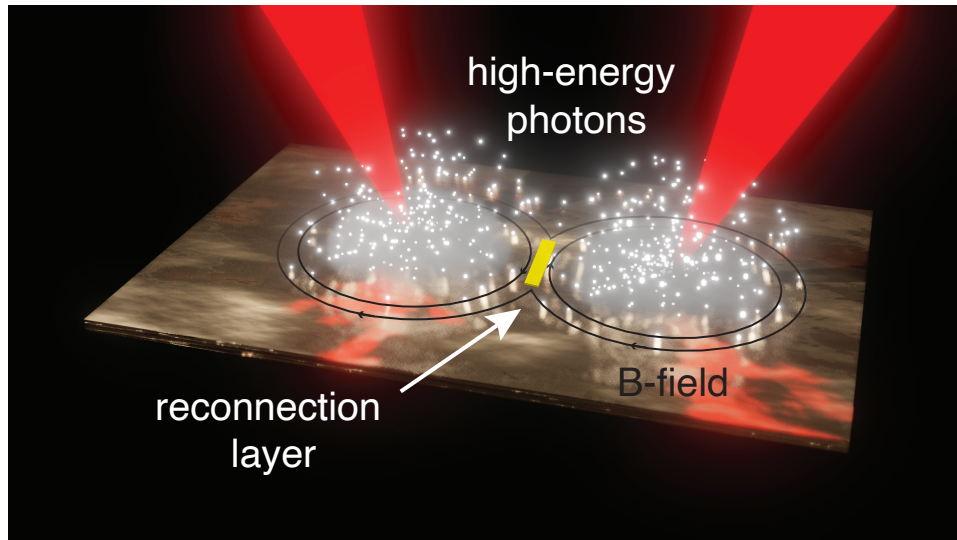
Figure 7.1: Concept for radiative reconnection using two ultra-intense lasers.

the fields due to radiation reaction. Assuming constant magnetic fields and relatively small nonlinearity, analytic expressions for the mean energy and energy spread of the probe electron beam can be derived which shows a different scaling with the length and magnitude of the fields. Magnetic field strength and length can be solved for with this method, compared to deflectometry that can only solve for the path integrated fields. Determining whether this method is experimentally feasible is a work in progress.

7.4 Perspective

This thesis is being written at a very interesting time in the development of laser-plasma physics. In the time that I have been a graduate student several major changes have taken place. New multi-petawatt laser facilities are under development in Europe (ELI [193], Apollon [194]) and Asia (SULF [195], Corels [196]). In response, LasernetUS was formed allowing for scientists to propose experiments at the many mid-scale terawatt and petawatt class facilities throughout North America. Additionally, this coalition created a unified voice to advocate to the United States government for laser facilities that could compete with those

elsewhere in the world and provide the greatest opportunity for progress in plasma physics research [197,198]. A direct or indirect byproduct of this is the recent funding of ZEUS at the University of Michigan [30], MTW-OPAL at the University of Rochester [199], and a multi-petawatt facility at the Stanford Linear Accelerator National Laboratory (SLAC) [200]. These facilities are expected to achieve intensities $> 10^{23}$ W/cm^2. At these intensities it is expected that QED effects will become important as demonstrated in Chapter 6. In the context of the work in this thesis this brings about the question: what should future experimental and theoretical efforts at these laser facilities focus on?

From the current state of laboratory astrophysics research there appears to be two logical frontiers for progress to be made on: rigorous studies of microphysics (e.g. reconnection, instabilities, etc.) using high rep-rate lasers, and studying the highest energy interactions possible. For the former frontier we must first consider consider the current state of high-energy experiments studying collisionless shocks or magnetic fields. These experiments are generally performed on large-scale facilities such as OMEGA or NIF. Time on these facilities is very limited, for example one may only get a couple shot days a year on OMEGA EP with ~ 7 shots being taken on an average day. This limitation greatly restricts the amount of parameter space that can be sampled. It also makes it very difficult to measure processes that are not the dominant effect in a system. This has been a serious limiting factor in the progress of laser-driven magnetic reconnection as signatures of electron acceleration by reconnection are lost in the background of dominant laser accelerated electrons. Given enough data this laser background could be understood and subtracted to see the effects of reconnection.

With the number of shots taken currently and the limited diagnostics it is also highly non-trivial to analyze data. Looking at the work in Chapter 5 the small number of shots, and having proton deflectometry as the only diagnostic, placed a significant burden on simulations to provide insight into the interaction. Additionally, the ambiguity of what fields cause the deflections makes it very difficult to analyze data as features must be interpreted, opening

analysis up to potential error due to biases. High rep-rate systems will provide more rigorous studies that require less interpretation. These experiments must also be well diagnosed, potentially requiring the development of new diagnostics. With the generation of large datasets from these diagnostics it is likely that machine learning will be applied, allowing for more sophisticated models to be produced. The application of high rep-rate lasers to laboratory astrophysics should greatly increase the accuracy of experiments and allow for a shift in the experimental paradigm from experiments with small data sets demonstrating signatures of interesting physics, to rigorous large dataset experiments where these signatures are well understood.

Although a significant amount of effort should be put into rigorously studying the regimes that can already be accessed by current laser systems, we must also explore the highest intensity interactions possible to access new physics regimes. In Chapter 6 we showed that at the upper end of expected intensities, magnetic fields should exceed 0.1 MT and a significant fraction of energy will be converted to photons with enough energy to create pairs. Additionally, in Chapter 5 we showed that semi-relativistic shocks can already be studied at current available laser intensities. A simple combination of these two ideas suggests that we may be able to achieve relativistic magnetized shocks where radiation reaction and QED effects become important. In addition, with the combination of two ultra intense laser pulses it is possible that radiative reconnection may be studied (Fig. 7.1). Although likely not a perfect analog for the environments theorized in extreme astrophysics, experiments studying these processes will give insight into physics that can only be studied in idealized simulations currently. Achieving these experiments will not be trivial and will likely require the development of new diagnostics that can probe the extreme conditions and measure the emitted radiation. As shown in Chapter 6 it is possible that radiation reaction may be leveraged to create new diagnostics. These experiments will likely exist in the current small data set paradigm and will require huge simulations to gain insight into the physics of the interaction. Even without QED effects, such simulations are computationally intensive as demonstrated

in Chapter 5, therefore QED effects must be implemented in a very efficient way in future particle-in-cell codes.

BIBLIOGRAPHY

[1] *Tycho's Supernova Remnant*, https://chandra.harvard.edu/photo/2005/tycho/.

[2] P. Zhang, S. S. Bulanov, D. Seipt, A. V. Arefiev, and A. G. R. Thomas, *Relativistic plasma physics in supercritical fields*, Physics of Plasmas **27**, 050601 (2020).

[3] M. J. Starkey, M. A. Dayeh, S. A. Fuselier, S. M. Petrinec, D. J. McComas, K. Ogasawara, J. R. Szalay, and N. A. Schwadron, *Determining the Near-Instantaneous Curvature of Earth's Bow Shock Using Simultaneous IBEX and MMS Observations*, Journal of Geophysical Research: Space Physics **127**, e2021JA030036 (2022).

[4] K. Heng, R. McCray, S. A. Zhekov, P. M. Challis, R. A. Chevalier, A. P. S. Crotts, C. Fransson, P. Garnavich, R. P. Kirshner, S. S. Lawrence, P. Lundqvist, N. Panagia, C. S. J. Pun, N. Smith, J. Sollerman, and L. Wang, *Evolution of the Reverse Shock Emission from SNR 1987A*, The Astrophysical Journal **644**, 959–970 (2006).

[5] Vogt, Frédéric P. A., Seitenzahl, Ivo R., Dopita, Michael A., and Ghavamian, Parviz, *[FeXIV] and [FeXI] reveal the forward shock in SNR 1E0102.2-7219*, Astronomy & Astrophysics **602**, L4 (2017).

[6] M. V. Barkov, M. Lyutikov, and D. Khangulyan, *3D dynamics and morphology of bow-shock pulsar wind nebulae*, Monthly Notices of the Royal Astronomical Society **484**, 4760–4784 (2019).

[7] H. Madanian, M. I. Desai, S. J. Schwartz, L. B. Wilson, S. A. Fuselier, J. L. Burch, O. L. Contel, D. L. Turner, K. Ogasawara, A. L. Brosius, C. T. Russell, R. E. Ergun, N. Ahmadi, D. J. Gershman, and P.-A. Lindqvist, *The Dynamics of a High Mach Number Quasi-perpendicular Shock: MMS Observations*, The Astrophysical Journal **908**, 40 (2021).

[8] A. M. Bykov, E. Amato, A. E. Petrov, A. M. Krassilchtchikov, and K. P. Levenfish, *Pulsar Wind Nebulae with Bow Shocks: Non-thermal Radiation and Cosmic Ray Leptons*, Space Science Reviews **207**, 235–290 (2017).

[9] L. Sironi, U. Keshet, and M. Lemoine, *Relativistic Shocks: Particle Acceleration and Magnetization*, Space Science Reviews **191**, 519–544 (2015).

[10] F. Fiuza, R. A. Fonseca, J. Tonge, W. B. Mori, and L. O. Silva, *Weibel-Instability-Mediated Collisionless Shocks in the Laboratory with Ultraintense Lasers*, Physical Review Letters **108**, 235004 (2012).

[11] A. Kandus, K. E. Kunze, and C. G. Tsagas, *Primordial magnetogenesis*, Physics Reports **505**, 1–58 (2011).

[12] A. Brandenburg and K. Subramanian, *Astrophysical magnetic fields and nonlinear dynamo theory*, Physics Reports **417**, 1–209 (2005).

[13] R. Schlickeiser and P. K. Shukla, *Cosmological Magnetic Field Generation by the Weibel Instability*, The Astrophysical Journal **599**, L57–L60 (2003).

[14] L. Biermann and A. Schlüter, *Cosmic Radiation and Cosmic Magnetic Fields. II. Origin of Cosmic Magnetic Fields*, Physical Review **82**, 863–868 (1951).

[15] R. P. Drake, *High Energy Density Physics: Fundamentals, Inertial Fusion and Experimental Astrophysics*, Springer International Publishing, Berlin (2018).

[16] D. Haberberger, S. Tochitsky, F. Fiuza, C. Gong, R. A. Fonseca, L. O. Silva, W. B. Mori, and C. Joshi, *Collisionless shocks in laser-produced plasma generate monoenergetic high-energy proton beams*, Nature Physics **8**, 95 – 99 (2011).

[17] H. G. Rinderknecht, M. J. Rosenberg, C. K. Li, N. M. Hoffman, G. Kagan, A. B. Zylstra, H. Sio, J. A. Frenje, M. Gatu Johnson, F. H. Séguin, R. D. Petrasso, P. Amendt, C. Bellei, S. Wilks, J. Delettrez, V. Y. Glebov, C. Stoeckl, T. C. Sangster, D. D. Meyerhofer, and A. Nikroo, *Ion Thermal Decoupling and Species Separation in Shock-Driven Implosions*, Physical Review Letters **114**, 025001 (2015).

[18] P. T. Campbell, C. A. Walsh, B. K. Russell, J. P. Chittenden, A. Crilly, G. Fiksel, P. M. Nilson, A. G. R. Thomas, K. Krushelnick, and L. Willingale, *Magnetic Signatures of Radiation-Driven Double Ablation Fronts*, Physical Review Letters **125**, 145001 (2020).

[19] L. Gao, P. M. Nilson, I. V. Igumenshchev, M. G. Haines, D. H. Froula, R. Betti, and D. D. Meyerhofer, *Precision Mapping of Laser-Driven Magnetic Fields and Their Evolution in High-Energy-Density Plasmas*, Physical Review Letters **114**, 215003 (2015).

[20] G. Sarri, A. Macchi, C. A. Cecchetti, S. Kar, T. V. Liseykina, X. H. Yang, M. E. Dieckmann, J. Fuchs, M. Galimberti, L. A. Gizzi, R. Jung, I. Kourakis, J. Osterholz, F. Pegoraro, A. P. L. Robinson, L. Romagnani, O. Willi, and M. Borghesi, *Dynamics of Self-Generated, Large Amplitude Magnetic Fields Following High-Intensity Laser Matter Interaction*, Physical Review Letters **109**, 205002 (2012).

[21] L. J. Perkins, R. Betti, K. N. LaFortune, and W. H. Williams, *Shock Ignition: A New Approach to High Gain Inertial Confinement Fusion on the National Ignition Facility*, Physical Review Letters **103**, 045004 (2009).

[22] D. A. Uzdensky, *Magnetic Reconnection in Extreme Astrophysical Environments*, Space Science Reviews **160**, 45–71 (2011).

[23] D. Strickland and G. Mourou, *Compression of amplified chirped optical pulses*, Optics Communications **55**, 447–449 (1985).

[24] T. Tajima and J. M. Dawson, *Laser electron accelerator*, Physical Review Letters **43** (1979).

[25] S. P. D. Mangles, C. D. Murphy, Z. Najmudin, A. G. R. Thomas, J. L. Collier, A. E. Dangor, E. J. Divall, P. S. Foster, J. G. Gallacher, C. J. Hooker, D. A. Jaroszynski, A. J. Langley, W. B. Mori, P. A. Norreys, F. S. Tsung, R. Viskup, B. R. Walton, and K. Krushelnick, *Monoenergetic beams of relativistic electrons from intense laser-plasma interactoins*, Nature **431**, 535–538 (2004).

[26] P. Kaw and J. Dawson, *Relativistic Nonlinear Propagation of Laser Beams in Cold Overdense Plasmas*, The Physics of Fluids **13**, 472–481 (1970).

[27] B. Gonzalez-Izquierdo, R. J. Gray, M. King, R. J. Dance, R. Wilson, J. McCreadie, N. M. H. Butler, R. Capdessus, S. Hawkes, J. S. Green, M. Borghesi, D. Neely, and P. McKenna, *Optically controlled dense current structures driven by relativistic plasma aperture-induced diffraction*, Nature Physics **12**, 505–512 (2016).

[28] M. Vranic, T. Grismayer, R. A. Fonseca, and L. O. Silva, *Electron–positron cascades in multiple-laser optical traps*, Plasma Physics and Controlled Fusion **59**, 014040 (2016).

[29] T. G. Blackburn, C. P. Ridgers, J. G. Kirk, and A. R. Bell, *Quantum Radiation Reaction in Laser–Electron-Beam Collisions*, Physical Review Letters **112**, 015001 (2014).

[30] J. Nees, A. Maksimchuk, G. Kalinchenko, B. Hou, Y. Ma, P. Campbell, A. McKelvey, L. Willingale, I. Jovanovic, C. Kuranz, A. Thomas, and K. Krushelnick, *ZEUS: A National Science Foundation Mid-Scale Facility for Laser-Driven Science in the QED Regime*, in *2020 Conference on Lasers and Electro-Optics (CLEO)*, 1–2 (2020).

[31] D. D. Ryutov, R. P. Drake, and B. A. Remington, *Criteria for Scaled Laboratory Simulations of Astrophysical MHD Phenomena*, The Astrophysical Journal Supplement Series **127**, 465–468 (2000).

[32] M. Yamada, H. Ji, S. Hsu, T. Carter, R. Kulsrud, N. Bretz, F. Jobes, Y. Ono, and F. Perkins, *Study of driven magnetic reconnection in a laboratory plasma*, Physics of Plasmas **4**, 1936–1944 (1997).

[33] W. Gekelman, T. De Haas, W. Daughton, B. Van Compernolle, T. Intrator, and S. Vincena, *Pulsating Magnetic Reconnection Driven by Three-Dimensional Flux-Rope Interactions*, Physical Review Letters **116**, 235101 (2016).

[34] P. M. Nilson, L. Willingale, M. C. Kaluza, C. Kamperidis, S. Minardi, M. S. Wei, P. Fernandes, M. Notley, S. Bandyopadhyay, M. Sherlock, R. J. Kingham, M. Tatarakis, Z. Najmudin, W. Rozmus, R. G. Evans, M. G. Haines, A. E. Dangor, and K. Krushelnick, *Magnetic Reconnection and Plasma Dynamics in Two-Beam Laser-Solid Interactions*, Physical Review Letters **97**, 255001 (2006).

[35] F. Fiuza, G. F. Swadling, A. Grassi, H. G. Rinderknecht, D. P. Higginson, D. D. Ryutov, C. Bruulsema, R. P. Drake, S. Funk, S. Glenzer, G. Gregori, C. K. Li, B. B. Pollock, B. A. Remington, J. S. Ross, W. Rozmus, Y. Sakawa, A. Spitkovsky, S. Wilks, and H. S. Park, *Electron acceleration in laboratory-produced turbulent collisionless shocks*, Nature Physics **16**, 916–920 (2020).

[36] D. Kraus, J. Vorberger, A. Pak, N. J. Hartley, L. B. Fletcher, S. Frydrych, E. Galtier, E. J. Gamboa, D. O. Gericke, S. H. Glenzer, E. Granados, M. J. MacDonald, A. J. MacKinnon, E. E. McBride, I. Nam, P. Neumayer, M. Roth, A. M. Saunders, A. K. Schuster, P. Sun, T. van Driel, T. Döppner, and R. W. Falcone, *Formation of diamonds in laser-compressed hydrocarbons at planetary interior conditions*, Nature Astronomy **1**, 606–611 (2017).

[37] F. Suzuki-Vidal, S. V. Lebedev, A. Ciardi, L. A. Pickworth, R. Rodriguez, J. M. Gil, G. Espinosa, P. Hartigan, G. F. Swadling, J. Skidmore, G. N. Hall, M. Bennett, S. N. Bland, G. Burdiak, P. de Grouchy, J. Music, L. Suttle, E. Hansen, and A. Frank, *Bow shock fragmentation driven by a thermal instability in laboratory astrophysics experiments*, The Astrophysical Journal **815**, 96 (2015).

[38] J. E. Bailey, T. Nagayama, G. P. Loisel, G. A. Rochau, C. Blancard, J. Colgan, P. Cosse, G. Faussurier, C. J. Fontes, F. Gilleron, I. Golovkin, S. B. Hansen, C. A. Iglesias, D. P. Kilcrease, J. J. MacFarlane, R. C. Mancini, S. N. Nahar, C. Orban, J. C. Pain, A. K. Pradhan, M. Sherrill, and B. G. Wilson, *A higher-than-predicted measurement of iron opacity at solar interior temperatures*, Nature **517**, 56–59 (2015).

[39] A. E. Raymond, C. F. Dong, A. McKelvey, C. Zulick, N. Alexander, A. Bhattacharjee, P. T. Campbell, H. Chen, V. Chvykov, E. Del Rio, P. Fitzsimmons, W. Fox, B. Hou, A. Maksimchuk, C. Mileham, J. Nees, P. M. Nilson, C. Stoeckl, A. G. R. Thomas, M. S. Wei, V. Yanovsky, K. Krushelnick, and L. Willingale, *Relativistic-electron-driven magnetic reconnection in the laboratory*, Physical Review E **98**, 043207 (2018).

[40] K. F. F. Law, Y. Abe, A. Morace, Y. Arikawa, S. Sakata, S. Lee, K. Matsuo, H. Morita, Y. Ochiai, C. Liu, A. Yogo, K. Okamoto, D. Golovin, M. Ehret, T. Ozaki, M. Nakai, Y. Sentoku, J. J. Santos, E. d'Humières, P. Korneev, and S. Fujioka, *Relativistic magnetic reconnection in laser laboratory for testing an emission mechanism of hard-state black hole system*, Physical Review E **102**, 033202 (2020).

[41] J. Slavin and R. E. Holzer, *Solar wind flow about the terrestrial plantes 1. modeling bow shock position and shape*, Journal of geophysical research **86**, 11401–11418 (1981).

[42] S. P. Reynolds, B. M. Gaensler, and F. Bocchino, *Magnetic Fields in Supernova Remnants and Pulsar-Wind Nebulae*, Space Science Reviews **166**, 231–261 (2012).

[43] C. Badenes, K. J. Borkowski, J. P. Hughes, U. Hwang, and E. Bravo, *Constraints on the Physics of Type Ia Supernovae from the X-Ray Spectrum of the Tycho Supernova Remnant*, The Astrophysical Journal **645**, 1373–1391 (2006).

[44] I. I. Roussev, T. I. Gombosi, I. V. Sokolov, M. Velli, W. M. IV, D. L. DeZeeuw, P. Liewer, G. Tth, and J. Luhmann, *A Three-dimensional Model of the Solar Wind Incorporating Solar Magnetogram Observations*, The Astrophysical Journal **595**, L57–L61 (2003).

[45] K. Wilhelm, *Solar coronal-hole plasma densities and temperatures*, Astronomy & Astrophysics **455**, 697–708 (2006).

[46] L. Sironi and A. Spitkovsky, *Acceleration of particles at the termination shock of a relativistic striped wind*, The Astrophysical Journal **741**, 39 (2011).

[47] M. V. Medvedev and A. Loeb, *Generation of Magnetic Fields in the Relativistic Shock of Gamma-Ray Burst Sources*, The Astrophysical Journal **526**, 697–706 (1999).

[48] N. C. Woolsey, Y. A. Ali, R. G. Evans, R. A. D. Grundy, S. J. Pestehe, P. G. Carolan, N. J. Conway, R. O. Dendy, P. Helander, K. G. McClements, J. G. Kirk, P. A. Norreys, M. M. Notley, and S. J. Rose, *Collisionless shock and supernova remnant simulations on VULCAN*, Physics of Plasmas **8**, 2439–2445 (2001).

[49] A. Rigby, F. Cruz, B. Albertazzi, R. Bamford, A. R. Bell, J. E. Cross, F. Fraschetti, P. Graham, Y. Hara, P. M. Kozlowski, Y. Kuramitsu, D. Q. Lamb, S. Lebedev, J. R. Marques, F. Miniati, T. Morita, M. Oliver, B. Reville, Y. Sakawa, S. Sarkar, C. Spindloe, R. Trines, P. Tzeferacos, L. O. Silva, R. Bingham, M. Koenig, and G. Gregori, *Electron acceleration by wave turbulence in a magnetized plasma*, Nature Physics **14**, 475–479 (2018).

[50] L. O. Silva, M. Marti, J. R. Davies, R. A. Fonseca, C. Ren, F. S. Tsung, and W. B. Mori, *Proton Shock Acceleration in Laser-Plasma Interactions*, Physical Review Letters **92**, 015002 (2004).

[51] A. Stockem, F. Fiuza, A. Bret, R. A. Fonseca, and L. O. Silva, *Exploring the nature of collisionless shocks under laboratory conditions*, Scientific Reports **4**, 3934 (2014).

[52] V. Eselevich and M. Eselevich, *Disturbed zone and piston shock ahead of coronal mass ejection*, The Astrophysical Journal **761**, 68 (2012).

[53] A. Spitkovsky and J. Arons, *Time Dependence in Relativistic Collisionless Shocks: Theory of the Variable "Wisps" in the Crab Nebula*, The Astrophysical Journal **603**, 669–681 (2004).

[54] L. O. Drury, *An introduction to the theory of diffusive shock acceleration of energetic particles in tenuous plasmas*, Reports on Progress in Physics **46**, 973–1027 (1983).

[55] L. Ball and D. B. Melrose, *Shock Drift Acceleration of Electrons*, Publications of the Astronomical Society of Australia **18**, 361–373 (2001).

[56] S. Bulanov, T. Esirkepov, V. Khoroshkov, A. Kuznetsov, and F. Pegoraro, *Oncological hadrontherapy with laser ion accelerators*, Physics Letters A **299**, 240–247 (2002).

[57] F. Fiuza, A. Stockem, E. Boella, R. A. Fonseca, L. O. Silva, D. Haberberger, S. Tochitsky, W. B. Mori, and C. Joshi, *Ion acceleration from laser-driven electrostatic shocks*, Physics of Plasmas **20**, 056304 (2013).

[58] A. Pak, S. Kerr, N. Lemos, A. Link, P. Patel, F. Albert, L. Divol, B. B. Pollock, D. Haberberger, D. Froula, M. Gauthier, S. H. Glenzer, A. Longman, L. Manzoor, R. Fedosejevs, S. Tochitsky, C. Joshi, and F. Fiuza, *Collisionless shock acceleration of narrow energy spread ion beams from mixed species plasmas using* 1 μm *lasers*, Physical Review Accelerators and Beams **21**, 103401 (2018).

[59] A. P. L. Robinson, M. Zepf, S. Kar, R. G. Evans, and C. Bellei, *Radiation pressure acceleration of thin foils with circularly polarized laser pulses*, New Journal of Physics **10**, 013021 (2008).

[60] F. J. Dollar, *High Intensity, High Contrast Laser Solid Interactions with Short Pulses*, Ph.D. thesis, University of Michigan (2012).

[61] M. Passoni, L. Bertagna, and A. Zani, *Target normal sheath acceleration: theory, comparison with experiments and future perspectives*, New Journal of Physics **12**, 045012 (2010).

[62] A. Higginson, R. J. Gray, M. King, R. J. Dance, S. D. R. Williamson, N. M. H. Butler, R. Wilson, R. Capdessus, C. Armstrong, J. S. Green, S. J. Hawkes, P. Martin, W. Q. Wei, S. R. Mirfayzi, X. H. Yuan, S. Kar, M. Borghesi, R. J. Clarke, D. Neely, and P. McKenna, *Near-100 MeV protons via a laser-driven transparency-enhanced hybrid acceleration scheme*, Nature Communications **9**, 724 (2018).

[63] N. L. Kugland, D. D. Ryutov, C. Plechaty, J. S. Ross, and H.-S. Park, *Invited Article: Relation between electric and magnetic field structures and their proton-beam images*, Review of Scientific Instruments **83**, 101301 (2012).

[64] J. W. Dungey, *Interplanetary magnetic field and the auroral zones*, Physical Review Letters **6**, 47–48 (1961).

[65] D. F. Webb and T. A. Howard, *Coronal Mass Ejections: Observations*, Living Reviews in Solar Physics **9**, 3 (2012).

[66] G. P. Zank and H.-R. Müller, *The dynamical heliosphere*, Journal of Geophysical Research: Space Physics **108** (2003).

[67] R. N. Manchester, *Observational Properties of Pulsars*, Science **304**, 542–546 (2004).

[68] B. Khiar, G. Revet, A. Ciardi, K. Burdonov, E. Filippov, J. Béard, M. Cerchez, S. N. Chen, T. Gangolf, S. S. Makarov, M. Ouillé, M. Safronova, I. Y. Skobelev, A. Soloviev, M. Starodubtsev, O. Willi, S. Pikuz, and J. Fuchs, *Laser-Produced Magnetic-Rayleigh-Taylor Unstable Plasma Slabs in a 20 T Magnetic Field*, Physical Review Letters **123**, 205001 (2019).

149

[69] D. B. Schaeffer, W. Fox, D. Haberberger, G. Fiksel, A. Bhattacharjee, D. H. Barnak, S. X. Hu, and K. Germaschewski, *Generation and Evolution of High-Mach-Number Laser-Driven Magnetized Collisionless Shocks in the Laboratory*, Physical Review Letters **119**, 025001 (2017).

[70] S. Sakata, S. Lee, H. Morita, T. Johzaki, H. Sawada, Y. Iwasa, K. Matsuo, K. F. F. Law, A. Yao, M. Hata, A. Sunahara, S. Kojima, Y. Abe, H. Kishimoto, A. Syuhada, T. Shiroto, A. Morace, A. Yogo, N. Iwata, M. Nakai, H. Sakagami, T. Ozaki, K. Yamanoi, T. Norimatsu, Y. Nakata, S. Tokita, N. Miyanaga, J. Kawanaka, H. Shiraga, K. Mima, H. Nishimura, M. Bailly-Grandvaux, J. J. Santos, H. Nagatomo, H. Azechi, R. Kodama, Y. Arikawa, Y. Sentoku, and S. Fujioka, *Magnetized fast isochoric laser heating for efficient creation of ultra-high-energy-density states*, Nature Communications **9**, 3937 (2018).

[71] W. Schumaker, N. Nakanii, C. McGuffey, C. Zulick, V. Chvykov, F. Dollar, H. Habara, G. Kalintchenko, A. Maksimchuk, K. A. Tanaka, A. G. R. Thomas, V. Yanovsky, and K. Krushelnick, *Ultrafast Electron Radiography of Magnetic Fields in High-Intensity Laser-Solid Interactions*, Physical Review Letters **110**, 015003 (2013).

[72] R. N. Sudan, *Mechanism for the generation of 10^9 G magnetic fields in the interaction of ultraintense short laser pulse with an overdense plasma target*, Phys. Rev. Lett. **70**, 3075–3078 (1993).

[73] E. G. Zweibel and M. Yamada, *Magnetic Reconnection in Astrphysical and Laboratory Plasmas*, Annual Review of Astronomy and Astrophysics **47**, 291–332 (2009).

[74] M. Øieroset, T. D. Phan, M. Fujimoto, R. P. Lin, and R. P. Lepping, *In situ detection of collisionless reconnection in the Earth's magnetotail*, Nature **412**, 6845 (2001).

[75] A. R. Bell, *Turbulent amplification of magnetic field and diffusive shock acceleration of cosmic rays*, Monthly Notices of the Royal Astronomical Society **353**, 550–558 (2004).

[76] J. F. Drake, M. Opher, M. Swisdak, and J. N. Chamoun, *A magnetic reconnection mechanism for the generation of anomalous cosmic rays*, The Astrophysical Journal **709**, 963–974 (2010).

[77] C. M. Huntington, F. Fiuza, J. S. Ross, A. B. Zylstra, R. P. Drake, D. H. Froula, G. Gregori, N. L. Kugland, C. C. Kuranz, M. C. Levy, C. K. Li, J. Meinecke, T. Morita, R. Petrasso, C. Plechaty, B. A. Remington, D. D. Ryutov, Y. Sakawa, A. Spitkovsky, H. Takabe, and H. S. Park, *Observation of magnetic field generation via the Weibel instability in interpenetrating plasma flows*, Nature Physics **11**, 173–176 (2015).

[78] P. Tzeferacos, A. Rigby, A. F. A. Bott, A. R. Bell, R. Bingham, A. Casner, F. Cattaneo, E. M. Churazov, J. Emig, F. Fiuza, C. B. Forest, J. Foster, C. Graziani, J. Katz, M. Koenig, C. K. Li, J. Meinecke, R. Petrasso, H. S. Park, B. A. Remington, J. S. Ross, D. Ryu, D. Ryutov, T. G. White, B. Reville, F. Miniati, A. A. Schekochihin, D. Q. Lamb, D. H. Froula, and G. Gregori, *Laboratory evidence of dynamo amplification of magnetic fields in a turbulent plasma*, Nature Communications **9**, 591 (2018).

[79] P. Gibbon, *Short Pulse Laser Interactions with Matter: An Introduction*, Imperial College Press, London (2005).

[80] A. E. Siegman, *Lasers*, University Science Books, Sausalito, California (1986).

[81] C. Thaury, F. Quéré, J. P. Geindre, A. Levy, T. Ceccotti, P. Monot, M. Bougeard, F. Réau, P. d'Oliveira, P. Audebert, R. Marjoribanks, and P. Martin, *Plasma mirrors for ultrahigh-intensity optics*, Nature Physics **3**, 424–429 (2007).

[82] F. Druon, G. Chériaux, J. Faure, J. Nees, M. Nantel, A. Maksimchuk, G. Mourou, J. C. Chanteloup, and G. Vdovin, *Wave-front correction of femtosecond terawatt lasers by deformable mirrors*, Optics Letters **23**, 1043–1045 (1998).

[83] V. Yanovsky, V. Chvykov, G. Kalinchenko, P. Rousseau, T. Planchon, T. Matsuoka, A. Maksimchuk, J. Nees, G. Cheriaux, G. Mourou, and K. Krushelnick, *Ultra-high intensity- 300-TW laser at 0.1 Hz repetition rate.*, Optics Express **16**, 2109–2114 (2008).

[84] J. W. Yoon, Y. G. Kim, I. W. Choi, J. H. Sung, H. W. Lee, S. K. Lee, and C. H. Nam, *Realization of laser intensity over $10^{23} W/cm^2$*, Optica **8**, 630–635 (2021).

[85] S. Gales, K. A. Tanaka, D. L. Balabanski, F. Negoita, D. Stutman, O. Tesileanu, C. A. Ur, D. Ursescu, I. Andrei, S. Ataman, M. O. Cernaianu, L. D'Alessi, I. Dancus, B. Diaconescu, N. Djourelov, D. Filipescu, P. Ghenuche, D. G. Ghita, C. Matei, K. Seto, M. Zeng, and N. V. Zamfir, *The extreme light infrastructure—nuclear physics (ELI-NP) facility: new horizons in physics with 10 PW ultra-intense lasers and 20 MeV brilliant gamma beams*, Reports on Progress in Physics **81**, 094301 (2018).

[86] L. V. Keldysh, *Ionization in the field of a strong electromagnetic wave*, Sov. Phys. JETP **20**, 1307–1314 (1965).

[87] F. F. Chen, *Introduction to plasma physics and controlled fusion*, volume 1, Springer (1984).

[88] *R. Fitzpatrick lecture notes, Coulomb Logarithm*, https://farside.ph.utexas.edu/teaching/plasma/Plasma/node39.html.

[89] P. Gibbon and A. R. Bell, *Collisionless absorption in sharp-edged plasmas*, Physical Review Letters **68**, 1535–1538 (1992).

[90] A. J. Kemp, Y. Sentoku, and M. Tabak, *Hot-Electron Energy Coupling in Ultraintense Laser-Matter Interaction*, Physical Review Letters **101**, 075004 (2008).

[91] C. Ridgers, T. Blackburn, D. Del Sorbo, L. Bradley, C. Slade-Lowther, C. Baird, S. Mangles, P. McKenna, M. Marklund, C. Murphy *et al.*, *Signatures of quantum effects on radiation reaction in laser–electron-beam collisions*, Journal of Plasma Physics **83** (2017).

[92] A. Timokhin and A. Harding, *On the polar cap cascade pair multiplicity of young pulsars*, The Astrophysical Journal **810**, 144 (2015).

[93] P. Zhang, C. P. Ridgers, and A. G. R. Thomas, *The effect of nonlinear quantum electrodynamics on relativistic transparency and laser absorption in ultra-relativistic plasmas*, New Journal of Physics **17**, 043051 (2015).

[94] M. Jirka, O. Klimo, M. Vranic, S. Weber, and G. Korn, *QED cascade with 10 PW-class lasers*, Scientific Reports **7**, 1–7 (2017).

[95] A. Bret, *Can We Trust MHD Jump Conditions for Collisionless Shocks?*, The Astrophysical Journal **900**, 111 (2020).

[96] F. Fiuza, A. Stockem, E. Boella, R. A. Fonseca, L. O. Silva, D. Haberberger, S. Tochitsky, C. Gong, W. B. Mori, and C. Joshi, *Laser-Driven Shock Acceleration of Monoenergetic Ion Beams*, Physical Review Letters **109**, 215001 (2012).

[97] R. Z. Sagdeev, Rev. Plasma Phys. **4**, 23–91 (1966).

[98] E. Ott and R. Sudan, *Nonlinear theory of ion acoustic waves with Landau damping*, The Physics of fluids **12**, 2388–2394 (1969).

[99] M. A. Malkov, R. Z. Sagdeev, G. I. Dudnikova, T. V. Liseykina, P. H. Diamond, K. Papadopoulos, C.-S. Liu, and J. J. Su, *Ion-acoustic shocks with self-regulated ion reflection and acceleration*, Physics of Plasmas **23**, 043105 (2016).

[100] G. Sorasio, M. Marti, R. Fonseca, and L. O. Silva, *Very High Mach-Number Electrostatic Shocks in Collisionless Plasmas*, Physical Review Letters **96**, 045005 (2006).

[101] A. Stockem, E. Boella, F. Fiuza, and L. O. Silva, *Relativistic generalization of formation and ion-reflection conditions in electrostatic shocks*, Physical Review E **87**, 043116 (2013).

[102] C. K. Li, F. H. Séguin, J. A. Frenje, J. R. Rygg, R. D. Petrasso, R. P. J. Town, O. L. Landen, J. P. Knauer, and V. A. Smalyuk, *Observation of Megagauss-Field Topology Changes due to Magnetic Reconnection in Laser-Produced Plasmas*, Physical Review Letters **99**, 055001 (2007).

[103] N. Shukla, K. Schoeffler, E. Boella, J. Vieira, R. Fonseca, and L. O. Silva, *Interplay between the Weibel instability and the Biermann battery in realistic laser-solid interactions*, Physical Review Research **2**, 023129 (2020).

[104] *OMEGA EP laser system*, https://www.lle.rochester.edu/index.php/omega-laser-facility-2/6271-2/.

[105] *Omega Laser Facility Users' Guide*, https://www.lle.rochester.edu/index.php/about-the-laboratory-for-laser-energetics/nluf/.

[106] P. T. Campbell, *Laboratory Investigations of Magnetic Field Generation and Interactions Driven by High Power Lasers*, Ph.D. thesis, University of Michigan (2019).

[107] M. Borghesi, A. Schiavi, D. H. Campbell, M. G. Haines, O. Willi, A. J. MacKinnon, L. A. Gizzi, M. Galimberti, R. J. Clarke, and H. Ruhl, *Proton imaging: a diagnostic for inertial confinement fusion/fast ignitor studies*, Plasma Physics and Controlled Fusion **43**, A267 (2001).

[108] A. F. A. Bott, C. Graziani, P. Tzeferacos, T. G. White, D. Q. Lamb, G. Gregori, and A. A. Schekochihin, *Proton imaging of stochastic magnetic fields*, Journal of Plasma Physics **83**, 905830614 (2017).

[109] R. A. Fonseca, L. O. Silva, F. S. Tsung, V. K. Decyk, W. Lu, C. Ren, W. B. Mori, S. Deng, S. Lee, T. Katsouleas, and J. C. Adam, *OSIRIS: A Three-Dimensional, Fully Relativistic Particle in Cell Code for Modeling Plasma Based Accelerators*, in P. M. A. Sloot, A. G. Hoekstra, C. J. K. Tan, and J. J. Dongarra (editors), *Computational Science — ICCS 2002*, 342–351, Springer Berlin Heidelberg, Berlin, Heidelberg (2002).

[110] R. G. Hemker, *Particle-in-cell modeling of plasma-based accelerators in two and three dimensions*, arXiv preprint arXiv:1503.00276 (2015).

[111] M. Vranić, *Extreme laser-matter interactions: multi-scale PIC modelling from the classical to the QED perspective*, Ph.D. thesis, Universidade de Lisboa Instituto Superior Técnico (2015).

[112] K. Yee, *Numerical solution of initial boundary value problems involving Maxwell's equations in isotropic media*, IEEE Transactions on antennas and propagation **14**, 302–307 (1966).

[113] R. Courant, K. Friedrichs, and H. Lewy, *Über die partiellen Differenzengleichungen der mathematischen Physik*, Mathematische Annalen **100**, 32–74 (1928).

[114] M. Vranic, J. L. Martins, R. A. Fonseca, and L. O. Silva, *Classical radiation reaction in particle-in-cell simulations*, Computer Physics Communications **204**, 141–151 (2016).

[115] A. Di Piazza, M. Tamburini, S. Meuren, and C. H. Keitel, *Improved local-constant-field approximation for strong-field QED codes*, Physical Review A **99**, 022125 (2019).

[116] V. Malka, S. Fritzler, E. Lefebvre, E. d'Humières, R. Ferrand, G. Grillon, C. Albaret, S. Meyroneinc, J.-P. Chambaret, A. Antonetti, and D. Hulin, *Practicability of proton-therapy using compact laser systems*, Medical Physics **31**, 1587–1592 (2004).

[117] K. Krushelnick, E. Clark, R. Allott, F. Beg, C. Danson, A. Machacek, V. Malka, Z. Najmudin, D. Neely, P. Norreys, and M. Salvati, *Ultrahigh-intensity laser-produced plasmas as a compact heavy ion injection source*, IEEE Transactions on Plasma Science **28**, 1110–1155 (2000).

[118] M. Borghesi, A. Schiavi, D. H. Campbell, M. G. Haines, O. Willi, A. J. Mackinnon, P. Patel, M. Galimberti, and L. A. Gizzi, *Proton imaging detection of transient electro-magnetic fields in laser-plasma interactions (invited)*, Review of Scientific Instruments **74**, 1688–1693 (2003).

[119] L. Disdier, J.-P. Garçonnet, G. Malka, and J.-L. Miquel, *Fast Neutron Emission from a High-Energy Ion Beam Produced by a High-Intensity Subpicosecond Laser Pulse*, Physical Review Letters **82**, 1454–1457 (1999).

[120] M. Roth, D. Jung, K. Falk, N. Guler, O. Deppert, M. Devlin, A. Favalli, J. Fernandez, D. Gautier, M. Geissel, R. Haight, C. E. Hamilton, B. M. Hegelich, R. P. Johnson, F. Merrill, G. Schaumann, K. Schoenberg, M. Schollmeier, T. Shimada, T. Taddeucci, J. L. Tybo, F. Wagner, S. A. Wender, C. H. Wilde, and G. A. Wurden, *Bright Laser-Driven Neutron Source Based on the Relativistic Transparency of Solids*, Physical Review Letters **110**, 044802 (2013).

[121] P. K. Patel, A. J. Mackinnon, M. H. Key, T. E. Cowan, M. E. Foord, M. Allen, D. F. Price, H. Ruhl, P. T. Springer, and R. Stephens, *Isochoric Heating of Solid-Density Matter with an Ultrafast Proton Beam*, Physical Review Letters **91**, 125004 (2003).

[122] I. Spencer, K. Ledingham, R. Singhal, T. McCanny, P. McKenna, E. Clark, K. Krushelnick, M. Zepf, F. Beg, M. Tatarakis, A. Dangor, P. Norreys, R. Clarke, R. Allott, and I. Ross, *Laser generation of proton beams for the production of short-lived positron emitting radioisotopes*, Nuclear Instruments and Methods in Physics Research Section B: Beam Interactions with Materials and Atoms **183**, 449–458 (2001).

[123] S. P. Hatchett, C. G. Brown, T. E. Cowan, E. A. Henry, J. S. Johnson, M. H. Key, J. A. Koch, A. B. Langdon, B. F. Lasinski, R. W. Lee, A. J. Mackinnon, D. M. Pennington, M. D. Perry, T. W. Phillips, M. Roth, T. C. Sangster, M. S. Singh, R. A. Snavely, M. A. Stoyer, S. C. Wilks, and K. Yasuike, *Electron, photon and ion beams from the relativisit interaction of Petawatt laser pulses with solid targets*, Physics of Plasmas **7** (2000).

[124] M. Borghesi, A. J. Mackinnon, D. H. Campbell, D. G. Hicks, S. Kar, P. K. Patel, D. Price, L. Romagnani, A. Schiavi, and O. Willi, *Multi-MeV proton source investigations in Ultraintense laser-foil iteractions*, Physical Review Letters **92**, 055003 (2004).

[125] S. Kar, K. F. Kakolee, B. Qiao, A. Macchi, M. Cerchez, D. Doria, M. Geissler, P. McKenna, D. Neely, J. Osterholz, R. Prasad, K. Quinn, B. Ramakrishna, G. Sarri, O. Willi, X. Y. Yuan, M. Zepf, and M. Borghesi, *Ion Acceleration in Multispecies Targets Driven by Intense Laser Radiation Pressure*, Physical Review Letters **109**, 185006 (2012).

[126] F. Dollar, C. Zulick, A. G. R. Thomas, V. Chvykov, J. Davis, G. Kalinchenko, T. Matsuoka, C. McGuffey, G. M. Petrov, L. Willingale, V. Yanovsky, A. Maksimchuk, and K. Krushelnick, *Finite Spot Effects on Radiation Pressure Acceleration from Intense High-Contrast Laser Interactions with Thin Targets*, Physical Review Letters **108**, 175005 (2012).

[127] C. A. J. Palmer, J. Schreiber, S. R. Nagel, N. P. Dover, C. Bellei, F. N. Beg, S. Bott, R. J. Clarke, A. E. Dangor, S. M. Hassan, P. Hilz, D. Jung, S. Kneip, S. P. D. Mangles, K. L. Lancaster, A. Rehman, A. P. L. Robinson, C. Spindloe, J. Szerypo, M. Tatarakis,

M. Yeung, M. Zepf, and Z. Najmudin, *Rayleigh-Taylor Instability of an Ultrathin Foil Accelerated by the Radiation Pressure of an Intense Laser*, Physical Review Letters **108**, 225002 (2012).

[128] W. J. Ma, I. J. Kim, J. Q. Yu, I. W. Choi, P. K. Singh, H. W. Lee, J. H. Sung, S. K. Lee, C. Lin, Q. Liao, J. G. Zhu, H. Y. Lu, B. Liu, H. Y. Wang, R. F. Xu, X. T. He, J. E. Chen, M. Zepf, J. Schreiber, X. Q. Yan, and C. H. Nam, *Laser Acceleration of Highly Energetic Carbon Ions Using a Double-Layer Target Composed of Slightly Underdense Plasma and Ultrathin Foil*, Physical Review Letters **122**, 014803 (2019).

[129] J. H. Bin, W. J. Ma, H. Y. Wang, M. J. V. Streeter, C. Kreuzer, D. Kiefer, M. Yeung, S. Cousens, P. S. Foster, B. Dromey, X. Q. Yan, R. Ramis, J. Meyer-ter Vehn, M. Zepf, and J. Schreiber, *Ion Acceleration Using Relativistic Pulse Shaping in Near-Critical-Density Plasmas*, Physical Review Letters **115**, 064801 (2015).

[130] D. Haberberger, S. Tochitsky, F. Fiuza, C. Gong, R. A. Fonseca, L. O. Silva, W. B. Mori, and C. Joshi, *Collisionless shocks in laser-produced plasma generate monoenergetic high-energy proton beams*, Nature Physics **8**, 95 – 99 (2011).

[131] C. A. J. Palmer, N. P. Dover, I. Pogorelsky, M. Babzien, G. I. Dudnikova, M. Ispiriyan, M. N. Polyanskiy, J. Schreiber, P. Shkolnikov, V. Yakimenko, and Z. Najmudin, *Monoenergetic Proton Beams Accelerated by a Radiation Pressure Driven Shock*, Physical Review Letters **106**, 014801 (2011).

[132] M. S. Wei, S. P. D. Mangles, Z. Najmudin, B. Walton, A. Gopal, M. Tatarakis, A. E. Dangor, E. L. Clark, R. G. Evans, S. Fritzler, R. J. Clarke, C. Hernandez-Gomez, D. Neely, W. Mori, M. Tzoufras, and K. Krushelnick, *Ion Acceleration by Collisionless Shocks in High-Intensity-Laser–Underdense-Plasma Interaction*, Physical Review Letters **93**, 155003 (2004).

[133] P. Kordell, *Collisionless Shock Acceleration of Ions in Underdense Plasma*, Ph.D. thesis, University of Michigan (2019).

[134] G. Hicks, O. Ettlinger, M. Borghesi, D. Carroll, R. Clarke, E. Ditter, T. Frazer, R. Gray, A. McIlvenny, P. McKenna, C. Palmer, L. Willingale, and Z. Najmudin, *Spectrally peaked proton beams shock accelerated from an optically shaped overdense gas jet by a near-infrared laser*, arXiv preprint arXiv:2104.13977 (2021).

[135] M. H. Helle, D. F. Gordon, D. Kaganovich, Y. Chen, J. P. Palastro, and A. Ting, *Laser-Accelerated Ions from a Shock-Compressed Gas Foil*, Physical Review Letters **117**, 165001 (2016).

[136] S. N. Chen, M. Vranic, T. Gangolf, E. Boella, P. Antici, M. Bailly-Grandvaux, P. Loiseau, H. Pépin, G. Revet, J. J. Santos, A. M. Schroer, M. Starodubtsev, O. Willi, L. O. Silva, E. d'Humières, and J. Fuchs, *Collimated protons accelerated from an overdense gas jet irradiated by a 1 µm wavelength high-intensity short-pulse laser*, Scientific Reports **7**, 165001 (2017).

[137] F. Sylla, M. Veltcheva, S. Kahaly, A. Flacco, and V. Malka, *Development and characterization of very dense submillimetric gas jets for laser-plasma interaction*, Review of Scientific Instruments **83**, 033507 (2012).

[138] R. Kumar, Y. Sakawa, L. N. K. Döhl, N. Woolsey, and A. Morace, *Enhancement of collisionless shock ion acceleration by electrostatic ion two-stream instability in the upstream plasma*, Physiacl Review Accelerators and Beams **22**, 043401 (2019).

[139] I. Pusztai, J. M. TenBarge, A. N. Csapó, J. Juno, A. Hakim, L. Yi, and T. Fülöp, *Low Mach-number collisionless electrostatic shocks and associated ion acceleration*, Plasma Physics and Controlled Fusion **60**, 035004 (2018).

[140] S. Tochitsky, A. Pak, F. Fiuza, D. Haberberger, N. Lemos, A. Link, D. H. Froula, and C. Joshi, *Laser-driven collisionless shock acceleration of ions from near-critical plasmas*, Physics of Plasmas **27**, 083102 (2020).

[141] R. Kumar, Y. Sakawa, T. Sano, L. N. K. Döhl, N. Woolsey, and A. Morace, *Ion acceleration at two collisionless shocks in a multicomponent plasma*, Physical Review E **103**, 043201 (2021).

[142] B. D. Keenan, A. N. Simakov, L. Chacón, and W. T. Taitano, *Deciphering the kinetic structure of multi-ion plasma shocks*, Physical Review E **96**, 053203 (2017).

[143] R. A. Fonseca, L. O. Silva, F. S. Tsung, V. K. Decyk, W. Lu, C. Ren, W. B. Mori, S. Deng, S. Lee, T. Katsouleas, and J. C. Adam, *OSIRIS: A Three-Dimensional, Fully Relativistic Particle in Cell Code for Modeling Plasma Based Accelerators*, in P. M. A. Sloot, A. G. Hoekstra, C. J. K. Tan, and J. J. Dongarra (editors), *Computational Science — ICCS 2002*, 342–351, Springer Berlin Heidelberg, Berlin, Heidelberg (2002).

[144] R. G. Hemker, *PhD Thesis UCLA* (1999).

[145] A. Macchi, A. S. Nindrayog, and F. Pegoraro, *Solitary versus shock wave acceleration in laser-plasma interactions*, Physical Review E **85**, 046402 (2012).

[146] H. Schamel, *Stationary solitary, snoidal and sinusoidal ion acoustic waves*, Plasma Physics **14**, 905–924 (1972).

[147] S. C. Wilks, W. L. Kruer, M. Tabak, and A. B. Langdon, *Absorption of ultra-intense laser pulses*, Physical Review Letters **69**, 1383–1386 (1992).

[148] W. L. Zhang, B. Qiao, T. W. Huang, X. F. Shen, W. Y. You, X. Q. Yan, S. Z. Wu, C. T. Zhou, and X. T. He, *Quasi-monoenergetic ion beam acceleration by laser-driven shock and solitary waves in near-critical plasmas*, Physics of Plasmas **23**, 073118 (2016).

[149] P. Puyuelo-Valdes, J. L. Henares, F. Hannachi, T. Ceccotti, J. Domange, M. Ehret, E. d'Humieres, L. Lancia, J.-R. Marquès, X. Ribeyre, J. J. Santos, V. Tikhonchuk, and M. Tarisien, *Proton acceleration by collisionless shocks using a supersonic H2 gas-jet target and high-power infrared laser pulses*, Physics of Plasmas **26**, 123109 (2019).

[150] D. Kraus, A. Ravasio, M. Gauthier, D. O. Gericke, J. Vorberger, S. Frydrych, J. Helfrich, L. B. Fletcher, G. Schaumann, B. Nagler, B. Barbrel, B. Bachmann, E. J. Gamboa, S. Göde, E. Granados, G. Gregori, H. J. Lee, P. Neumayer, W. Schumaker, T. Döppner, R. W. Falcone, S. H. Glenzer, and M. Roth, *Nanosecond formation of diamond and lonsdaleite by shock compression of graphite*, Nature Communications **7**, 10970 (2016).

[151] A. Rigby, F. Cruz, B. Albertazzi, R. Bamford, A. R. Bell, J. E. Cross, F. Fraschetti, P. Graham, Y. Hara, P. M. Kozlowski, Y. Kuramitsu, D. Q. Lamb, S. Lebedev, J. R. Marques, F. Miniati, T. Morita, M. Oliver, B. Reville, Y. Sakawa, S. Sarkar, C. Spindloe, R. Trines, P. Tzeferacos, L. O. Silva, R. Bingham, M. Koenig, and G. Gregori, *Electron acceleration by wave turbulence in a magnetized plasma*, Nature Physics **14**, 475–479 (2018).

[152] J. A. Stamper and B. H. Ripin, *Faraday-Rotation Measurements of Megagauss Magnetic Fields in Laser-Produced Plasmas*, Physical Review Letters **34**, 138–141 (1975).

[153] P. T. Campbell, C. A. Walsh, B. K. Russell, J. P. Chittenden, A. Crilly, G. Fiksel, L. Gao, I. V. Igumenshchev, P. M. Nilson, A. G. R. Thomas, K. Krushelnick, and L. Willingale, *Measuring magnetic flux suppression in high-power laser–plasma interactions*, Physics of Plasmas **29**, 012701 (2022).

[154] M. G. Haines, *Heat flux effects in Ohm's law*, Plasma Physics and Controlled Fusion **28**, 1705–1716 (1986).

[155] L. Willingale, A. G. R. Thomas, P. M. Nilson, M. C. Kaluza, S. Bandyopadhyay, A. E. Dangor, R. G. Evans, P. Fernandes, M. G. Haines, C. Kamperidis, R. J. Kingham, S. Minardi, M. Notley, C. P. Ridgers, W. Rozmus, M. Sherlock, M. Tatarakis, M. S. Wei, Z. Najmudin, and K. Krushelnick, *Fast Advection of Magnetic Fields by Hot Electrons*, Physical Review Letters **105**, 095001 (2010).

[156] L. Lancia, B. Albertazzi, C. Boniface, A. Grisollet, R. Riquier, F. Chaland, K.-C. Le Thanh, P. Mellor, P. Antici, S. Buffechoux, S. N. Chen, D. Doria, M. Nakatsutsumi, C. Peth, M. Swantusch, M. Stardubtsev, L. Palumbo, M. Borghesi, O. Willi, H. Pépin, and J. Fuchs, *Topology of Megagauss Magnetic Fields and of Heat-Carrying Electrons Produced in a High-Power Laser-Solid Interaction*, Physical Review Letters **113**, 235001 (2014).

[157] S. C. Wilks, A. B. Langdon, T. E. Cowan, M. Roth, M. Singh, S. Hatchett, M. H. Key, D. Pennington, A. MacKinnon, and R. A. Snavely, *Energetic proton generation in ultra-intense laser–solid interactions*, Physics of Plasmas **8**, 542–549 (2001).

[158] A. Maksimchuk, S. Gu, K. Flippo, D. Umstadter, and V. Y. Bychenkov, *Forward Ion acceleration in thin films driven by a high-intensity laser*, Physical Review Letters **84** (2000).

[159] R. A. Snavely, M. H. Key, S. P. Hatchett, T. E. Cowan, M. Roth, T. W. Phillips, M. A. Stoyer, E. A. Henry, T. C. Sangster, M. S. Singh, S. C. Wilks, A. MacKinnon, A. Offenberger, D. M. Pennington, K. Yasuike, A. B. Langdon, B. F. Lasinski, J. Johnson, M. D. Perry, and E. M. Campbell, *Intense High-Energy Proton Beams from Petawatt-Laser Irradiation of Solids*, Physical Review Letters **85**, 2945 (2000).

[160] E. L. Clark, K. Krushelnick, J. R. Davies, M. Zepf, F. N. Beg, M. Tatarikis, A. Machacek, P. A. Norreys, M. I. K. Santala, I. Watts, and A. E. Dangor, *Measurment of Energetic Proton Transport through Magnetized Plasma from Intense Laser Interactions with Solids*, Physical Review Letters **84**, 670 (2000).

[161] C. K. Li, F. H. Séguin, J. A. Frenje, J. R. Rygg, R. D. Petrasso, R. P. J. Town, P. A. Amendt, S. P. Hatchett, O. L. Landen, A. J. Mackinnon, P. K. Patel, V. A. Smalyuk, T. C. Sangster, and J. P. Knauer, *Measuring E and B Fields in Laser-Produced Plasmas with Monoenergetic Proton Radiography*, Physical Review Letters **97**, 135003 (2006).

[162] C. Ruyer, S. Bolaños, B. Albertazzi, S. N. Chen, P. Antici, J. Böker, V. Dervieux, L. Lancia, M. Nakatsutsumi, L. Romagnani, R. Shepherd, M. Swantusch, M. Borghesi, O. Willi, H. Pépin, M. Starodubtsev, M. Grech, C. Riconda, L. Gremillet, and J. Fuchs, *Growth of concomitant laser-driven collisionless and resistive electron filamentation instabilities over large spatiotemporal scales*, Nature Physics **16**, 983–988 (2020).

[163] M. J. Rosenberg, C. K. Li, W. Fox, I. Igumenshchev, F. H. Séguin, R. P. J. Town, J. A. Frenje, C. Stoeckl, V. Glebov, and R. D. Petraso, *A Laboratory study of asymmetric magnetic reconnection in strongly driven plasmas*, Nature Communications **6**, 6190 (2015).

[164] J. P. Chittenden, S. V. Lebedev, C. A. Jennings, S. N. Bland, and A. Ciardi, *X-ray generation mechanisms in three-dimensional simulations of wire array Z-pinches*, Plasma Physics and Controlled Fusion **46**, B457–B476 (2004).

[165] A. Ciardi, S. V. Lebedev, A. Frank, E. G. Blackman, J. P. Chittenden, C. J. Jennings, D. J. Ampleford, S. N. Bland, S. C. Bott, J. Rapley, G. N. Hall, F. A. Suzuki-Vidal, A. Marocchino, T. Lery, and C. Stehle, *The evolution of magnetic tower jets in the laboratory*, Physics of Plasmas **14**, 056501 (2007).

[166] C. A. Walsh, J. P. Chittenden, D. W. Hill, and C. Ridgers, *Extended-magnetohydrodynamics in under-dense plasmas*, Physics of Plasmas **27**, 022103 (2020).

[167] J. Dargent, F. Lavorenti, F. Califano, P. Henri, F. Pucci, and S. S. Cerri, *Interplay between Kelvin–Helmholtz and lower-hybrid drift instabilities*, Journal of Plasma Physics **85**, 805850601 (2019).

[168] E. P. Alves, T. Grismayer, R. A. Fonseca, and L. O. Silva, *Electron-scale shear instabilities: magnetic field generation and particle acceleration in astrophysical jets*, New Journal of Physics **16**, 035007 (2014).

[169] N. T. Gladd, *The lower hybrid drift instability and the modified two stream instability in high density theta pinch environments*, Plasma Physics **18**, 27–40 (1976).

[170] J. Park, D. Caprioli, and A. Spitkovsky, *Simultaneous Acceleration of Protons and Electrons at Nonrelativistic Quasiparallel Collisionless Shocks*, Physical Review Letters **114**, 085003 (2015).

[171] X. Guo, L. Sironi, and R. Narayan, *Non-Thermal Electron Acceleration in ow Mach Number Collisionless Shocks. I. Particle Energy Spectra and Acceleration Mechanism*, Astrophysical Journal **794**, 153 (2014).

[172] T. D. Phan, J. P. Eastwood, M. A. Shay, J. F. Drake, B. U. Ö. Sonnerup, M. Fujimoto, P. A. Cassak, M. Øieroset, J. L. Burch, R. B. Torbert, A. C. Rager, J. C. Dorelli, D. J. Gershman, C. Pollock, P. S. Pyakurel, C. C. Haggerty, Y. Khotyaintsev, B. Lavraud, Y. Saito, M. Oka, R. E. Ergun, A. Retino, O. Le Contel, M. R. Argall, B. L. Giles, T. E. Moore, F. D. Wilder, R. J. Strangeway, C. T. Russell, P. A. Lindqvist, and W. Magnes, *Electron magnetic reconnection without ion coupling in Earth's turbulent magnetosheath*, Nature **557**, 202–206 (2018).

[173] S. R. Kulkarni, S. N. Vogel, Z. Wang, and D. O. S. Wood, *Identification of the nebula G70.7 + 1.2 as a bow shock powered by a pulsar/Be-star binary*, Nature **360**, 139–141 (1992).

[174] C. A. J. Palmer, P. T. Campbell, Y. Ma, L. Antonelli, A. F. A. Bott, G. Gregori, J. Halliday, Y. Katzir, P. Kordell, K. Krushelnick, S. V. Lebedev, E. Montgomery, M. Notley, D. C. Carroll, C. P. Ridgers, A. A. Schekochihin, M. J. V. Streeter, A. G. R. Thomas, E. R. Tubman, N. Woolsey, and L. Willingale, *Field reconstruction from proton radiography of intense laser driven magnetic reconnection*, Physics of Plasmas **26**, 083109 (2019).

[175] A. Brandenburg and K. Subramanian, *Astrophysical magnetic fields and nonlinear dynamo theory*, Physics Reports **417**, 1–209 (2005).

[176] R. Schlickeiser and P. Shukla, *Cosmological Magnetic Field Generation by the Weibel Instability*, Astrophysical Journal **599**, L57 (2003).

[177] H. Daido, F. Miki, K. Mima, M. Fujita, K. Sawai, H. Fujita, Y. Kitagawa, S. Nakai, and C. Yamanaka, *Generation of a strong magnetic field by an intense CO_2 laser pulse*, Physical Review Letters **56**, 846–849 (1986).

[178] K. M. Schoeffler, N. F. Loureiro, R. A. Fonseca, and L. O. Silva, *Magnetic-Field Generation and Amplification in an Expanding Plasma*, Physical Review Letters **112**, 175001 (2014).

[179] Y. Shi, K. Weichman, R. J. Kingham, and A. V. Arefiev, *Magnetic field generation in a laser-irradiated thin collisionless plasma target by return current electrons carrying orbital angular momentum*, New Journal of Physics **22**, 073067 (2020).

[180] T. Wang, T. Toncian, M. S. Wei, and A. V. Arefiev, *Structured targets for detection of Megatesla-level magnetic fields through Faraday rotation of XFEL beams*, Physics of Plasmas **26**, 013105 (2019).

[181] Z. Gong, K. Z. Hatsagortsyan, and C. H. Keitel, *Retrieving Transient Magnetic Fields of Ultrarelativistic Laser Plasma via Ejected Electron Polarization*, Physial Review Letters **127**, 165002 (2021).

[182] T. Grismayer, M. Vranic, J. L. Martins, R. A. Fonseca, and L. O. Silva, *Laser absorption via quantum electrodynamics cascades in counter propagating laser pulses*, Physics of Plasmas **23**, 056706 (2016).

[183] T. Grismayer, M. Vranic, J. L. Martins, R. A. Fonseca, and L. O. Silva, *Seeded QED cascades in counterpropagating laser pulses*, Physical Review E **95**, 023210 (2017).

[184] J. Stamper and B. Ripin, *Faraday-rotation measurements of megagauss magnetic fields in laser-produced plasmas*, Physical Review Letters **34**, 138 (1975).

[185] M. Tatarakis, I. Watts, F. Beg, E. Clark, A. Dangor, A. Gopal, M. Haines, P. Norreys, U. Wagner, M.-S. Wei, M. Zepf, and K. Krushelnick, *Measuring huge magnetic fields*, Nature **415**, 280–280 (2002).

[186] A. J. Gonsalves, K. Nakamura, J. Daniels, C. Benedetti, C. Pieronek, T. C. H. de Raadt, S. Steinke, J. H. Bin, S. S. Bulanov, J. van Tilborg, C. G. R. Geddes, C. B. Schroeder, C. Tóth, E. Esarey, K. Swanson, L. Fan-Chiang, G. Bagdasarov, N. Bobrova, V. Gasilov, G. Korn, P. Sasorov, and W. P. Leemans, *Petawatt Laser Guiding and Electron Beam Acceleration to 8 GeV in a Laser-Heated Capillary Discharge Waveguide*, Phys. Rev. Lett. **122**, 084801 (2019).

[187] S. Kneip, C. McGuffey, J. L. Martins, M. S. Bloom, V. Chvykov, F. Dollar, R. Fonseca, S. Jolly, G. Kalintchenko, K. Krushelnick, A. Maksimchuk, S. P. D. Mangles, Z. Najmudin, C. A. J. Palmer, K. T. Phuoc, W. Schumaker, L. O. Silva, J. Vieira, V. Yanovsky, and A. G. R. Thomas, *Characterization of transverse beam emittance of electrons from a laser-plasma wakefield accelerator in the bubble regime using betatron x-ray radiation*, Physical Review Special Topics-Accelerators and Beams **15**, 021302 (2012).

[188] R. Weingartner, M. Fuchs, A. Popp, S. Raith, S. Becker, S. Chou, M. Heigoldt, K. Khrennikov, J. Wenz, T. Seggebrock, B. Zeitler, Z. Major, J. Osterhoff, F. Krausz, S. Karsch, and F. Grüner, *Imaging laser-wakefield-accelerated electrons using miniature magnetic quadrupole lenses*, Physical Review Special Topics-Accelerators and Beams **14**, 052801 (2011).

[189] C. Thaury, E. Guillaume, A. Döpp, R. Lehe, A. Lifschitz, K. Ta Phuoc, J. Gautier, J.-P. Goddet, A. Tafzi, A. Flacco, F. Tissandier, S. Sebban, A. Rousse, and V. Malka, *Demonstration of relativistic electron beam focusing by a laser-plasma lens*, Nature communications **6**, 1–5 (2015).

[190] K. Nakamura, A. Gonsalves, C. Lin, A. Smith, D. Rodgers, R. Donahue, W. Byrne, and W. Leemans, *Electron beam charge diagnostics for laser plasma accelerators*, Physical Review Special Topics-Accelerators and Beams **14**, 062801 (2011).

[191] J. Cardarelli, *Private Communication* (2022).

[192] R. Mbarek, C. Haggerty, L. Sironi, M. Shay, and D. Caprioli, *Relativistic Asymmetric Magnetic Reconnection*, Physiacl Review Letters **128**, 145101 (2022).

[193] *Extreme Light Infrastructure (ELI)*, https://eli-laser.eu/.

[194] *Apollon*, https://apollonlaserfacility.cnrs.fr/en/home/.

[195] Z. Gan, L. Yu, C. Wang, Y. Liu, Y. Xu, W. Li, S. Li, L. Yu, X. Wang, X. Liu *et al.*, *The Shanghai Superintense Ultrafast Laser Facility (SULF) Project*, Progress in Ultrafast Intense Laser Science XVI 199–217 (2021).

[196] *CORELS*, https://www.ibs.re.kr/eng/sub02_03_05.do.

[197] National Academies of Sciences, Engineering, and Medicine, *Opportunities in Intense Ultrafast Lasers: Reaching for the Brightest Light*, National Academies Press (2018).

[198] R. Falcone, F. Albert, F. Beg, S. Glenzer, T. Ditmire, T. Spinka, and J. Zuegel, *Workshop report: brightest light initiative (March 27-29 2019, OSA Headquarters, Washington, DC)*, arXiv preprint arXiv:2002.09712 (2020).

[199] J. Bromage, S.-W. Bahk, M. Bedzyk, I. Begishev, S. Bucht, C. Dorrer, C. Feng, C. Jeon, C. Mileham, R. Roides *et al.*, *MTW-OPAL: a technology development platform for ultra-intense optical parametric chirped-pulse amplification systems*, High Power Laser Science and Engineering **9** (2021).

[200] *Department of Energy gives green light for a flagship petawatt laser facility at SLAC*, https://www6.slac.stanford.edu/news/2021-10-07-department-energy-gives-green-light-flagship-petawatt-laser-facility-slac.aspx.